THE DEVELOPMENT OF MULTIPLE SEEPAGE FACES ALONG HETEROGENEOUS HILLSIDES

by

Jennifer Rulon

B.Sc. The University of Washington, 1979

A THESIS SUBMITTED IN PARTIAL FULFILMENT OF
THE REQUIREMENT FOR THE DEGREE OF
DOCTOR OF PHILOSOPHY

in

THE FACULTY OF GRADUATE STUDIES
(Department of Interdisciplinary Hydrology)

We accept this thesis as conforming
to the required standard

THE UNIVERSITY OF BRITISH COLUMBIA

June 1984

In presenting this thesis in partial fulfilment of the requirements for an advanced degree at the University of British Columbia, I agree that the Library shall make it freely available for reference and study. I further agree that permission for extensive copying of this thesis for scholarly purposes may be granted by the head of my department or by his or her representatives. It is understood that copying or publication of this thesis for financial gain shall not be allowed without my written permission.

Department of Interdisciplinary Hydrology

The University of British Columbia
1956 Main Mall
Vancouver, Canada
V6T 1Y3

Date 20 June 1984

ABSTRACT

A study has been made to clarify the water-table configuration and hydraulic-head distribution in layered hillsides containing multiple seepage faces. A finite-element model was used to simulate two-dimensional, saturated and unsaturated, steady-state, and transient flow through layered slopes. A laboratory sand-tank experiment was built to test the physical foundation of the mathematical model; the test met with success. Layered slopes were found to feature perched water tables and wedge-shaped unsaturated zones which, in some cases, can extend several kilometers into the flow region. The results demonstrate that the hydraulic-head distribution and the formation of multiple seepage faces are strongly dependent on the position of the impeding layers, the hydraulic conductivity contrast, the rainfall rate, anisotropy, and the slope angle. Predictions of the groundwater conditions based on homogeneous, saturated analyses may be significantly in error when applied to problems in layered slopes. This study has implications with respect to slope stability, inflows into excavations, regional groundwater flow, the occurrence of perched flow systems, and hillslope processes involved in landform development.

TABLE OF CONTENTS

TABLE OF CONTENTS (continued)

LIST OF TABLES

LIST OF ILLUSTRATIONS

ACKNOWLEDGMENTS

I would like to thank Al Freeze for his guidance and encouragement throughout the entire project and for suggesting the thesis topic. In addition, I would like to thank him for his generous financial support. All funding came from a grant awarded to Al Freeze by The National Science and Engineering Research Council of Canada.

I would also like to thank the talented technical staff in the Geology Department at the University of British Columbia. Ray Rodway built most of the equipment used in the laboratory experiment; Ed Montgomery took photos of the laboratory work; John Knight assembled the electronic equipment; and, Gord Hodge drafted the figures.

I appreciate the helpful comments of my committee members; namely, Leslie Smith, Jan deVries, Bill Mathews, Olav Slaymaker, and Peter Byrne. I am grateful to Nick Sitar for advice during the early part of this work and to John Nieber who provided valuable guidance in the design of the physical model.

Finally, special thanks to Keith Loague, Grant Garven, and Chuck Mase for their assistance in the lab as well as for helpful discussions throughout the entire project.

Chapter 1

INTRODUCTION

Groundwater conditions within a hillslope play an important role in many geotechnical, hydrogeological, and geomorphological problems. For example, geotechnical engineers must predict the fluid-pressure distribution along potential failure surfaces and calculate inflow rates into excavations. Hydrogeologists may be required to assess the role of groundwater discharge in areas where shoreline erosion is a problem. Geomorphologists study the role of groundwater in hillslope processes as they relate to landform development. In each instance, the fluid-pressure distribution, the location of discharge areas, and the rates of discharge must be predicted. Our ability to make these predictions is well established for homogeneous hillsides. However, real geologic environments are almost always heterogeneous. This thesis contributes to our ability to predict groundwater conditions in heterogeneous hillsides.

In both homogeneous and heterogenous hillsides, the discharge phenomena are associated with the presence of a seepage face. A seepage face is defined as a saturated outflow boundary along which the fluid pressure is atmospheric. A seepage face forms when the water table intersects the soil surface above the water level in an adjacent sink. The factors governing the formation of seepage faces are therefore the same as those controlling the position of the water table, namely, interactions between: a) the saturated and unsaturated flow

systems, b) the geology of the hillside, and c) the hydro-meteorological conditions along the boundaries of the flow region.

There are two general approaches that can be used to analyze flow conditions in regions containing a seepage face. The first, known as the "free-surface" approach, assumes that flow above the water table is negligible so that only the saturated portion of the flow region is analyzed. The advantage of this approach is its simplicity; the governing equation of flow is relatively easy to solve with existing analytical or numerical techniques. The disadvantage is that it does not generally allow one to specify a recharge rate to the saturated zone.

The second approach involves an analysis of both the saturated and unsaturated flow regions. This approach is more physically-based and is generally amenable to numerical solution. However, the data required to characterize the hydraulic properties of the unsaturated zone are difficult to measure on a routine basis. In addition, numerical difficulties can prevent one from obtaining a solution in some instances.

Both approaches have been applied successfully to homogeneous hillsides containing a single, continuous seepage face. However, in nature, we observe that hillsides may exhibit several discontinuous seepage faces resulting from the complex, saturated-unsaturated flow systems that develop in heterogeneous geological environments. These flow systems

feature perched water tables and wedge-shaped unsaturated zones located above the main saturated zone and must be studied with a saturated-unsaturated analysis. The work presented in this thesis provides such an analysis of the fluid-pressure distribution and geometry of multiple seepage faces on heterogeneous hillsides. The study is limited to horizontally layered slopes, as these are an important type of heterogeneous geological environment.

From a theoretical standpoint, this research will: a) clarify the nature of the fluid-pressure distribution and hydraulic-head distribution in layered slopes containing more than one seepage face, b) investigate the relative quantities of outflow from the seepage faces, c) indicate which combinations of hydrogeologic variables are most likely to produce multiple seepage faces, d) show the response of these systems to transient rainfall events, and e) provide insight into the mechanisms by which perched flow systems form. From a practical standpoint, this research will aid field studies requiring an understanding of the groundwater conditions in layered slopes.

During the writing stages of this thesis, Cooley (1983) published a study in which he developed a new technique to overcome some of the numerical difficulties particular to saturated-unsaturated modeling. He presents several examples of the applicability of his model, including a drainage problem involving multiple seepage faces. To the author's knowledge, this is the only previously published attempt to model multiple

seepage faces. While Cooley's work deals primarily with his numerical methodology, the emphasis of the study presented here is placed on the factors controlling the occurrence of multiple seepage faces.

There are four objectives of this study. The first is to select a finite-element model that will predict the fluid-pressure distribution and seepage-face locations in layered, heterogeneous hillsides. The second is to build a laboratory model to verify the physical foundation of the solutions generated by the numerical model. The third objective is to use the numerical model in sensitivity studies designed to reach quantitative conclusions about the factors governing the development of multiple seepage faces. The final objective is to form generalized conclusions regarding the importance of multiple seepage faces in geotechnical, hydrogeological, and geomorphological problems.

It is not the intention of this study to provide a model to be used routinely in practical, site-specific problems; the amount of field data required by the model would be prohibitive in most cases. Instead, the model is best suited to generic studies, that is, in the application to relatively simple, hypothetical hillsides to assess general mechanisms. The results of these generic studies should prove useful in the development of appropriate strategies to resolve individual, practical problems. For example, a general understanding of the water-table configuration and the geometry of the saturated and unsaturated flow regions would be useful when designing data collection networks in layered media.

This thesis is organized in the following manner: Chapter 2 provides a description of the mathematical model, Chapter 3 describes the laboratory work performed to verify the mathematical model, Chapter 4 describes the steady-state sensitivity study, Chapter 5 presents the results of two preliminary transient studies, Chapter 6 discusses applications of the results to geotechnical, hydrogeological and geomorphological problems, and Chapter 7 contains the summary and conclusions.

Chapter 2

THE MATHEMATICAL MODEL

Freeze (1978) outlined four steps involved in building a mathematical model. The first step is to describe the physical problem. The second step is to replace the physical problem with an equivalent boundary-value problem, noting the assumptions required to establish an equivalence. The third step is to choose a mathematical technique to solve the boundary-value problem. These three steps are discussed in this chapter. The final step, interpreting the mathematical results in terms of the physical problem, will be discussed later in the thesis, following the sensitivity studies.

2.1 The Physical Problem

The physical problem introduced in Chapter 1 is illustrated in a simplified form in Figure 1. The region ABCDEFA represents a two-dimensional, vertical cross section through a layered hillside. Each geologic unit is homogeneous and isotropic with respect to hydraulic conductivity. The hydraulic conductivity of the shaded layer is less than that of the surrounding material. The flow region is bounded below by impermeable strata. The boundaries AB and CD represent groundwater divides and provide vertical impermeable boundaries. Water may infiltrate into the region along ED and may discharge into a river located along AF and across seepage faces, as they develop along FE. The physical problem is to

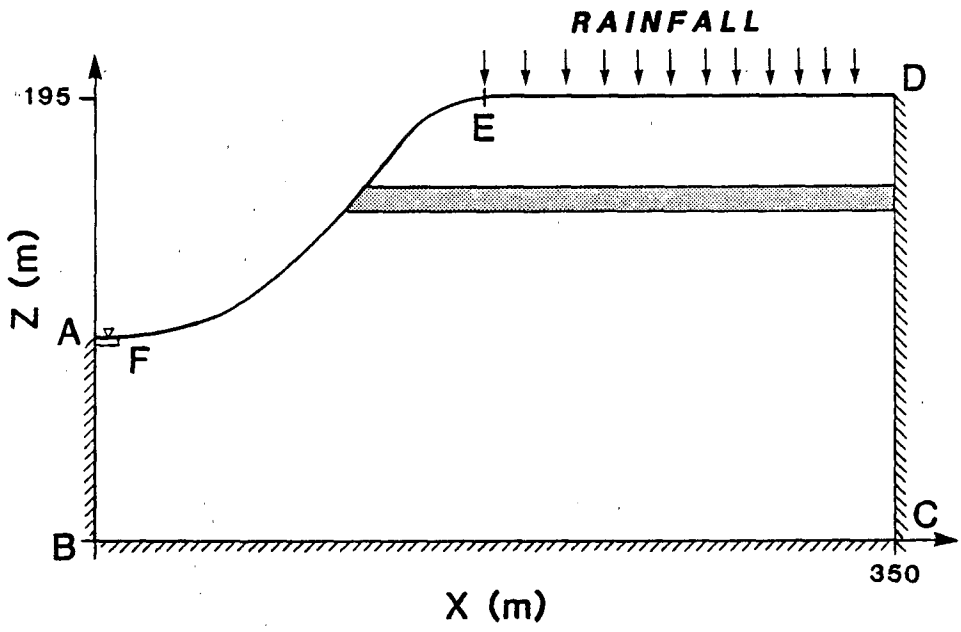

Figure 1. Hypothetical flow region.

determine the saturated-unsaturated flow patterns responsible for the development of multiple seepage faces in this type of hydrogeologic environment.

2.2 The Boundary-Value Problem

Toth (1962, 1963) was the first hydrogeologist to recognize that regional groundwater flow patterns could be obtained mathematically as solutions to boundary-value problems. The method has become a standard theoretical approach for solving both regional and local groundwater flow problems and will be used in the present study. To set up the boundary-value problem for transient flow conditions in the region shown in Figure 1, one needs a governing equation of flow, knowledge of the hydrogeologic parameters that control the flow, boundary conditions, and initial conditions. These requirements are discussed in this section.

Transient, saturated-unsaturated flow through a two-dimensional, heterogeneous and isotropic flow region is governed by the following equation:

$$\frac{\partial}{\partial x}\left[K(x,z,\psi)\ \frac{\partial \psi}{\partial x}\right] + \frac{\partial}{\partial z}\left[K(x,z,\psi)\left(\frac{\partial \psi}{\partial z} + 1\right)\right] = \left[C(\psi) + \frac{\theta}{n} S_s\right] \frac{\partial \psi}{\partial t} \qquad 2.1$$

where ψ = pressure head, [L], K = hydraulic conductivity, [L/T], C = specific moisture capacity, [1/L], S_s = specific storage, [1/L], θ = volumetric water content, [L^3/L^3], n = porosity, [L^3/L^3], t = time, [T], and x,z = horizontal and

vertical coordinate directions, [L]. This equation is a combination of the saturated flow equation developed by Jacob (1940), later clarified by Cooper (1966), and the unsaturated flow equation developed by Richards (1931); these equations were coupled by Freeze (1971). The hydrogeologic parameters that appear in Equation 2.1 will be examined first, followed by a discussion of the assumptions and limitations implicit in the use of Equation 2.1.

The first term to be examined is the pressure head, ψ. It appears as the dependent variable in the governing equation of flow. It is related to the total mechanical energy of the fluid at a point by the expression:

$$h = \psi + z \qquad 2.2$$

where h = hydraulic head = mechanical energy per unit weight of fluid, [L], and z = elevation head = elevation of the point with respect to an arbitrary datum, [L]. The pressure head is defined by:

$$\psi = p/\rho g \qquad 2.3$$

where p = fluid pressure expressed in terms of gage pressure, $[MT^{-2}L^{-1}]$, ρ = fluid density, $[M/L^3]$, and g = gravitational acceleration, $[L/T^2]$.

The solution of Equation 2.1 is the distribution of ψ throughout the flow region at a given time t. From this field,

we can identify the position of the water table as the $\psi = 0$ isobar, and distinguish between the saturated zone, where $\psi > 0$, and the unsaturated zone, where $\psi < 0$.

The second term to be examined is the hydraulic conductivity, K, which is a measure of the ease with which water passes through the porous medium. It is a property of both the fluid and the porous medium and is given by:

$$K = \frac{k\rho g}{\mu} \qquad 2.4$$

where k = permeability, $[L^2]$, and μ = dynamic viscosity of the fluid, $[ML^{-1}T^{-1}]$.

The hydraulic conductivity appears as the proportionality constant in Darcy's law, written here for two-dimensional flow through a saturated-unsaturated, homogeneous and isotropic region:

$$v_x = -K(\psi) \frac{\partial h}{\partial x} \qquad 2.5a$$

$$v_z = -K(\psi) \frac{\partial h}{\partial z} \qquad 2.5b$$

where v_x, v_z = specific discharge in the x and z directions, [L/T]. Note the dependence of the conductivity on the pressure head. An example of a $K(\psi)$ relationship is illustrated in Figure 2a. For $\psi > \psi_a$, K is a constant; for $\psi < \psi_a$, K varies over many orders of magnitude. ψ_a is known as the air-entry value of a soil and is the pressure head at which air first

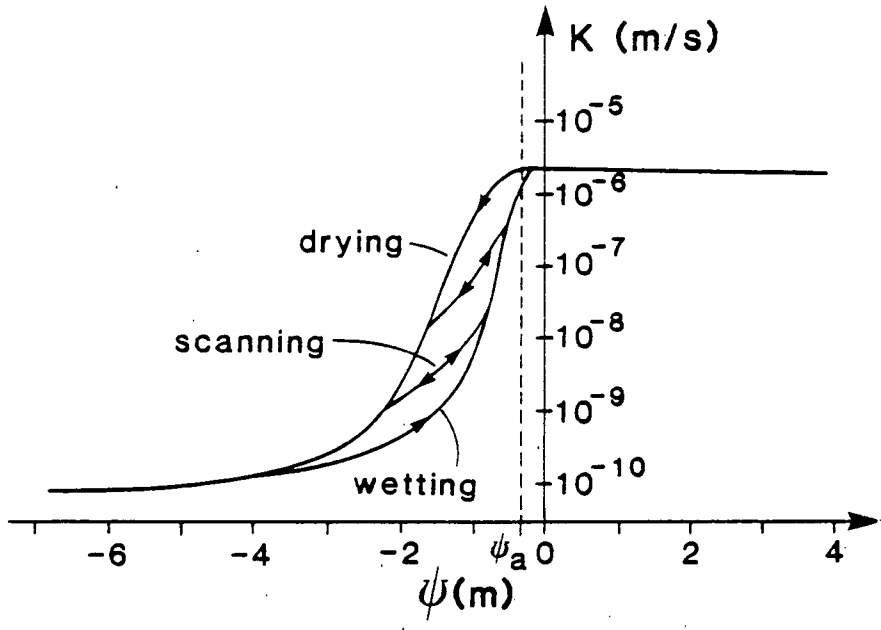

a. K(ψ) relationship

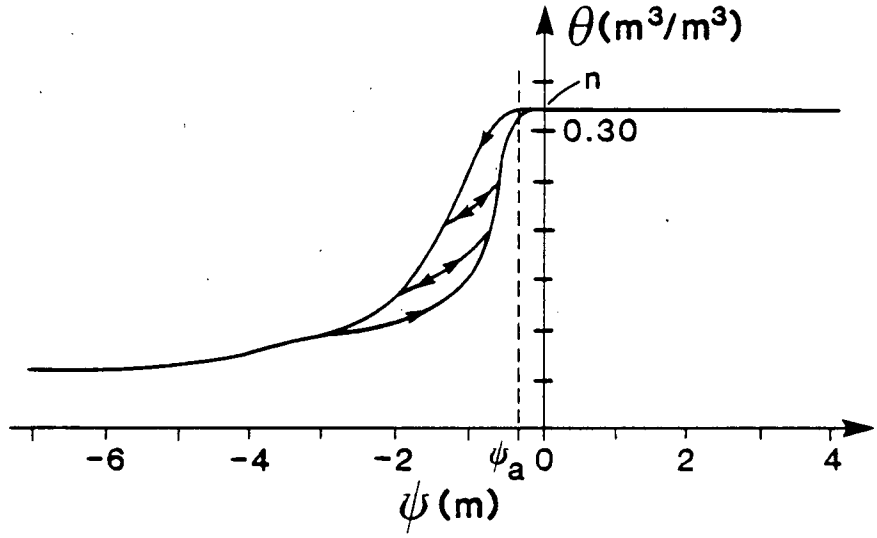

b. $\theta(\psi)$ relationship

Figure 2. Examples of characteristic curves.

enters the pore spaces of a soil as it desaturates. Note also that the $K(\psi)$ relationship is hysteretic. The two bounding curves are known as the primary drying and primary wetting curves. There are an infinite number of scanning curves between these; two have been indicated in Figure 2a.

The dependence of K on ψ in the unsaturated zone is related to the variation of ψ with water content, θ. An example of a $\theta(\psi)$ relationship is shown in Figure 2b. For $\psi > \psi_a$, θ is a constant equal to the porosity of the soil, n. For $\psi < \psi_a$, θ decreases, as shown. As the water content of a soil decreases, the tensional forces acting upon the soil water increase, so that the fluid pressure, and hence the pressure head, decreases. In addition, as the water content decreases, the cross sectional area available for flow also decreases and we observe a steep decline in the hydraulic conductivity. The $K(\psi)$ and $\theta(\psi)$ curves are collectively termed the characteristic curves of a soil. Although attempts have been made, it appears that they cannot be derived analytically from fundamental physical laws; they must be either measured or estimated for each soil. Further information concerning the characteristic curves can be found in standard soil-physics texts such as Hillel (1980).

The last two terms in Equation 2.1 to be examined are the specific moisture capacity, C, and the specific storage, S_s; these relate to the storage properties of the porous medium. The specific moisture capacity describes the dominant mechanism by which water is released from storage in the unsaturated

zone, namely, desaturation. It is defined as the change in water content per unit change in pressure head:

$$C(\psi) = \frac{d\theta}{d\psi} \qquad 2.6$$

It is not a constant, but rather, it is a hysteretic function of ψ and is obtained from the slope of the $\theta(\psi)$ curve.

The specific storage, S_s, reflects the dominant mechanisms by which water is released from storage in the saturated zone. It is defined as the volume of water released from storage per unit volume of the medium as a result of a unit decline in the hydraulic head. A decline in the hydraulic head is accompanied by a decline in the fluid pressure. This, in turn, triggers two mechanisms that release water from storage. First, the effective stress increases causing the release of water as the porous medium compacts. Second, the fluid expands, thereby releasing additional water. The components of the specific storage reflect these two mechanisms:

$$S_s = \rho g(\alpha + n\beta) \qquad 2.7$$

where α = compressibility of the porous medium, $[LT^2/M]$, and β = compressibility of water $[LT^2/M]$. The compressibility of the porous medium is determined from the slope of the stress-strain diagram that relates the void ratio to the effective stress for a soil. The compressibility of water, β, is assumed to be a constant, equal to $4.4 \times 10^{-10} m^2/N$.

Data representing $K(\psi)$, $\theta(\psi)$, $C(\psi)$, and S_s for a variety of geologic materials are available in the literature. Mualem (1976) compiled data on the unsaturated properties of over 80 soils. From this report, characteristic curves can be chosen to represent naturally occurring agricultural soils. The effects of hysteresis will not be considered in this thesis; only the primary drying portion of each curve will be used. The values of S_s can be computed from Table 1, which lists values of α for various types of material.

Table 1. Range of values of compressibility.

	α (m^2/N)
clay	$10^{-6} - 10^{-8}$
sand	$10^{-7} - 10^{-9}$
gravel	$10^{-8} - 10^{-10}$
jointed rock	$10^{-8} - 10^{-10}$
sound rock	$10^{-9} - 10^{-11}$

(Source: Freeze and Cherry, 1979)

The derivation of Equation 2.1, as presented in Freeze and Cherry (1979), requires several assumptions. First, it assumes that the air phase in the unsaturated zone is continuous and is maintained at atmospheric pressure. The effects of entrapped air are therefore neglected. Second, it assumes that Darcy's law is valid. This implies that flow is laminar and the only sources of energy driving fluid flow are differences in the

elevation head and in the pressure head. The model is therefore restricted to flow regions where the following processes are insignificant: a) flow through macropores, b) flow caused by thermal gradients, and c) flow caused by the uptake of water through plant roots. Equation 2.1 is developed for isotropic porous media and it can only be applied to regions where flow is predominantly two-dimensional. The effects of evapotranspiration are also ignored.

Several assumptions are necessary with respect to the compressibility of the porous medium. We assume that the porous medium is compressible but the individual soil grains are not. The porous medium is assumed to be linearly and reversibly elastic. The total stress is assumed to be constant and act in the vertical direction only. We will also assume that the value of S_s remains constant in both the saturated and unsaturated zones. This is a reasonable assumption in the saturated zone, however, effective stress is a complex and incompletely understood function of the negative fluid pressures that occur in the unsaturated zone. Fortunately:

$$C(\psi)\ \frac{\partial \psi}{\partial t} >> \frac{\theta}{n}\ S_s\ \frac{\partial \psi}{\partial t}$$

in the unsaturated zone, so we can use a constant S_s value without introducing significant errors.

In order to solve the flow equation, the physical conditions that exist along the boundaries must be expressed mathematically in terms of ψ. The boundary conditions will be developed with reference to Figure 1.

On the impermeable basal boundary, BC, there is no flow in the z-direction so that

$$\frac{\partial h}{\partial z} = 0$$

or, in terms of ψ,

$$\frac{\partial \psi}{\partial z} = -1 \qquad 2.8$$

Along the vertical impermeable boundaries, AB and CD, there is no flow in the x-direction so that:

$$\frac{\partial h}{\partial x} = 0$$

or, in terms of ψ:

$$\frac{\partial \psi}{\partial x} = 0 \qquad 2.9$$

One can view these boundaries as prescribed-flux boundaries on which the flux is zero.

The base of the stream, AF, is a prescribed-ψ boundary, along which

$$\psi = z_s \qquad 2.10$$

where z_s is the depth of water overlying the horizontal stream bottom. We will assume throughout this study that the boundary conditions given by Equations 2.8 through 2.10 remain constant with time.

The infiltration boundary, ED, and the seepage face boundary, FE, may contain both prescribed-flux and prescribed-ψ

segments. For example, portions of the infiltration boundary may experience incipient ponding so that ψ is prescribed to be zero; other portions may remain unsaturated so that the flux rate is specified as the rainfall rate. Similarly, those portions of the seepage face boundary that contain a seepage face will have a prescribed ψ equal to zero; those portions that remain unsaturated will have a prescribed flux equal to zero. Since conditions along both ED and FE may vary in response to variations in the pressure-head distribution throughout the entire flow region, these represent transient boundary conditions. Their numerical treatment will be discussed in more detail in the following section describing the mathematical method of solution.

In addition to boundary conditions, one needs an initial distribution of $\psi(x,z)$ at $t = 0$ in order to solve Equation 2.1. The distribution can either represent static conditions, whereby the water table is horizontal and is at the same elevation as the stream surface, or, steady-state flow conditions. In the latter case, the steady-state form of the governing equation must be solved:

$$\frac{\partial}{\partial x}\left[K(x,z,\psi)\ \frac{\partial \psi}{\partial x}\right] + \frac{\partial}{\partial z}\left[K(x,z,\psi)\left(\frac{\partial \psi}{\partial z} + 1\right)\right] = 0 \qquad 2.11$$

subject to a set of steady-state boundary conditions similar to those already described.

2.3 The Numerical Method of Solution

The governing equation of flow is a nonlinear partial differential equation. It is very difficult to solve by exact analytical methods, particularly in heterogeneous regions containing complex boundary conditions. Approximate numerical techniques have been developed to solve these types of equations with relative ease. Rubin (1968) and Freeze (1971) solved similar equations describing saturated-unsaturated flow with finite-difference models. Neuman (1972, 1973) adapted the Galerkin finite-element method to the analysis. The computer program named UNSAT I, written and documented by Neuman (1972) was selected and modified for use in the present study. UNSAT I can be used to model two-dimensional, transient, nonhysteretic flow through heterogeneous, anisotropic, saturated-unsaturated regions. The documentation presented by Neuman (1972) gives a complete description of the derivation of the finite-element equations and the use of the model. This information will not be repeated here. Instead, the basic idea behind the method will be presented. The problems particular to the solution of the given boundary-value problem will be discussed, and the limitations introduced by the finite-element analysis will be noted.

In order to apply the finite-element method, the flow region is first divided into a set of triangular and/or quadrilateral subregions known as elements. Each element is defined by the lines joining the corner nodal points and each element is assigned a set of hydraulic properties. The continuous partial differential equation is then replaced at

each node by an approximate algebraic equation to produce a set of N discrete equations, where N = number of nodal points in the flow region. To do this, the governing equation of flow is rewritten as:

$$L(\psi) = 0 \qquad 2.12$$

where L is a differential operator given by

$$L(\psi) = \frac{\partial}{\partial x}\left[K(x,z,\psi)\ \frac{\partial \psi}{\partial x}\right] + \frac{\partial}{\partial z}\left[K(x,z,\psi)\left(\frac{\partial \psi}{\partial z}+1\right)\right] - \left[\left(C(\psi) + \frac{\theta}{n}\ S_s\right)\frac{\partial \psi}{\partial t}\right]$$

An approximate function, $\hat{\psi}(x,z,t)$, which satisfies the boundary and initial conditions is chosen and defined as

$$\hat{\psi}(x,z,t) = \sum_{n=1}^{N} \psi_n(t)\ \delta_n(x,z) \quad n = 1.2....N \qquad 2.13$$

where $\psi_n(t)$ = the exact value of $\psi(t)$ at each nodal point, and $\delta_n(x,z)$ are linearly independent functions of the spatial coordinates, known as basis, shape, or coordinate functions.

When ψ is replaced by $\hat{\psi}$, Equation 2.12 becomes:

$$L(\hat{\psi}) = R(x,z) \neq 0 \qquad 2.14$$

where R(x,z) is the residual, or error, created by the approximation. To minimize the residual throughout the flow region, V, we perform the following integration:

$$\int_V w(x,z)R(x,z)dV = 0 \qquad 2.15$$

where $w(x,z)$ is a weighting function, also a function only of the spatial coordinates. Different methods can be used at this point in the finite-element formulation, depending upon the choice of the weighting function. Neuman (1972) uses the Galerkin method in which the basis functions are chosen as the weighting function. Equation 2.15 becomes:

$$\int_V \delta_i(x,z)R(x,z)dV = 0$$

Writing $R(x,z)$ in terms of equation 2.14 and replacing $\hat{\psi}$ by the expression given in Equation 2.13, we obtain:

$$\int_V \delta_i(x,z)\left[L\left(\sum_{n=1}^{N} \psi_n(t)\,\delta_n(x,z)\right)\right]dV = 0 \qquad 2.16$$

This integral is then evaluated at all nodes to produce a set of simultaneous equations, expressed in matrix form as

$$[A]\ \{\psi\} + [F]\ \left(\frac{\partial \psi}{\partial t}\right) = (Q) - (B)$$

[A] is the conductance, or global stiffness, matrix. It is an N x N matrix and is sparse, banded, and symmetric. [F] is the capacitance matrix. It expresses the ability of the region to absorb or release water from storage due to a change in pressure head. It is an N x N, diagonal matrix. $\{\psi\}$ is the vector containing the unknown values of ψ at individual nodes.

{Q} is a vector that contains the flux across the boundary nodes of the flow region. It is equal to zero at all internal nodes that do not act as sources or sinks. {B} contains the flux at each node due to gravity alone.

A fully implicit time scheme is used to evaluate the time derivative, $\partial\psi/\partial t$. The time domain is discretized into a sequence of timesteps. At the beginning of each timestep, predictions of the new values of ψ are made, based on the values from the previous timestep. Modifications are then made to the matrix equation to incorporate the boundary conditions and the matrix equation is solved by Gaussian elimination for $\{\psi\}$. These results are improved by an iterative process until a satisfactory degree of convergence is achieved. Further information concerning the details of finite-element modeling can be found in texts such as Wang and Anderson (1982), Pinder and Gray (1977), Zienkiewicz (1977), and Bathe and Wilson (1976).

The problems particular to the solution of the given boundary-value problem relate to the treatment of the boundary conditions. Constant-head boundaries and fixed impermeable boundaries are easily handled by the finite-element method; the equations corresponding to these boundary nodes are modified to ensure that ψ = prescribed value and Q = 0, respectively. However, the transient boundary conditions that occur along the seepage-face boundary and the infiltration boundary require special treatment.

The seepage-face boundary is special because the position and length of a seepage face may vary unpredictably as the pressure head varies with time throughout the region. The boundary condition is therefore a function of the dependent variable and cannot be fixed a priori; an iterative scheme is required to arrive at the proper boundary condition. Neuman (1972) employed the following scheme to predict the position at each timestep. During the first iteration, set $\psi = 0$ along the seepage face and treat this segment of the boundary as a prescribed-ψ boundary. Set $Q = 0$ along the unsaturated portion of the boundary and treat this segment as a prescribed-flux boundary. The matrix equation is then solved with the expectations that a) the newly calculated value of Q is negative, indicating that flow is directed out of the porous medium, only along the prescribed-ψ segment, and b) the newly calculated value of ψ is negative only where Q was previously set equal to zero. If these expectations are not met, the boundary conditions at the errant nodes are redefined to agree with the new solution. This procedure is repeated until the solution converges within a given timestep. The iterative scheme exploits the ease with which the finite-element method can formulate and modify boundary conditions.

In order to improve the convergence rate, Neuman (1972) designed the iterative procedure so that the boundary conditions are always modified sequentially, from node to node, beginning at the base and proceeding to the top of the seepage-face boundary. In addition, if it becomes necessary during an

iteration to set Q = 0 at any node, Q at all the higher nodes on the boundary are automatically set equal to zero. This aspect of the iterative scheme was removed for the present study to allow for the development of more than one seepage face along the hillslope. Prior to this modification, it was possible to model more than one seepage face along a slope, provided that the lowermost node associated with each seepage face could be specified a priori. The modification removed this restriction.

The infiltration boundary also requires special treatment because the flux across the soil surface cannot be specified a priori; it depends upon the antecedent moisture conditions and the infiltration capacity of the soil. During the first iteration in each timestep, the infiltration boundary is treated as a prescribed-flux boundary. Each node is assigned an arbitrary fraction of the rainfall rate. The matrix equations are solved and if the computed value of ψ is negative at some nodes along the boundary, the prescribed flux is increased. If a portion of the infiltration boundary becomes ponded during an iteration, then that portion is treated as a prescribed-ψ boundary with $\psi = 0$. This process is repeated until convergence occurs and each node along the infiltration boundary is either unsaturated and transmitting the full rainfall rate, or is ponded and transmitting water at a rate less than the imposed rainfall rate. This iterative scheme was introduced by Neuman et.al. (1974, 1975) in a program titled UNSAT II. UNSAT I was modified for the present study to incorporate the algorithm.

Several limitations are introduced by the finite-element analysis. A node that is located on the seepage-face boundary cannot be included in the infiltration boundary. Therefore, rainfall must be restricted to the flat, upland surface and infiltration cannot be modeled along the slope. In addition, there is no mechanism to route surface runoff. When ponding occurs on the infiltration surface, or when water discharges across a seepage face, the subsequent path of the runoff is not modeled. Furthermore, the model does not take into account the interactions between the subsurface flow system and changes in the stream level.

The model is also limited by the nature of the characteristic curves. Recall from Figure 2, that where the soil is very dry, the pressure-head gradient is steep. In addition, the hydraulic conductivity varies in the unsaturated zone over several orders of magnitude for small changes in pressure head. These two factors can combine to produce slow convergence rates, or, in some instances, numerical instability. To help avoid such problems, one can increase the number of nodes and space them more closely in the portions of the flow region where dry conditions are anticipated. The total number of nodes, however, is limited by the available computer storage capacity. Alternatively, one may modify the shape of the characteristic curves to reduce their step-like form. Instability problems were encountered during the sensitivity studies and will be discussed in more detail, following the laboratory verification of the numerical model.

Chapter 3

MODEL VERIFICATION

When numerical modeling is used to solve new types of boundary-value problems, it is important to verify that the mechanisms supported by these solutions are physically correct. In many instances, our understanding of the physics of groundwater flow is sufficient to evaluate whether or not a solution is reasonable. This is not the case when hydrogeologic factors combine to produce more than one seepage face; the complexity of the boundary conditions and the saturated-unsaturated flow systems prohibit an intuitive approach to model verification.

There are several ways to verify a model. The numerical model could be verified if it were tested against: a) an analytical solution, b) field observations, or c) a physical laboratory model. An analytical solution is not available in this case because of the complexity of the flow region and boundary conditions. A quantitative check in the field would require knowledge of the boundaries of the region of flow, the geometry of the soil units, the antecedent moisture conditions, the hydraulic properties of each soil unit, and measurements of hydraulic head, inflow, and outflow. It is unlikely that these field data would be known with sufficient accuracy to provide unequivocal verification of the numerical analysis. However, with a physical laboratory model, much of the uncertainty surrounding these data requirements can be eliminated through proper experimental design and material testing. The

laboratory approach was therefore selected to be the most feasible means of verification.

Physical models have been used in this manner in several previous studies. For example, Freeze and Banner (1970) used a soil column to verify transient, one-dimensional, unsaturated flow to a recharging groundwater flow system. Nieber and Walter (1981) designed a physical model to verify the transient runoff response of a homogeneous hillside. In both cases, a flow domain was constructed and subjected to a set of boundary and initial conditions. The hydraulic-head distribution was measured and compared to that predicted by the numerical model. A favorable comparison then lent credence to the conclusions drawn from the numerical analysis of more complex flow regions.

In the present study, a sand-box model was built to verify two-dimensional, steady-state, saturated and unsaturated flow through a heterogeneous hillside in which two seepage faces were allowed to develop. The predicted and observed pressure-head distribution, seepage-face locations, and discharge rates were then compared in order to judge the validity of the mathematical model.

Details of the experiment are given in this chapter. First, the experimental design is described. Second, results of a trial run are presented. This run was designed to troubleshoot technical problems and consequently contained only a sparse sampling of the hydraulic-head distribution. Third, results are presented from a final run in which the hydraulic-head distribution was monitored extensively.

3.1 The Experimental Design

The experimental flow region, illustrated in Figure 3, consists of a vertical cross section through a hillside that is 2.44 m long, 1.0 m high, and 0.1 m wide. It is composed of medium sand, within which there is a horizontal layer of fine sand intended to impede flow and create a seepage face. Four types of boundary conditions are present:

1. AB, BC, and CD are impermeable boundaries
2. AF is a prescribed-head boundary
3. DE is an infiltration boundary
4. EF is a seepage-face boundary

Steady-state, nonhysteretic flow conditions were monitored for a series of decreasing rainfall rates applied to an initially saturated hillside.

The design of the physical model operated within many constraints. Design decisions were subject to the limitations inherent in the laboratory equipment and the uncertainties introduced by experimental error. Many of the constraints could not be predicted at the onset of the experiment. As a result, the experimental design was not complete until after the trial run; by this time, all constraints had been identified.

The description of the experimental design has been organized in the following manner. First, the selection and testing of the medium and fine sand is described. Then, an

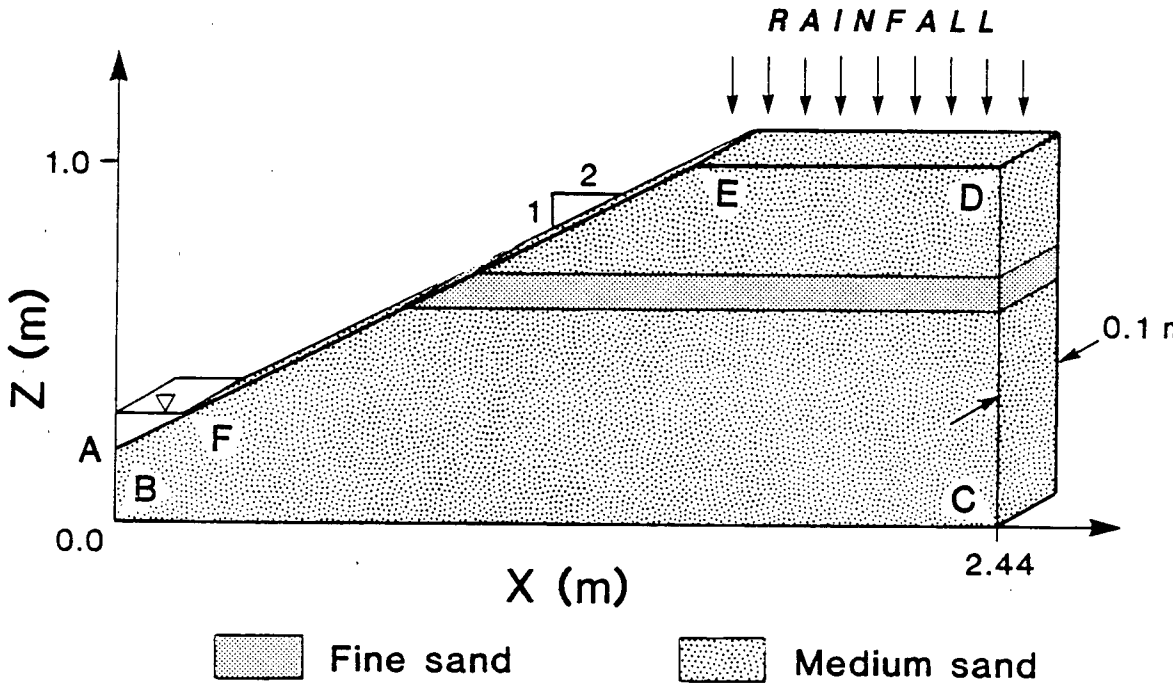

Figure 3. The experimental flow region.

analysis of the experimental error associated with the determination of the hydraulic properties is presented. This is followed by a description of the devices designed to generate and maintain the boundary conditions. Equipment not purchased was built by Ray Rodway, a machinist in the Department of Geological Sciences, at the University of British Columbia. His craftsmanship was fundamental to the success of the experiment.

SELECTION AND TESTING OF THE MEDIUM SAND

The medium sand was sieved from a supply of Ottawa Silica Sand. The fraction that was chosen passed through a 30-mesh sieve and was retained on a 40-mesh sieve, so that the grain size ranged from 0.4 to 0.6 mm. Following the MIT or British Standards classification scheme (Craig, 1978), this represents a medium sand.

A poorly-graded sand was chosen for its ability to approximate a homogeneous and isotropic porous medium. However, the more uniform the grain size, the more step-like the characteristic curves become. This may cause instability in the numerical analysis. The finite-element program was therefore tested with a set of step-like characteristic curves and the effect was to increase the number of iterations required for convergence from approximately three to seven. This was judged to be an acceptable tradeoff for the homogeneity and isotropy gained through the use of a poorly-graded sand.

Once the medium sand was selected, the hydraulic conductivity, the porosity, and the characteristic curves were measured. Samples were prepared for testing by slowly adding wet sand to a column of water and allowing the sand to settle in a state of loosest-packing. It was felt that attempts to compact the sand would lead to a more heterogeneous sample that would be difficult to reproduce in the sand tank. Distilled water was used for soil testing, unless otherwise noted.

The saturated conductivity, K, of the medium sand was determined from a constant-head permeameter test. The procedure involves the application of a constant-head differential to a saturated soil sample and measurement of the resulting volumetric flow rate. A detailed description of the standard laboratory procedure is given by Lambe (1951).

The porosity, n, was calculated from the relationship:

$$n = 1 - \rho_b/\rho_p$$

when ρ_b = dry bulk density [M/L^3] and ρ_p = particle density [M/L3]. The sand was essentially pure silica so that ρ_p = 2.65 gm/cm^3.

The saturated conductivity and porosity were determined for five samples. The results are summarized below in Table 2 and are discussed later in regard to the error analysis.

Table 2. Constant-head test results on the medium sand.

Sample #	porosity, n	K(m/s)
1	.435	2.83×10^{-3}
2	.431	2.81×10^{-3}
3	.427	3.14×10^{-3}
4	.431	2.99×10^{-3}
5	.428	3.07×10^{-3}

There are several laboratory procedures for determining the characteristic curves, $K(\psi)$ and $\theta(\psi)$. Klute (1972) provides a comprehensive review.

The method used to determine $K(\psi)$ was first described by Childs and Collis-George (1950). It is based on Darcy's law for one-dimensional, vertical, unsaturated flow through homogeneous and isotropic soil, written as

$$v_z = Q/A = - K(\psi) \left[\frac{\partial \psi}{\partial z} + 1\right] \qquad 3.1$$

where Q = volumetric flow rate, $[L^3/T]$, and A = cross sectional area of the sample, $[L^2]$. When water is supplied to a long, vertical column of homogeneous soil such that the specific discharge is less than the saturated conductivity, steady-state flow conditions are characterized by a transmission zone in which the water content and pressure head are uniform. In this zone, $\partial\psi/\partial z = 0$ and Equation 3.1 simplifies to:

$$v_z = Q/A = K(\psi)$$

The conductivity in the transmission zone is therefore equal to the specific discharge. To obtain a point on the $K(\psi)$ curve, one needs to measure ψ in the transmission zone and calculate the specific discharge from measurements of Q and A. The entire primary drying curve is obtained by proceeding through a series of steady-state conditions in which the specific discharge is successively reduced from a maximum value near the saturated conductivity. The column used for this procedure was 1.3 m long with an inside diameter, ID, = 6.0 cm. Water was supplied to the top of the column at a rate controlled by a constant-discharge pump. Outflow from the base of the column was collected from an adjustable water reservoir.

To measure pressure head, tensiometers were installed in the column wall, as shown in Figure 4. The tensiometers used in this study consist of hollow ceramic tubes, 7 inches long with an ID = 3/16 inch and an outside diameter, OD $\leq$ 5/16 inch. One end is sealed with glass and the other end may be cut to the required length and attached to a manometer. When in use, the tensiometer is saturated and the lines to the manometer are filled with water. Water flows across the porous ceramic walls until the fluid pressure inside the tensiometer has equilibrated with the fluid pressure of the soil water. In the case of positive fluid pressure, water flows from the soil into the tensiometer until equilibrium is reached. In the case of negative fluid pressure, water flows from the tensiometer to the soil.

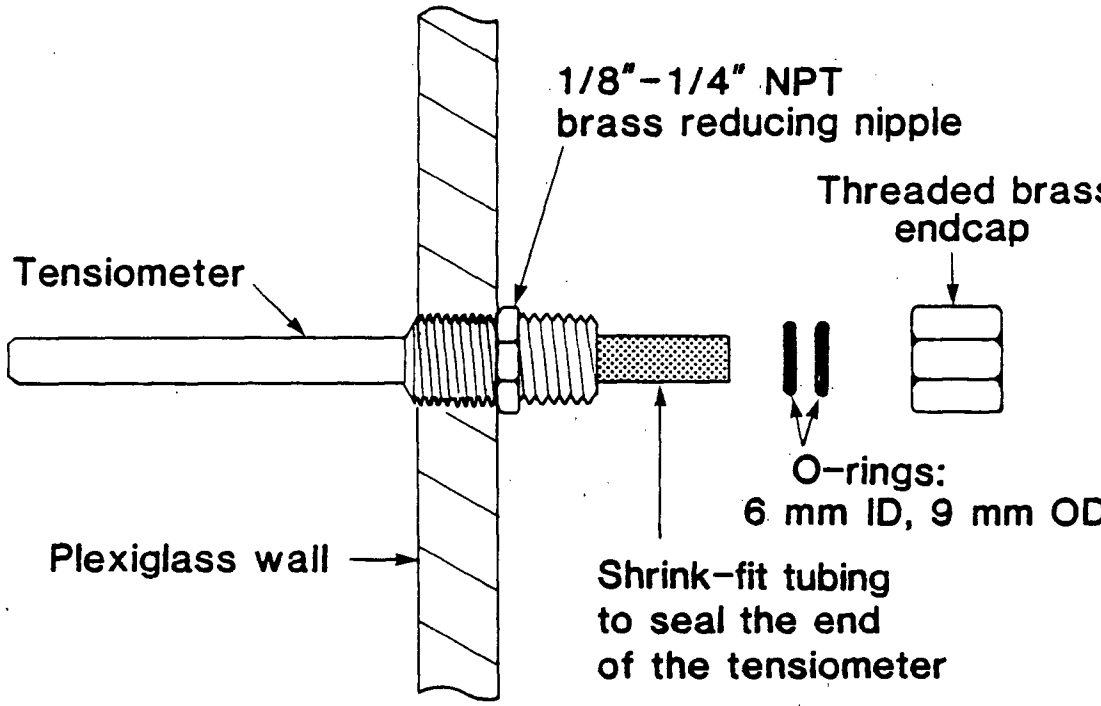

Figure 4. Tensiometer installation.

Tensiometers cease to function when either the air-entry value of the ceramic is exceeded, or when the water content of the soil becomes too low to provide sufficient hydraulic contact for equilibration to occur. The air-entry value of the ceramic was reported by the manufacturer to be between 0.82 bar and 0.95 bar. This means that for $\psi < -830$ cm, air may enter the tensiometer through the ceramic and invalidate future readings. The second criterion proved to be far more restrictive as the soil became too dry to equilibrate at $\psi = -18$ cm. The design of the physical model was therefore constrained to demonstrate the development of multiple seepage faces in a saturated-unsaturated regime in which $\psi > -18$ cm. This constraint was acceptable because it includes almost the full range of moisture-content values experienced by the soil as it desaturated.

Three experimentally determined $K(\psi)$ curves are shown in Figure 5. Error bars indicating one standard deviation about each data point have been added to one of the curves to indicate the magnitude of the measurement errors involved in the $K(\psi)$ determination. A complete discussion of the error analysis is presented later. An air-entry value of $\psi_a = -11.5$ cm was measured as the distance over which the soil remains saturated above a static water table.

The $\theta(\psi)$ curve was determined using a Tempe Cell. A Tempe Cell consists of a 3-cm long brass ring, 5.4 cm in diameter, that contains the soil sample between two plexiglass endcaps.

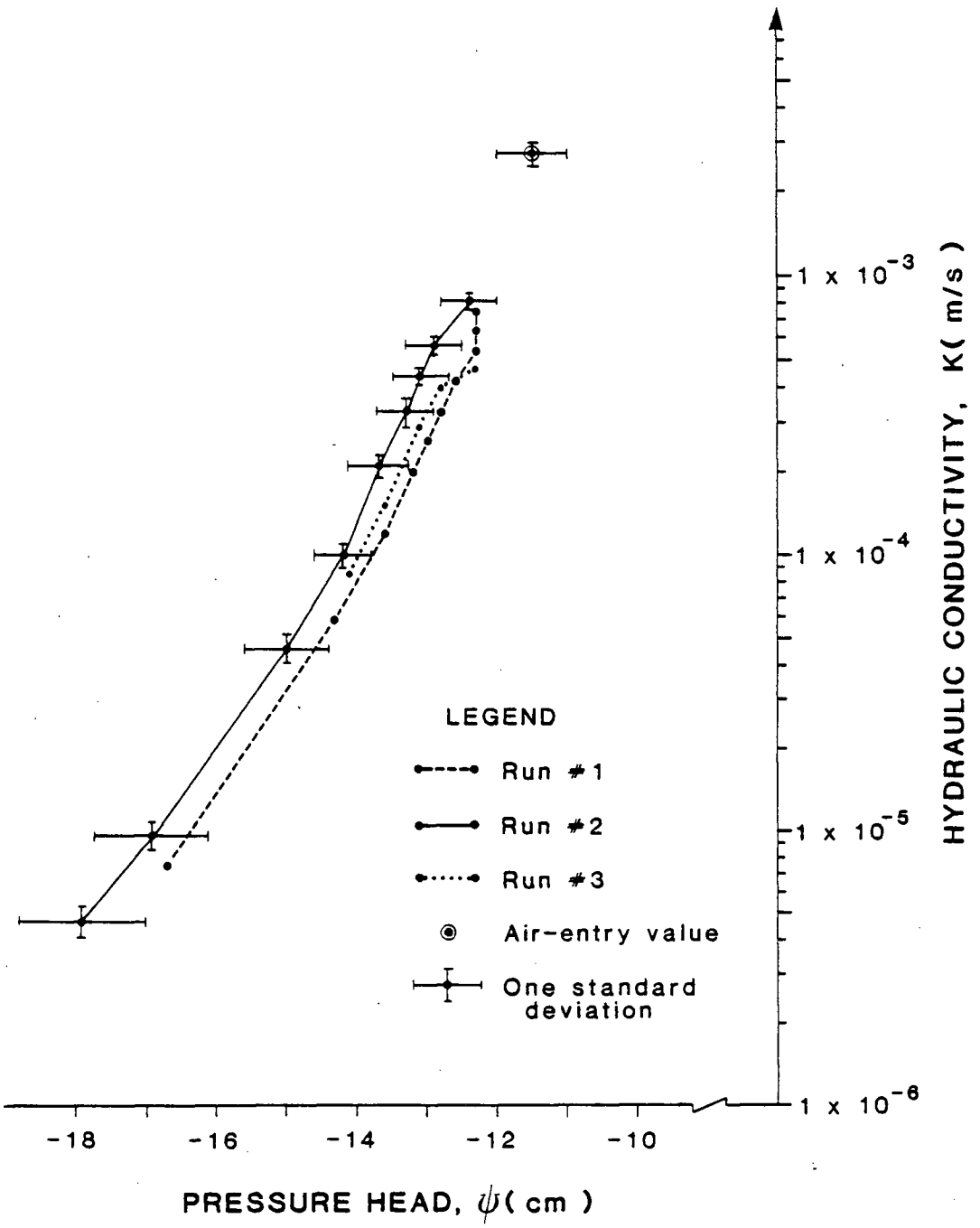

Figure 5. Measured $K(\psi)$ data for the medium sand.

The lower endcap contains a 1/2-bar ceramic plate on which the soil rests. There is a small reservoir of water beneath the ceramic plate that is connected by water-filled tubing to an outflow collection flask. Negative fluid pressure is applied to the base of the ceramic plate by lowering the outflow flask relative to the soil sample.

To prepare the Tempe Cell, the porous plate was vacuum saturated and the outflow lines and the brass sample container were filled with de-aired water. Sand was placed loosely into the brass container. The bulk density was measured to provide a means of determining the porosity and initial weight of water contained in the sample.

On lowering the sample, water drained from the sand until the fluid pressure had equilibrated across the ceramic plate. Twelve to twenty-four hours were allowed for equilibration. The amount of water released was measured gravimetrically and used to calculate the water content for each decrement in pressure head. The pressure head was measured as the vertical distance from the outflow level to the center of the soil sample. Measured in this way, ψ represents an average over the length of the sample.

Figure 6 shows two experimentally determined $\theta(\psi)$ curves with one showing error bars. The method used to quantify the error is discussed later.

SELECTION AND TESTING OF THE FINE SAND

Numerical studies were used extensively to guide the selection of the fine sand. These simulations were used to

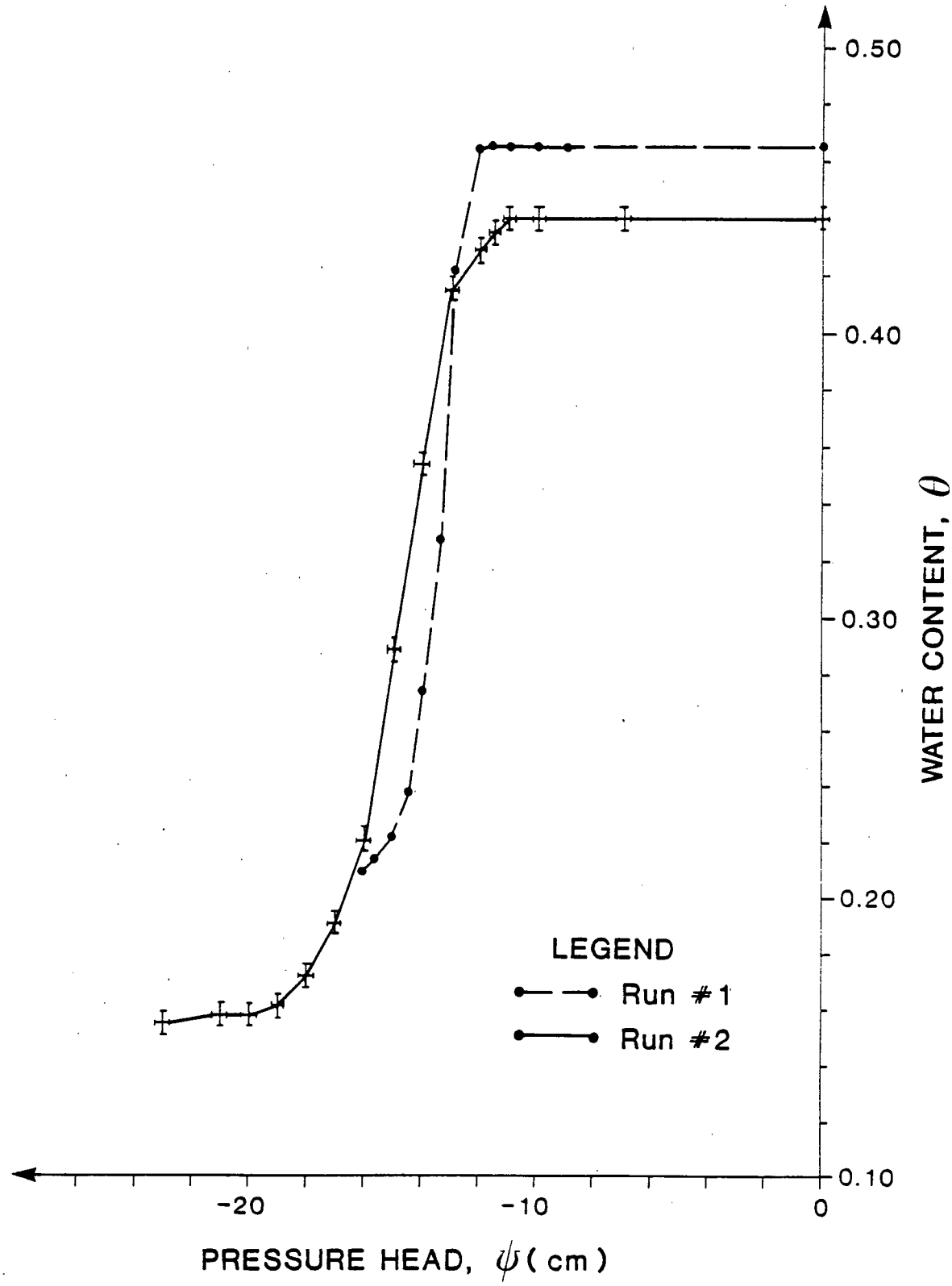

Figure 6. Measured $\theta(\psi)$ data for the medium sand.

provide theoretical predictions of the response of the physical model to various design options. Specifically, numerical studies helped to determine the optimum thickness and location of the fine sand layer and the associated range of K values that theoretically would produce multiple seepage faces. To avoid confusion, the saturated conductivity of the fine sand will be termed K_2 and that of the medium sand will be termed K_1. For the numerical simulations, characteristic curves averaged from those shown in Figures 5 and 6 were used to represent the medium sand.

Criteria for selection were based upon characteristics judged to be desirable for the final flow region. Figure 7a shows three such characteristics. First, two seepage faces, labeled BC and EF, are present. Second, the uppermost portion of the water table, labeled BA, does not intersect the infiltration boundary to produce ponding. Third, an unsaturated wedge, labeled CDE, is formed beneath the uppermost seepage face. These three characteristics are hereafter implicit in the phrase "an acceptable solution."

Two types of unacceptable solutions were also identified during preliminary numerical studies. The first type occurs if the conductivity contrast, K_1/K_2, is so low that solutions typified by Figure 7b are produced. Two seepage faces will not form, regardless of the rainfall rate. Note also that ponding has occurred along the infiltration boundary. This is undesirable because the numerical model does not model surface runoff. A second type of undesirable solution is shown in

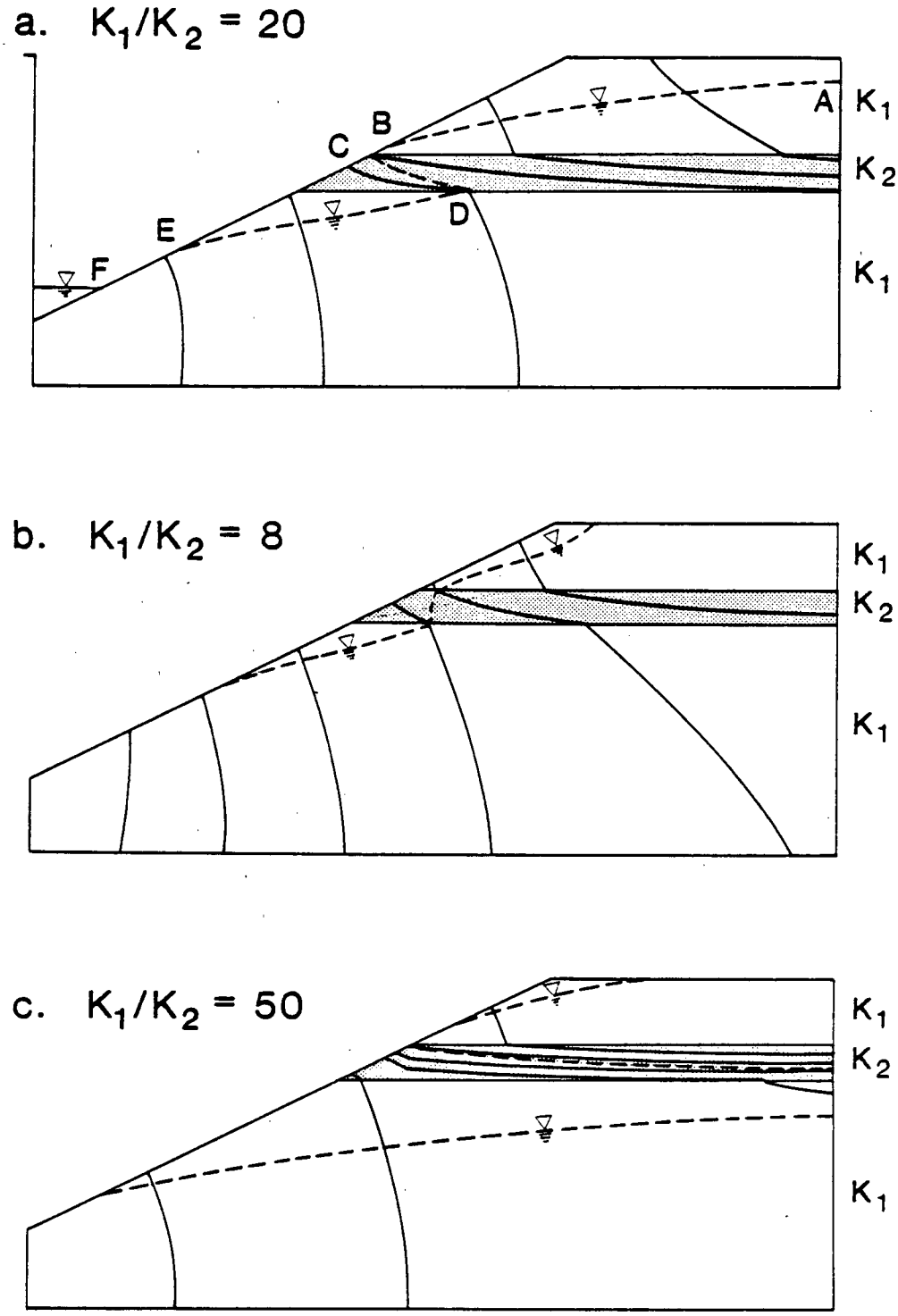

Figure 7. Desirable and undesirable characteristics of the experimental flow region.

Figure 7c. In this case, K_1/K_2 is so great that the fine layer forms an almost impervious boundary, and a single, continuous saturated zone cannot form. A flow region of this type is undesirable because it would not allow observation of the growth of the unsaturated wedge along the base of the impeding layer as the rainfall rate is decreased.

With these desirable and undesirable qualities in mind, a numerical study was designed to determine the optimum thickness and location of the impeding layer. The thickness of the impeding layer, T, and the elevation of the base of the layer, $\bar{z}$, were varied, as shown in Figure 8. Preliminary studies had indicated that a value of $K_1/K_2 = 20$ would avoid the undesirable solutions shown in Figure 7b and 7c, so this value was chosen and maintained constant throughout the analysis.

The response of each mesh to a series of four rainfall rates is summarized in Figures 9, 10, and 11. Figure 9 isolates the effect of T and $\bar{z}$ on the length over which the infiltration boundary is ponded. Mesh B produces the least amount of ponding for any given rainfall rate. Figure 10 shows the effect of T and $\bar{z}$ on the length of the uppermost seepage face. Meshes B and C are equally desirable because they tend to produce a relatively persistent uppermost seepage face. Figure 11 shows the effect of T and $\bar{z}$ on the distance the unsaturated wedge extends into the hillside. Mesh B is the most desirable in this regard because it produces the smallest unsaturated wedge. While a large unsaturated wedge might be more interesting to monitor, it is also more likely to contain

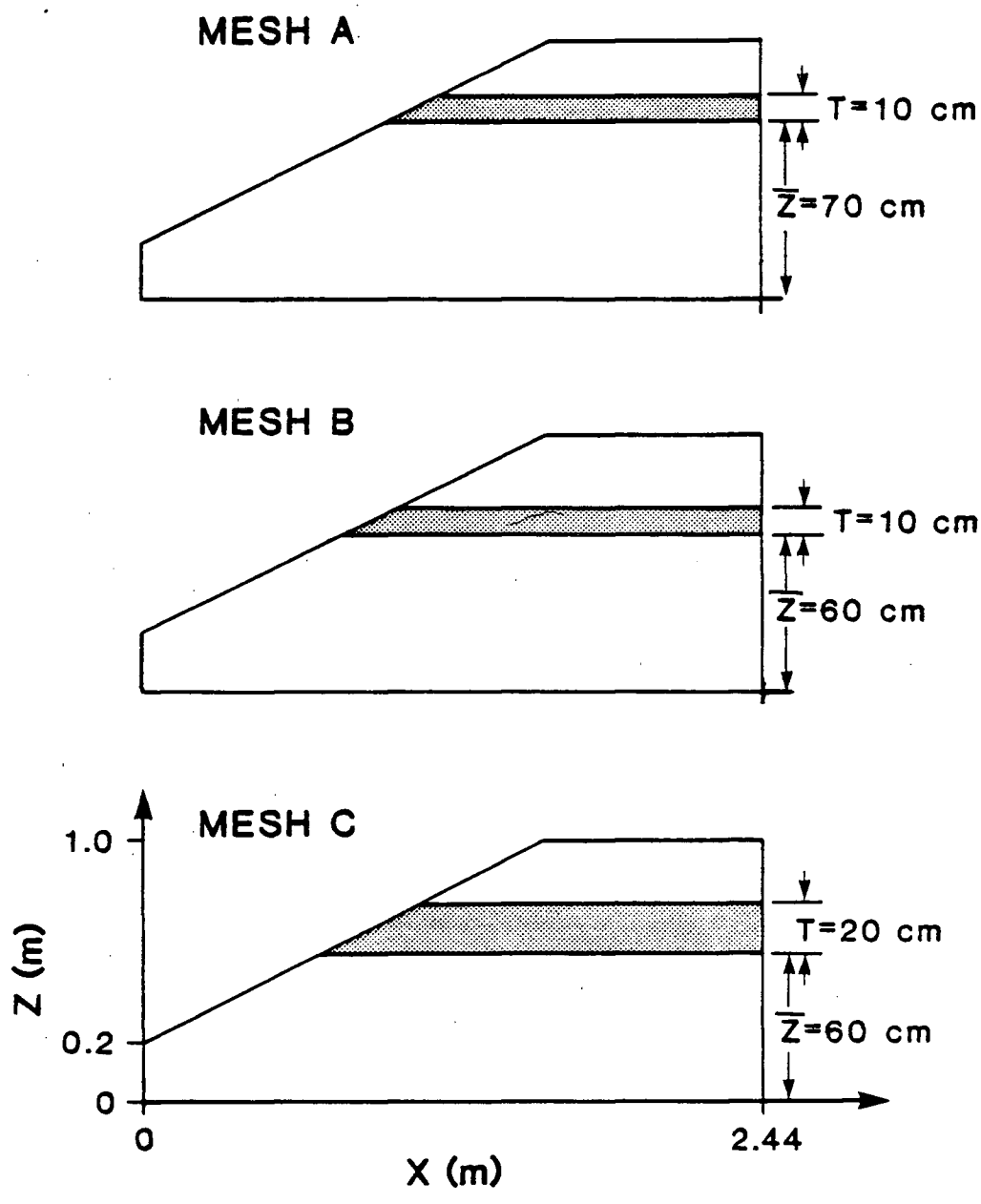

Figure 8. Three meshes used to determine the optimum thickness and location of the impeding layer.

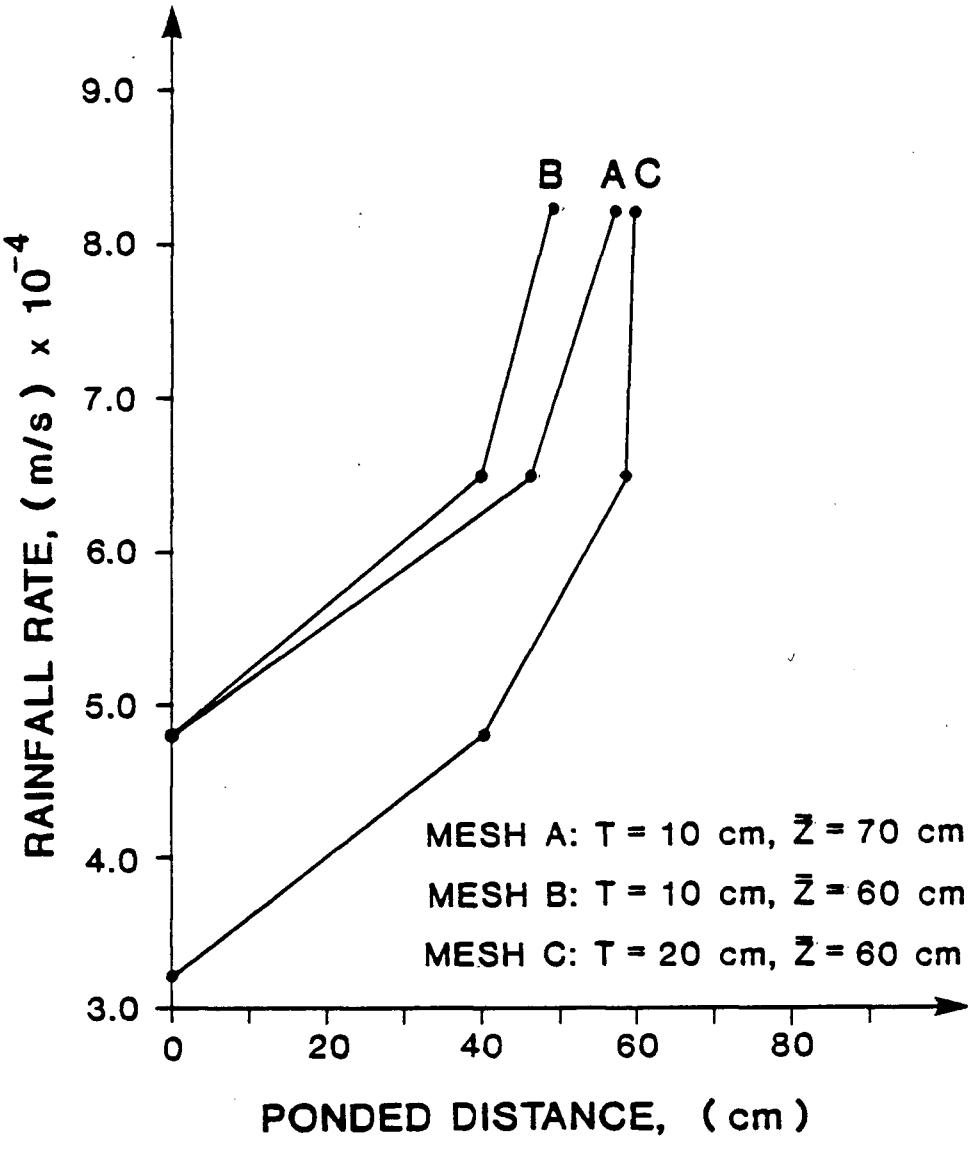

Figure 9. The effect of T and $\bar{z}$ on the length over which the infiltration boundary is ponded.

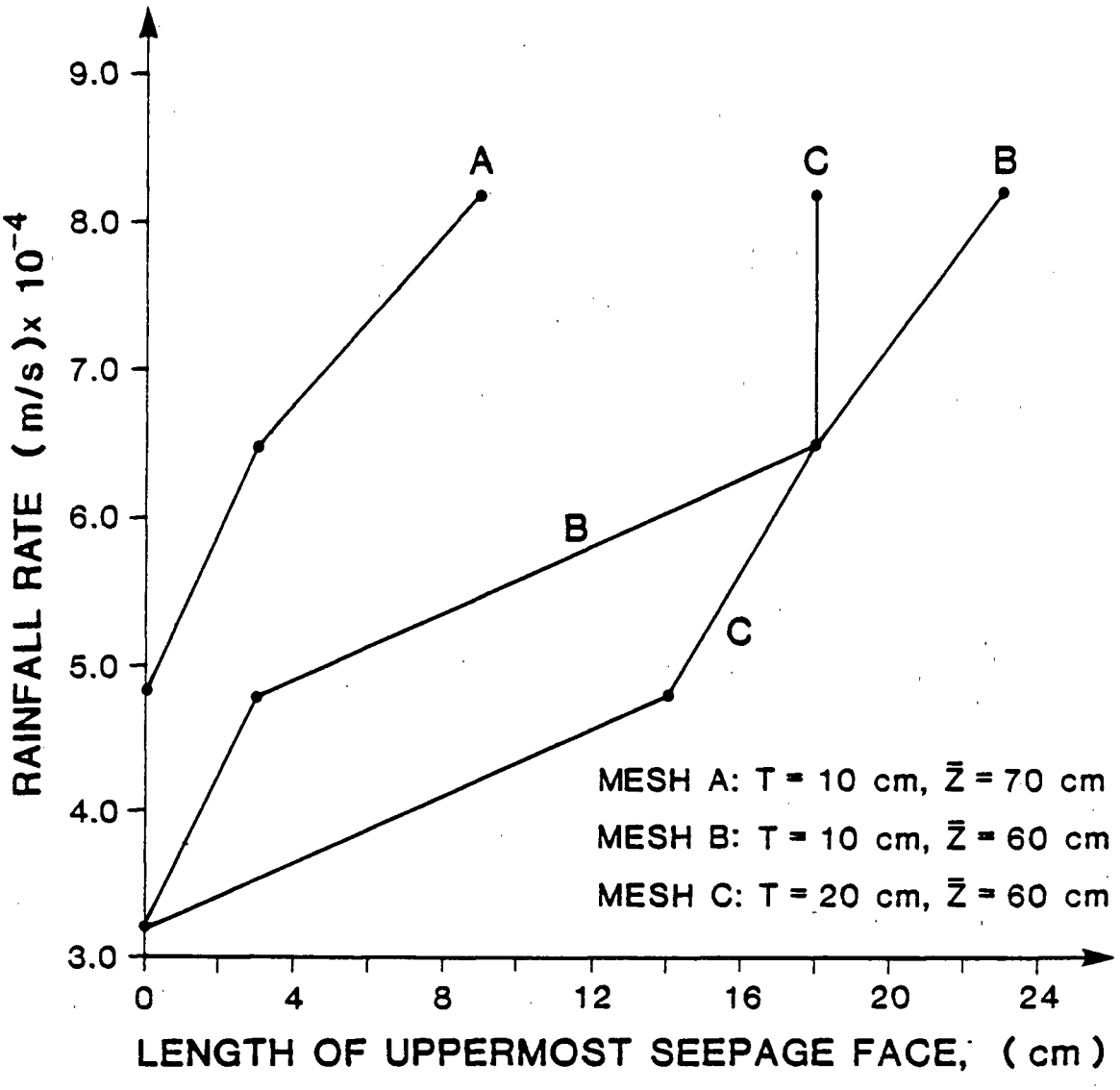

Figure 10. The effect of of T and $\bar{z}$ on the length of the uppermost seepage face.

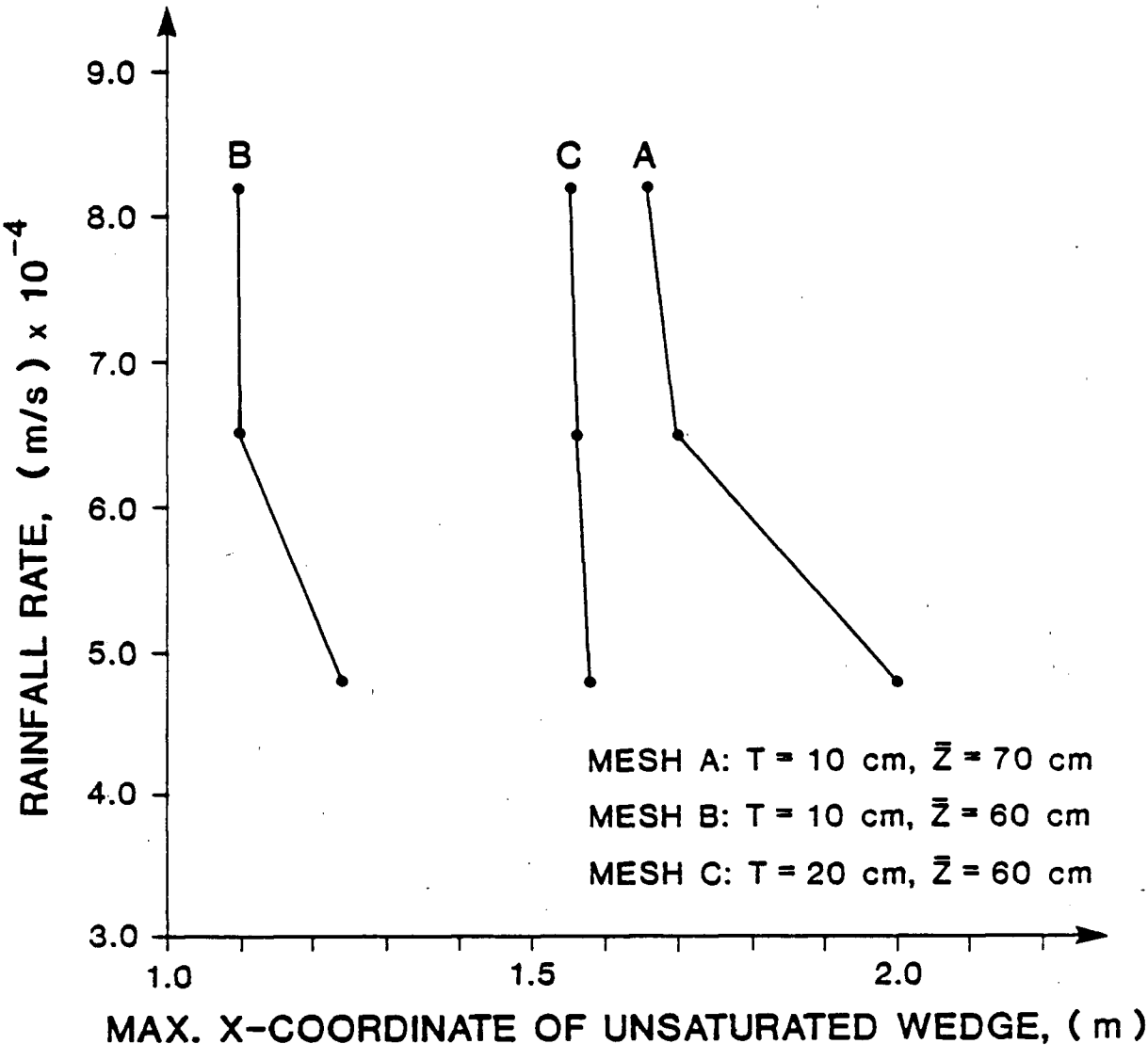

Figure 11. The effect of T and $\bar{z}$ on the distance the unsaturated wedge extends into the hillside.

values of $\psi < -18$ cm which cannot be measured with the tensiometers. Based on these observations, Mesh B was chosen as the optimum flow region.

Next, a study was made to quantify the range of K_2 values that would produce an acceptable solution for a rainfall rate of 2.8 cm/min, or 4.7×10^{-4} m/s. Preliminary studies had indicated that this rainfall rate would produce an acceptable solution and it fell within the range of the performance of the rainfall generator. In the analysis, the rainfall rate and the value of $K_1 = 2.8 \times 10^{-3}$ m/s remained fixed; K_2 was varied and shown to produce acceptable solutions for values between 8.3×10^{-5} m/s and 1.3×10^{-4} m/s. Values below this range produced surface ponding; above this range, the uppermost seepage face was lost. The optimum design for the experimental flow region is shown in Figure 12 for which $K_2 = 1.0 \times 10^{-4}$ m/s.

To help locate a sand having a saturated conductivity near 1.0×10^{-4} m/s, the following rough estimate was used:

$$K \approx 100 D_{10}^2 \qquad 3.2$$

where K is measured in cm/s and D_{10} is the particle size, in cm, such that 10% of the sand particles are smaller than that size. According to Equation 3.2, a sand with $K \approx 1.0 \times 10^{-4}$ m/s should be associated with $D_{10} \approx 0.1$ mm.

Four sieves, with openings ranging between 0.2 mm and 0.075 mm, were then used to separate a mixture of fine Ottawa Silica Sand. The fraction with a grain size between 0.1 mm and

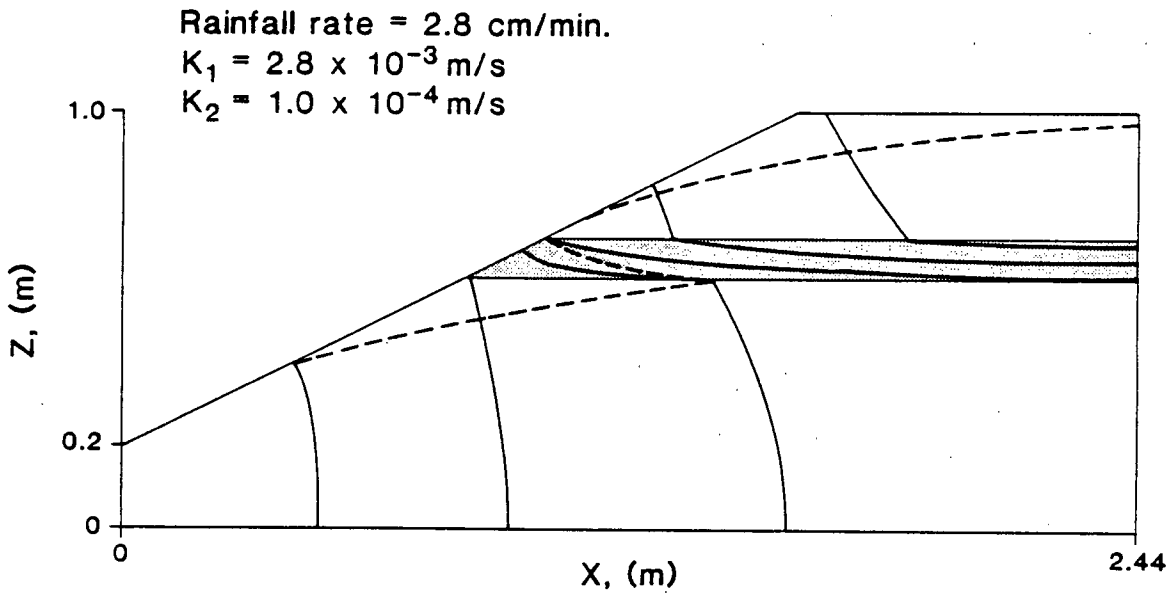

Figure 12. The optimum design for the experimental flow region

0.075 had a saturated conductivity approximately equal to 1.2 x 10^{-4} m/s. This was the sand that was selected to form the impeding layer with the expectation that a solution similar to Figure 12 could be obtained experimentally.

Constant-head permeameter tests were performed on five samples of the fine sand. The results are summarized below, in Table 3, and are discussed later in regard to the error analysis.

Table 3. Constant-head test results on the fine sand.

Sample	n	K(m/s)
1	.469	1.24×10^{-4}
2	.463	1.23×10^{-4}
3	.449	1.12×10^{-4}
4	.451	1.30×10^{-4}
5	.447	1.20×10^{-4}

An air-entry value of $\psi_a = -90$ cm was measured for the fine sand. Because the physical model was designed to operate at $\psi > -18$ cm, the impeding layer would remain saturated and measurement of the characteristic curves was unnecessary.

ERROR ANALYSIS

Before one can judge whether an experimental result agrees with a theoretical prediction, the accuracy of both must be estimated. The experimental result, in this case, is the steady-state response of the physical model to a set of boundary conditions. The accuracy with which we can measure

the experimental result depends upon the accuracy of the pressure-sensing system and the seepage-collection system. A discussion of the accuracy of these systems is included in the discussion of the final experimental run. The accuracy of the theoretical prediction, on the other hand, depends primarily upon the accuracy with which the boundary conditions are maintained in the laboratory model and the accuracy of the experimentally determined hydraulic properties. The former is a technical problem and is discussed with the trial run; the latter will now be discussed.

Often, the hydraulic properties of a porous medium are calculated from several individual observations, each of which contributes to the inaccuracy of the computed result. For example, the value of K obtained from the constant-head test contains errors from the measurement of outflow volume, time, cross-sectional area, the constant-head differential, and the length of the sample. Propagation-of-error analysis is designed to quantify the contribution of these individual errors to the computed result. A complete discussion of the method is contained in Young (1962); a summary is presented below.

Suppose a quantity, P, is calculated from the measured quantities a,b,c,... . The expression relating the variance of the calculated quantity, σ_p^2, to the variances of the measured quantities, σ_a^2, σ_b^2, σ_c^2,..., is given as:

$$\sigma_p^2 = \left(\frac{\partial P}{\partial a}\right)^2 \sigma_a^2 + \left(\frac{\partial P}{\partial b}\right)^2 \sigma_b^2 + \left(\frac{\partial P}{\partial c}\right)^2 \sigma_c^2 + \ldots \qquad 3.3$$

The fractional standard deviation of the mean, σ_p/p, can be obtained from the following expression:

$$\left(\frac{\sigma_p}{P}\right)^2 = \left(\frac{1}{P}\frac{\partial P}{\partial a}\right)^2 \sigma_a^2 + \left(\frac{1}{P}\frac{\partial P}{\partial b}\right)^2 \sigma_b^2 + \left(\frac{1}{P}\frac{\partial P}{\partial c}\right)^2 \sigma_c^2 + \ldots \qquad 3.4$$

To illustrate the use of Equations 3.3 and 3.4, consider the calculation of K from the constant-head test, where:

$$K = \frac{\bar{Q}\ell}{tA\Delta h} \qquad 3.5$$

where:

$\bar{Q}$ = outflow volume [L^3]

t = time [T]

A = cross-sectional area [L^2]

Δh = constant-head differential [L]

ℓ = length of the sample [L]

From Equation 3.3, the variance of K is given as:

$$\sigma_K^2 = \left(\frac{\partial K}{\partial \bar{Q}}\right)^2 \sigma_{\bar{Q}}^2 + \left(\frac{\partial K}{\partial t}\right)^2 \sigma_t^2 + \left(\frac{\partial K}{\partial A}\right)^2 \sigma_A^2 + \left(\frac{\partial K}{\partial \Delta h}\right)^2 \sigma_{\Delta h}^2 + \left(\frac{\partial K}{\partial \ell}\right)^2 \sigma_\ell^2 \qquad 3.6$$

Inserting the partial derivatives indicated in Equation 3.6 leads to:

$$\sigma_K^2 = \left(\frac{\ell}{tA\Delta h}\right)^2 \sigma_{\bar{Q}}^2 + \left(\frac{-\bar{Q}\ell}{t^2 A\Delta h}\right)^2 \sigma_t^2 + \left(\frac{-\bar{Q}\ell}{tA^2\Delta h}\right)^2 \sigma_A^2 +$$

$$\left(\frac{-\bar{Q}\ell}{tA(\Delta h)^2}\right)^2 \sigma_{\Delta h}^2 + \left(\frac{\bar{Q}}{tA\Delta h}\right) \sigma_{\ell}^2 \qquad 3.7$$

From Equation 3.4, this further simplifies to:

$$\left(\frac{\sigma_K}{K}\right)^2 = \left(\frac{\sigma_{\bar{Q}}}{\bar{Q}}\right)^2 + \left(\frac{\sigma_t}{t}\right)^2 + \left(\frac{\sigma_A}{A}\right)^2 + \left(\frac{\sigma_{\Delta h}}{\Delta h}\right)^2 + \left(\frac{\sigma_\ell}{\ell}\right)^2 \qquad 3.8$$

Every quantity in Equation 3.8 can be estimated. Estimates of $\sigma_{\bar{Q}}$, σ_t, σ_A, $\sigma_{\Delta h}$ and σ_ℓ are based on the accuracy with which the observer makes the measurement.

For example, during the testing of the first sample of medium sand:

$\bar{Q} \pm \sigma_{\bar{Q}} = 159 \pm 1$ ml

$t \pm \sigma_t = 1$ min $\pm$ 0.5 sec

$A \pm \sigma_A = 28.27$ cm^2 $\pm$ 1.88 cm^2

$\Delta h \pm \sigma_{\Delta h} = 25.26$ cm $\pm$ 0.05 cm

$\ell \pm \sigma_\ell = 76.3$ cm $\pm$ 0.5 cm

After calculating the value of K for the first sample from Equation 3.5, Equation 3.8 can be solved for σ_K. This procedure is repeated for each sample tested. Then, using the arithmetic mean, the averge conductivity, K is obtained from

$$\bar{K} = \frac{1}{N} \sum_{i=1}^{N} K_i \qquad 3.9$$

where N = number of samples.

The variance of this average is found by applying Equation 3.3 to Equation 3.9 to obtain:

$$\sigma_{\bar{K}}^2 = \sum_{i=1}^{N} \left(\frac{\partial \bar{K}}{\partial K_i}\right)^2 \sigma_{K_i}^2$$

If the fluid temperature is known, then the permeability, k, can be calculated from Equation 2.4 and the error in k, can be similarly computed. Knowledge of $\bar{k} \pm \sigma_{\bar{k}}$ is useful because $\bar{K} \pm \sigma_{\bar{K}}$ can then be calculated for the fluid temperature at which the experiment is run.

This analysis was applied to the constant-head tests performed on the medium and fine sand. A four-step process was followed:

1. Measure K in the laboratory.
2. Compute the error in K due to individual errors in the measurement of $\bar{Q}$, t, A, Δh, and ℓ.
3. Compute k.
4. Compute the error in k due to individual errors in the measurement of K and temperature.

Table 4 summarizes the results from the analysis. These were used to examine the range of theoretical predictions obtained as K_1 and K_2 varied within two standard deviations of their means, for a given rainfall rate of 2.7 cm/min.

Table 4. Results of the error analysis performed on K_1 and K_2 for a fluid temperature of 20° C.

	MEDIUM SAND	FINE SAND
$\bar{k}$ (m^2)	2.84×10^{-10}	1.25×10^{-11}
$\sigma_{\bar{k}}$ (m^2)	0.14×10^{-10}	0.67×10^{-11}
$\bar{K}$ (m/s)	2.75×10^{-3}	1.21×10^{-4}
$\sigma_{\bar{K}}$ (m/s)	0.25×10^{-3}	0.11×10^{-4}

Three of these solutions are shown in Figure 13. Within this range, one would be unable to distinguish between the effect of experimental error in the measurement of K_1 and K_2 and an error in the finite-element formulation of the problem.

The variations shown in Figure 13 suggested that the numerical model might need to be calibrated before its validity is evaluated. For example, suppose the mathematical model predicts the solution shown in Figure 13b, for which $K_1 = \bar{K}_1$ and $K_2 = \bar{K}_2$, while the physical model produces the flow region shown in Figure 13c, for which $K_1 = \bar{K}_1 + 2\sigma_{K_1}$ and $K_2 = \bar{K}_2 + 2\sigma_{K_2}$. The mathematical model would be verified if new predictions using $K_1 = \bar{K}_1 + 2\sigma_{K_1}$ and $K_2 = \bar{K}_2 + 2\sigma_{K_2}$ matched the experimental response to rainfall rates other than 2.7 cm/min. In this way, the mathematical model is first calibrated against the results obtained for the first in a series of rainfall rates and then verified if it is able to predict the subsequent response of the physical model.

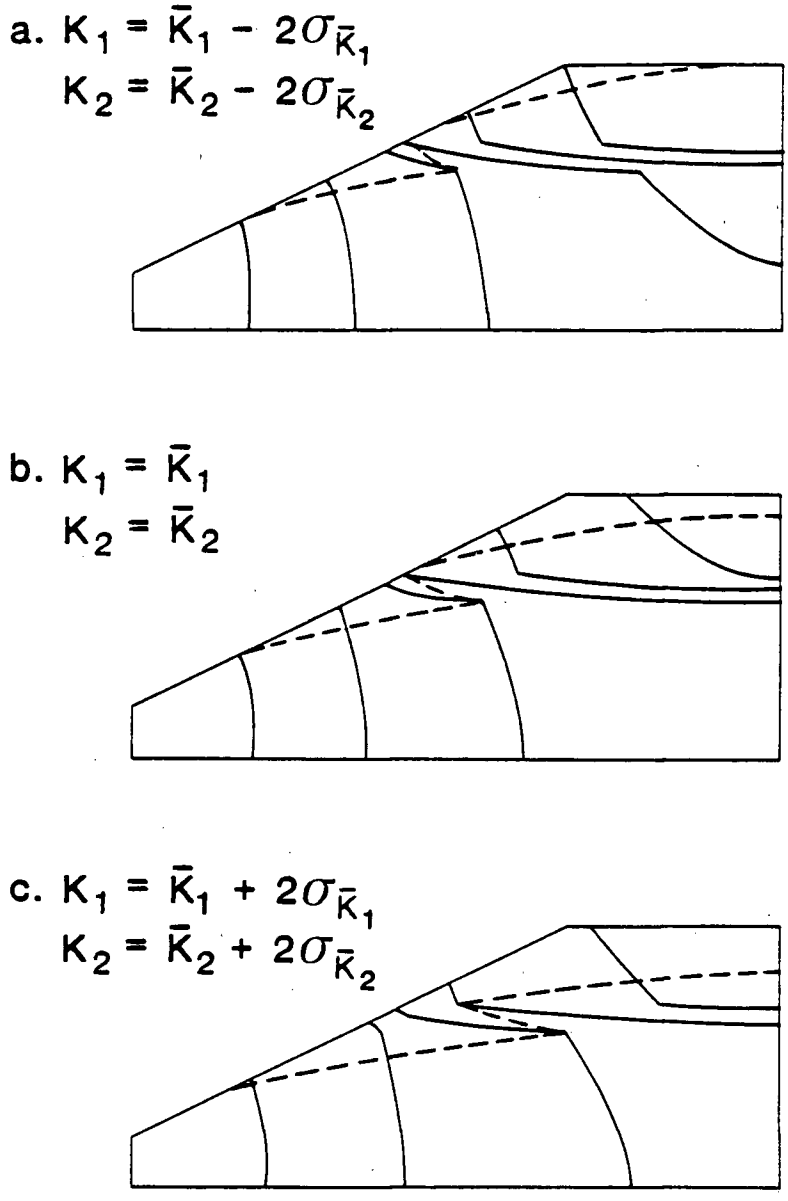

Figure 13. Range of theoretical predictions as K_1 and K_2 vary within two standard deviations of their means for a rainfall rate of 2.7 cm/min.

Superimposed on the errors in saturated conductivity are the errors present in the $K(\psi)$ and $\theta(\psi)$ data. Propagation-of-error analysis was performed on the characteristic curve data for the medium sand. The error bars associated with one standard deviation appear for one of the curves in Figures 5 and 6. Because of the relatively close fit of the data, the effect of the errors in $K(\psi)$ and $\theta(\psi)$ was judged to be less important than the effect of the errors in K_1 and K_2, although numerical studies were not performed to verify this. It was believed that an analysis of this type could be done at a later date if necessary. Subsequent results did not indicate a need for such an analysis.

The error analysis has not accounted for all the errors present in the experimental procedures. For example, because the sands were tested in a state of loosest-packing, some settlement with time was inevitable. During the $K(\psi)$ measurements, the length of the soil column decreased by up to 6 mm. This represented a 0.5% change in the total length of the soil column. The error analysis has not taken into account the transient effect of settlement on the measurement of the hydraulic properties.

GENERATION AND MAINTENANCE OF THE BOUNDARY CONDITIONS

As mentioned earlier in reference to Figure 3, the physical model contains four types of boundary conditions: impermeable boundaries, a constant-head boundary, an infiltration boundary and a seepage-face boundary. Each of these must be simulated in the laboratory. The impermeable

boundaries were formed by the plexiglass walls of the sand tank, the only precaution being that there be no leaks along the seams or tensiometer ports. The other boundary conditions required devices of varying complexity to regulate and measure inflow and outflow to the flow system.

The constant-head boundary was maintained with brass tubing connectors threaded into the wall of the tank. Outflow in excess of the amount required to maintain the constant level of water spills through the tubing connectors and the flow rate can be measured with a graduated cylinder and a stopwatch.

Rainfall was generated along the infiltration boundary using a device similar to one designed by Chow and Harbaugh (1965). The rainmaker consists of a box, 79 cm by 10 cm by 2.5 cm, constructed from 3/8-inch plexiglass. The bottom of the box contains one-inch lengths of polyethylene tubing (ID = .58 mm, OD = .965 mm) set along a one-inch square grid to produce the raindrops. Threaded into the top of the rainmaker is a tubing connector for the water supply and an air-escape valve for use when filling the rainmaker with water. The rainfall rate is controlled with a constant-discharge pump.

The most challenging boundary condition to simulate was the seepage-face boundary. A device was required that would restrain the sand and allow the measurement of seepage rates at each node along the slope, yet would not otherwise interfere with flow conditions. The device that was designed consists of nylon mesh stretched over an aluminum frame. Seepage

collectors are glued to the mesh and the entire device is bolted in place through the walls of the plexiglass tank.

The nylon mesh was selected so that the size of the mesh opening was small enough to prevent the movement of soil through it, yet large enough to offer little resistance to flow. To restrain the medium sand, which ranged in size from 0.4 mm to 0.6 mm, a mesh with an opening of 0.5 mm was chosen. To restrain the fine sand, which ranged in size from 0.075 mm to 0.10 mm, a mesh with an opening of 0.088 mm was chosen.

Seepage was collected at the nodes along the slope with the device shown in Figure 14. The collectors were constructed from PVC and glued to the mesh at the nodal point locations in such a way that only the lip of the collector is in contact with the soil. Brass tubing connectors, threaded through the wall of the tank, served to route seepage away from the slope and provide a means of measuring outflow rates.

3.2 The Trial Run

As the experimental design progressed, several questions arose regarding the technical aspects of the physical model. For example, could the sand be placed in the tank in a state of loosest packing? Would the device designed to maintain the seepage-face boundary work? Could the rainfall be maintained at constant rate for the length of time needed to reach steady state? A trial run was carried out to troubleshoot these types of problems. The objectives were to gain an indication of the likelihood of success of the physical model and to make the

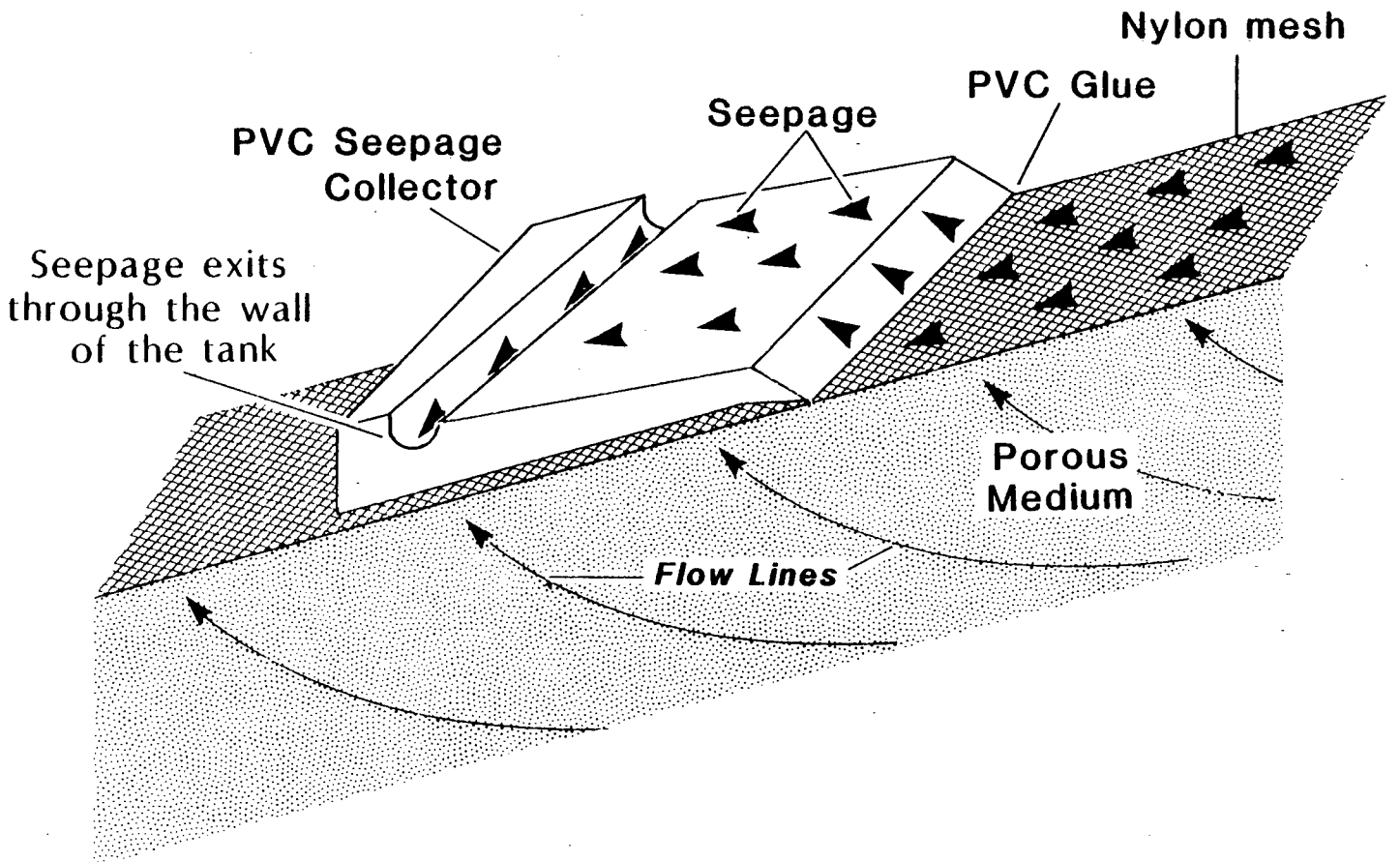

Figure 14. Seepage collector.

necessary design modifications to overcome technical problems. The final run, discussed in Section 3.3 would then incorporate the modifications and use a more extensive monitoring network to quantify the response of the physical model.

PREPARATION OF THE SAND TANK

To prepare for the trial run, the finite-element mesh was reproduced on the front wall of the tank with Letraline, a thin black adhesive tape. Fifty-six 3/8-inch diameter holes were threaded through the tank wall at the nodal points where tensiometers would be installed during the final run. For the purposes of the trial run, ten of these ports were used for tensiometers and three contained thermometers. Unused ports were sealed with brass plugs. Figure 15 shows the finite-element mesh, the function of each port, and the numbering system used to identify the tensiometers. A central support mounted on the frame of the tank prevented placement of tensiometers along $x = 1.2$ m.

The slope device was lowered into the tank and bolted in place. Twelve, 3/8-inch diameter holes were threaded into the tank to route seepage away from the seepage-face nodes. The location of the seepage collectors and the numbering system used to identify the collectors are indicated in Figure 15. Due to an oversight by the author, a collector was not placed at the lowermost seepage-face node.

Prior to filling the tank with water, all ports were sealed. Clamped tubing was attached to tubing connectors along the seepage-face and constant-head boundaries. The

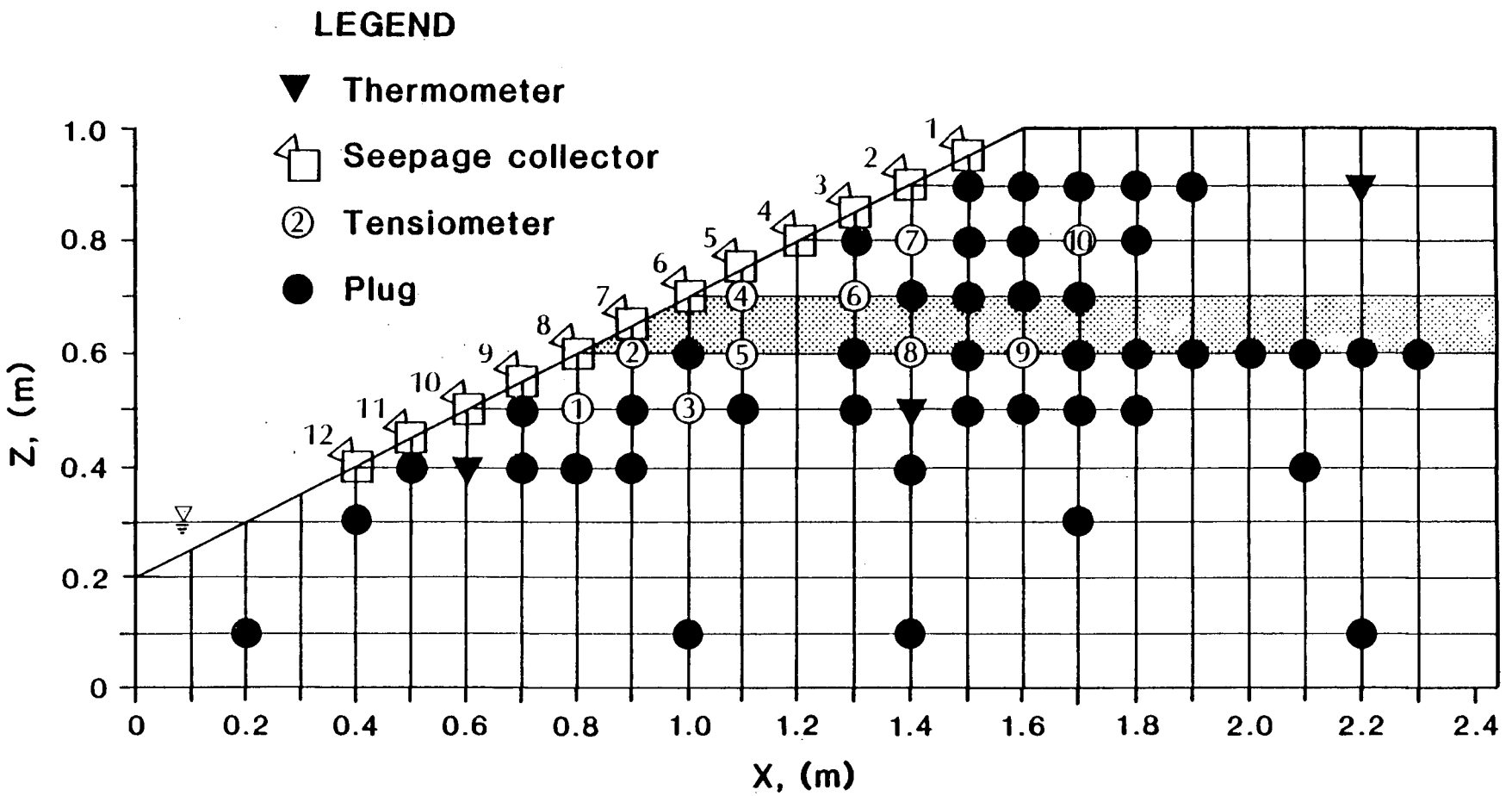

Figure 15. Location and function of measurement ports with respect to the finite-element mesh.

tensiometers and thermometers were installed by the method shown in Figure 4. The tank was then filled with tap water to a level z = 1.1 m; bleach was added to prevent algal growth. The manometers were purged of air and allowed to equilibrate.

FILLING THE TANK WITH SAND

Two methods of placing the sand in the tank were tried. First, wet sand was added to the water in the tank and allowed to settle into place in a state of loosest packing. This method failed because the sand would not settle flush against the nylon mesh along the slope. Attempts to gently push the sand in place along the slope were awkward and created differential packing.

The second method was to add wet sand to the water in the tank and distribute it with water pumped through a long metal rod. The pump intake was placed in the water to the left of the slope device. The pump outflow tubing was attached to a submerged rod and the sand could then be blown into place by the jet of water. In this way, the sand was placed flush against the nylon mesh. The only disadvantage to the method was that the bulk density of the sand in the tank was now different than the bulk density of the samples used to determine the hydraulic properties. The consequence of this will be discussed when the results are presented.

After the flow region had been placed in the tank, a thin layer of pea-sized gravel was placed along the infiltration boundary so that holes would not be bored into the sand by the rain.

RESULTS OF THE TRIAL RUN

To begin the trial run, the clamps sealing the constant-head boundary were removed and the water drained slowly from the tank. Rain was simultaneously applied at a rate of 2.7 cm/min. Approximately two hours were allowed to ensure that steady-state conditions were established. Readings of the pressure-head distribution were recorded for three successively decreasing rainfall rates. The thermometers indicated that the fluid temperature remained constant, within a degree Celsius, throughout the run.

The predicted pressure-head distribution for three rainfall rates is shown in Figure 16. Because the bulk density of the sand in the tank was higher than that of the samples used to determine the hydraulic properties, the values of K_1 and K_2 in the tank were lower than those used in the predictions shown in Figure 16. This can be seen by comparing the predicted and measured pressure-head distribution, as shown in Figure 17. The line connecting the data points are added to aid the comparison of the data; they do not represent interpolated values nor any other type of physical relationship. Note that for a given rainfall rate, the measured ψ values lie to the right of and are therefore greater than the predicted values. Subsequent numerical studies showed that by slightly decreasing the values of K_1 and K_2, the predicted values in Figure 17 shift to the right to provide better agreement with the experimental results. Qualitatively, however, the results are good. In particular, the measured ψ

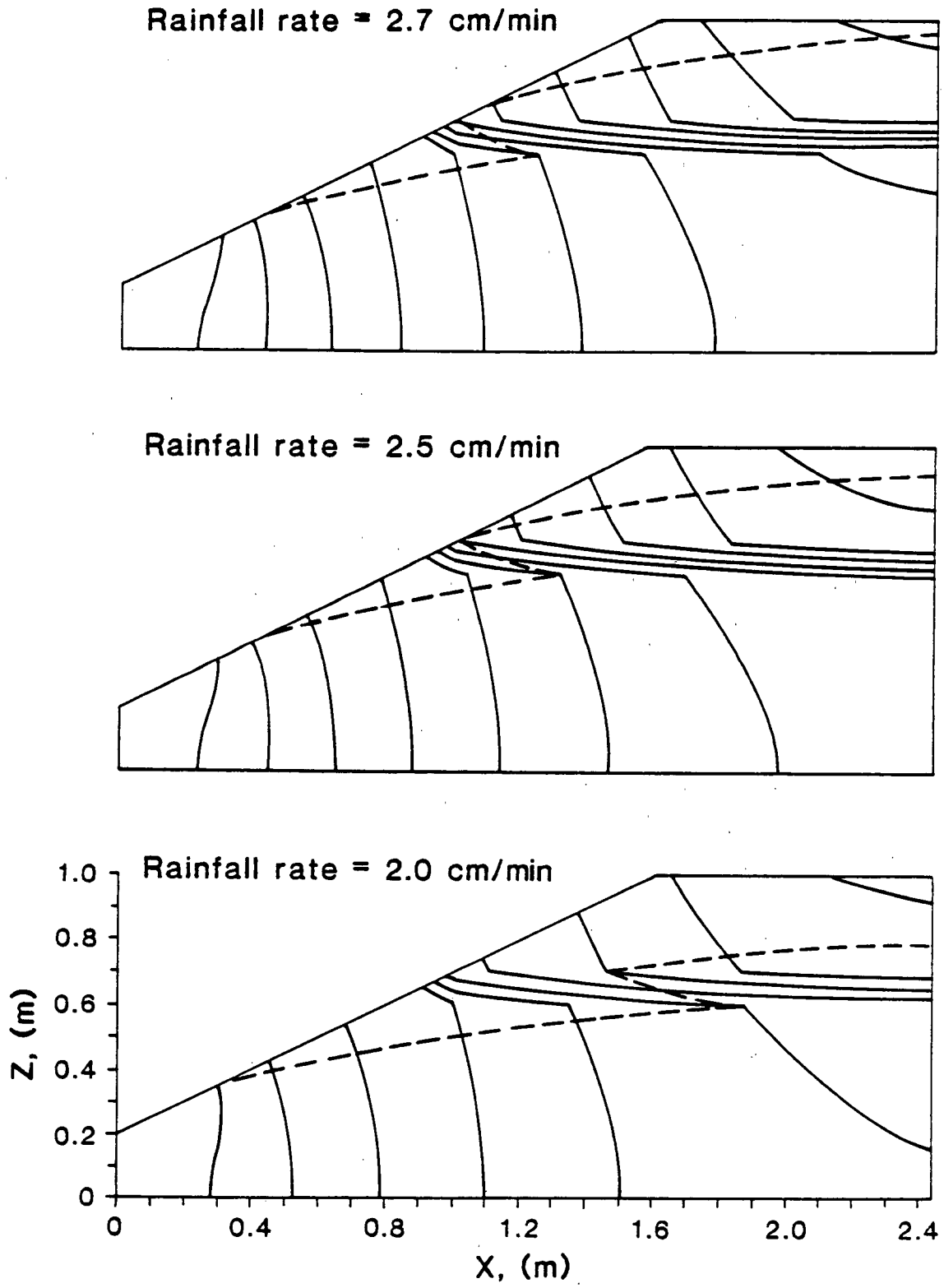

Figure 16. Predicted results for the trial run; K_1 = 2.75 x 10^{-3} m/s and K_2 = 1.21 x 10^{-4} m/s.

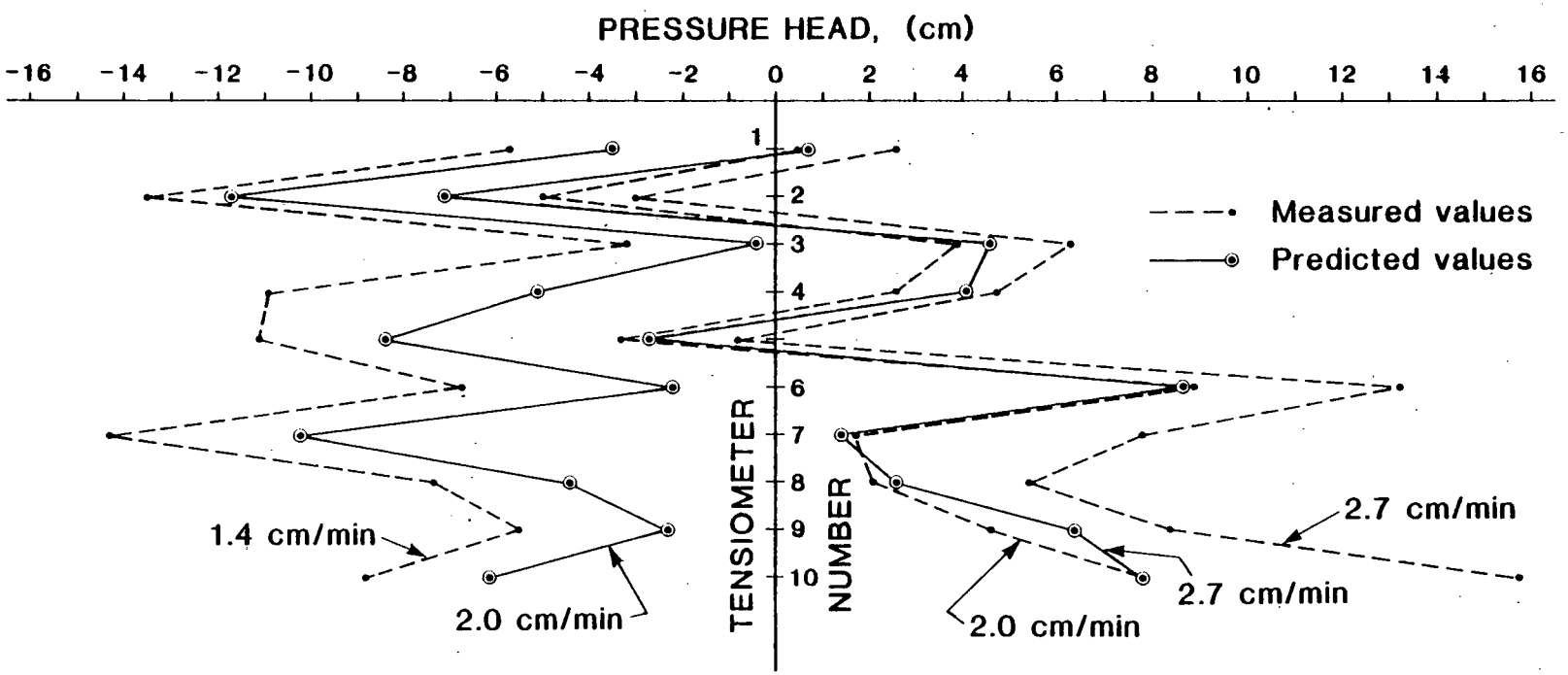

Figure 17. Comparison of measured and predicted pressure-head readings during the trial run.

values show that an unsaturated wedge formed beneath the impeding layer and became more extensive as the rainfall rate decreased.

The observed seepage-face locations did not correspond well with the predicted results. For example, for a rainfall rate of 2.7 cm/min, outflow was measured at seepage collector (SC) #4, #6, #7 and #12 while the theoretical model predicted seepage from SC #6 and #12. This discrepancy occurred because in the two days between filling the tank with sand and beginning the trial run, the sand had settled approximately 5mm away from the nylon mesh along the slope. Consequently, when the water level was lowered at the beginning of the trial run, slumping occurred. This affected the location of the seepage faces in two ways. First, it displaced the position of the fine layer downslope, near the nylon mesh. The uppermost seepage face was therefore shifted slightly downslope as indicated by the outflow measured at SC #7. Second, while the slumping provided excellent contact between the seepage collectors and the sand for SC #4 through SC #12, much of the sand near the top of the slope had moved downslope, leaving no contact at all above SC #4. The distance from the nylon mesh to the sand increased from a few millimeters at SC #3 to several centimeters at SC #1. Therefore, when ponding occurred along the infiltration boundary for a rainfall rate of 2.7 cm/min, the runoff flowed along the slope face and was collected in SC #4. Ponding, as well as outflow at SC #4, ceased for lower rainfall rates. To eliminate the problems

caused by slumping, it was recognized that the sand in the final run would need to be compacted as it is placed in the tank.

The rainfall rate was calculated from calibrations made prior to the trial run. Dust and lint became entrained in the water and eventually clogged up to fifty percent of the capillary tubes producing raindrops. This indicated the need for a filter around the pump intake for the final run and suggested that the rainfall rate is best calculated from the total outflow rate at steady state.

3.3 The Final Run

The final run was monitored with fifty-six tensiometers. Ten were attached to manometers and the remainder were connected by 1/16-inch ID nylon tubing to a 48-port Scanivalve. The Scanivalve is an electronic scanning valve that allows the hydraulic head to be measured at each port with a single pressure transducer. The output was read with a digital voltmeter and recorded by hand. Two of the 48 ports were used throughout the final run to calibrate the transducer. The error associated with the hydraulic head readings was approximately $\pm$ 3mm of water. This corresponds to a 1 mm error in the measurement of the pressure head and a 2 mm error in the measurement of the elevation head.

The sand was placed in the tank, as before, and compacted by striking the walls of the tank with a rubber mallet. Despite the compaction, the sand settled overnight up to 2 mm

away from the nylon mesh. As the water level was lowered, some slumping occurred and the fine layer was displaced slightly downslope in the vicinity of the nylon mesh. Additional coarse sand was fed from the top of the slope resulting in good contact between the flow region and all seepage collectors.

Steady-state readings were recorded for rainfall rates of 1.8 cm/min, 1.5 cm/min, and 1.26 cm/min. An attempt was made to take readings for a lower rainfall rate, but after four hours, the values were still fluctuating and the experiment was terminated. The rainfall rate was calculated from the total outflow rate at steady state. Figure 18 is a photograph of the experimental setup.

The experimental results are shown in Figure 19. The mathematical model was calibrated against the results shown in Figure 19a in the following manner. Because of the uncertainty concerning the in situ values of K_1 and K_2, a falling-head permeameter test was performed on a highly compacted sample of the medium sand. The resulting K_1 value served as a lower limit for the possible in situ value of K_1. A similar test on the fine sand was not made because all of the available fine sand had been placed in the sand tank. Calculations were then performed to determine if a reasonable set of K_1 and K_2 values could be found that would predict the observed response of the physical model. The results of this back-calculation are summarized in Table 5. Note that all values correspond to a fluid temperature of 11.5°C, the temperature at which the experiment was run.

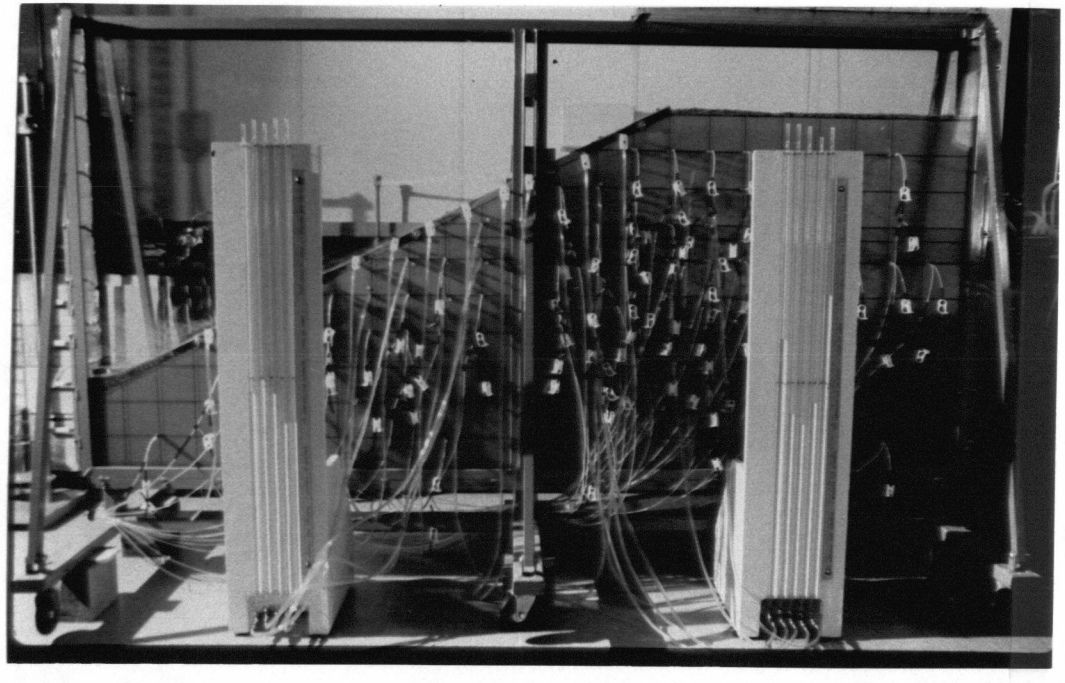

Figure 18. Photograph of the final experimental run.

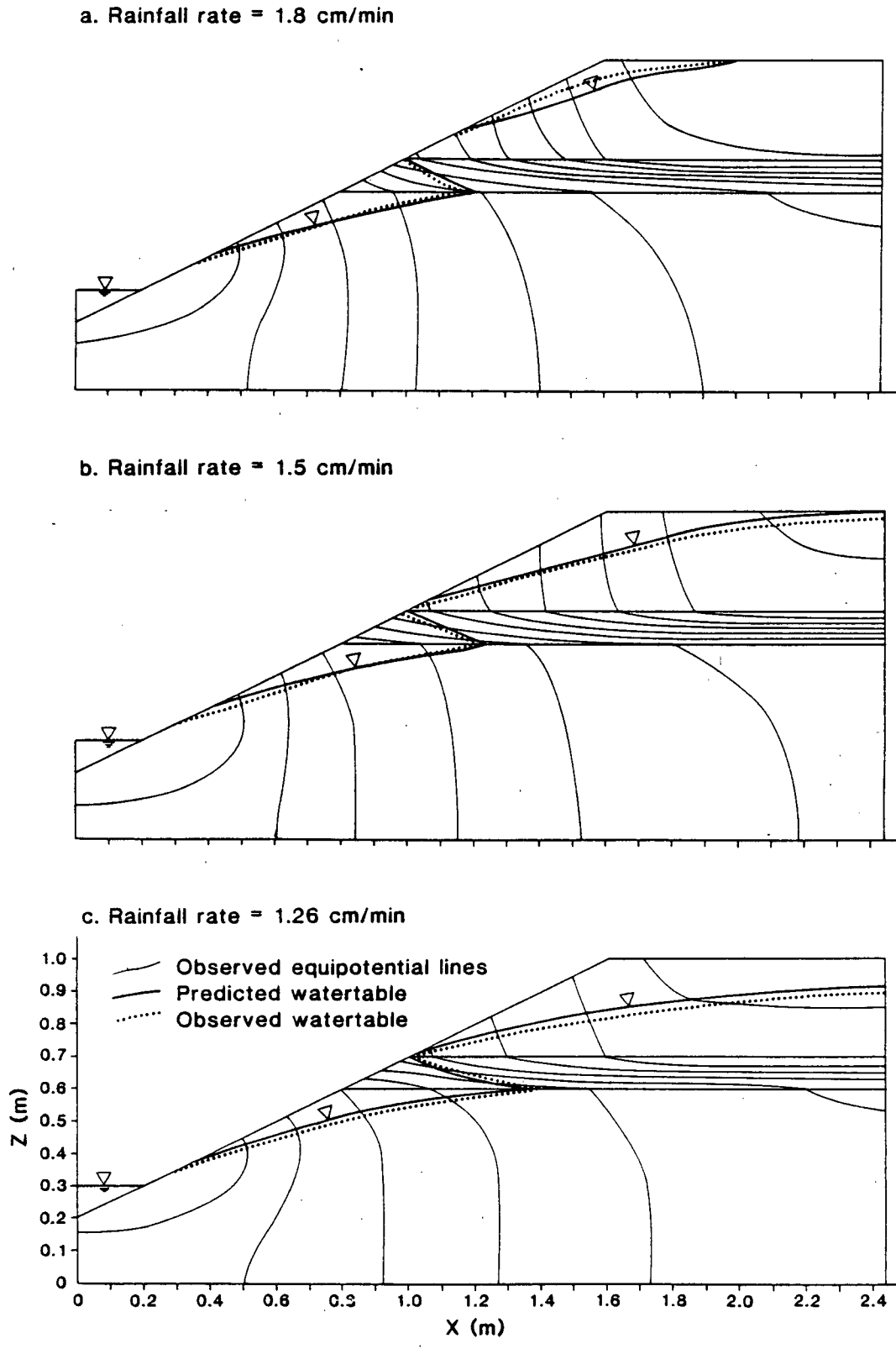

Figure 19. Comparison of predicted and observed water-table configurations for the final run, using best-fit values of K_1 and K_2.

Table 5. Summary of back calculations.

	K_1 (m/s)	K_2 (m/s)
loosest packing, 11.5°C	2.2×10^{-3}	9.8×10^{-5}
densest packing, 11.5°C	6.6×10^{-4}	not measured
best-fit value by model calibration	1.4×10^{-3}	5.5×10^{-5}

The best-fit values for K_1 and K_2 represent a 36% and 44% decrease, respectively, from the K values in a state of loosest packing. No attempt was made to measure new characteristic curves to account for changes in their shape due to compaction. The curves were simply scaled to the newly calculated values of the saturated conductivity. Based on the best-fit values of K_1 and K_2, the response of the physical model to the two subsequent rainfall rates was predicted. A comparison of the predicted and observed water-table configurations for all three rainfall rates are shown in Figure 19. Appendix B contains a comparison of the predicted and measured hydraulic-head data, as well as the corresponding pressure-head and elevation-head data.

Table 6 summarizes the predicted and measured values of outflow for the three rainfall rates. Note that seepage was collected at SC #7, but was not predicted, in all cases, due to the slight displacement of the fine sand layer near the slope.

In all cases, the total predicted outflow rates were within 11% of the total measured outflow rates. The first run shows a large discrepancy between the predicted and measured outflow rates from the uppermost seepage face (SC #5, 6, 7)

Table 6. Predicted versus observed outflow rates.

Run #1: Rainfall rate = 1.80 cm/min

Seepage Collector #	Predicted outflow rate (cm^3/min)	Measured Outflow rate (cm^3/min)
12	42	0
7	0	44
6	55	200
5	99	74

total predicted outflow = 1330 cm^3/min

total measured outflow = 1426 cm^3/min

Run #2: Rainfall rate = 1.50 cm/min

Seepage Collector #	Predicted outflow rate (cm^3/min)	Measured Outflow rate (cm^3/min)
12	32	0
7	0	34
6	52	72
5	65	0

total predicted outflow = 1270 cm^3/min

total measured outflow = 1133 cm^3/min

Run #3: Rainfall rate = 1.26 cm/min

Seepage Collector #	Predicted outflow rate (cm^3/min)	Measured Outflow rate (cm^3/min)
7	0	13
6	25	16

total predicted outflow = 1095 cm^3/min

total measured outflow = 996 cm^3/min

relative to the other runs. This may be due to ponding that occurred over much of the infiltration surface for a rainfall rate of 1.8 cm/min. At steady state, there was a constant depth of water on the surface. The maximum depth was approximately 1 cm at the the right hand side of the surface and tapered off to zero depth before reaching the slope. This created a head of water that was not predicted in the theoretical model. Recall that when the infiltration surface ponds during the numerical simulation, ψ is set equal to zero and the excess runoff is disregarded; it is not routed away nor is it converted into an equivalent head of water. The material used in the physical model is quite porous and conductive, so that a 0-1 cm constant head of water along the infiltration boundary can cause a large increase in the flow rate through the region, as observed. Given that the hydraulic head readings were accurate to within $\pm$ 3 mm, the effect on the head distribution of a 0-1 cm head of water along the infiltration boundary is not likely to be significant.

The rainfall rate during Run #2 was adjusted so that there was no ponding at steady state. The total outflow rate and the outflow rates from the uppermost seepage face compare well with the predicted rates. Note, however, that during both Run #1 and Run #2, seepage was predicted but not observed at SC #12. The slope of the water table immediately above the lowermost seepage face is relatively steep. A small discrepancy in the position of the water table can therefore translate into a larger discrepancy in the length of the lowermost seepage face.

For Run #3, the outflow rates measured along the slope compare well with theoretical predictions.

It is important to note that during the final run, the sand did not desaturate; that is, in the unsaturated zone, the pressure head remained greater than the air-entry value of the medium sand. The reason for this is as follows. Recall that the medium sand desaturates for $\psi < 11.5$ cm, yet the lowest value of ψ that can be read by the tensiometer is $\psi = -18$ cm. Therefore, only a very narrow range of values corresponding to desaturated conditions could be detected, namely, $-18 \text{ cm} < \psi < 11.5$ cm. The experiment was purposely designed to demonstrate the development of multiple seepage faces for relatively wet condition. As it turned out, the pressure head remained greater than -9 cm and the medium sand did not desaturate. While the experimental constraints precluded a rigorous test of the ability of the finite-element model to simulate flow in the desaturated portion of the unsaturated zone, the ability of the model to predict the water-table configuration and seepage-face locations has been verified.

In conclusion, the experimental results confirm that the numerical model produces solutions that are physically correct. The most plausible explanation for the minor numerical discrepancies that appear in Figure 19, Table 6, and Appendix B is that the experimental conditions were not perfectly matched in the numerical runs. The numerical model was set up assuming that each sand layer is homogeneous and isotropic, when in fact, it is probable that they are not. The conductivity could

easily vary by a factor of two over a very short distance due to nonuniform compaction. This type of variation results in discrepancies between predicted and measured outflow rates and head values. However, in light of the other aspects upon which the verification is judged, these facts do not seem to seriously discredit either the numerical or the physical model.

Chapter 4

STEADY-STATE SENSITIVITY ANALYSIS

Once the numerical model was verified, a steady-state analysis was performed to investigate the sensitivity of the solution to: a) the location and number of impeding layers within a hillside, b) the magnitude of the hydraulic conductivity contrast between adjacent geologic units, and c) the rainfall rate. Less-detailed studies were performed to indicate the sensitivity of the solution to anisotropy and the slope angle. Only a small portion of the range of hydrogeologic conditions has been investigated; however, the cases chosen illustrate that the fluid-pressure distribution and the development of multiple seepage faces are strongly dependent upon the position of the layers and their hydraulic properties.

4.1 Methodology

The finite-element mesh used throughout much of the analysis is shown in Figure 20. The flow region is 350 m long, 195 m high, and is bounded by a relatively steep slope of approximately 40°.

There are six possible locations for impeding layers, labeled A through F in Figure 20. Two types of material were specified for each flow region constructed with this mesh. Material No. 1 represents the dominant soil type and has a saturated hydraulic conductivity denoted by K_1. Material No. 2

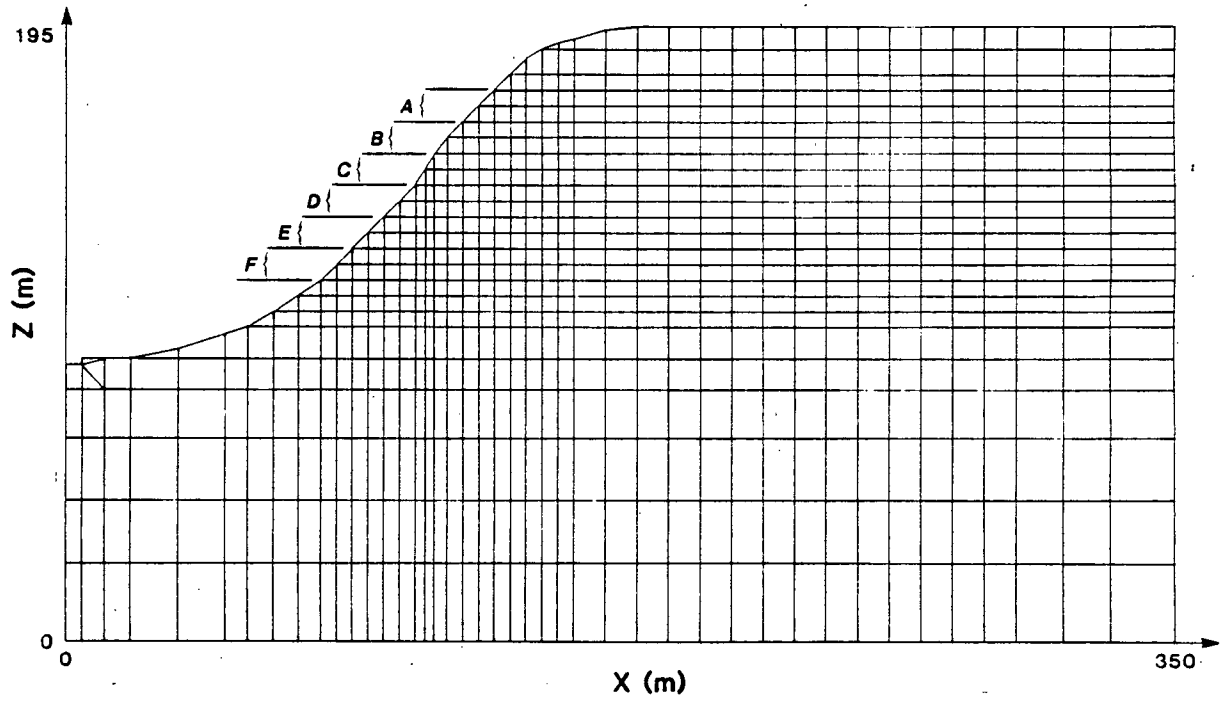

Figure 20. Finite-element mesh used for the steady-state sensitivity analysis.

represents the less abundant soil type and has a saturated hydraulic conductivity denoted by K_2. Therefore, a flow region identified as MeshAE indicates that there are two layers of Material No. 2 located at positions A and E in Figure 20. The remainder of the flow region is composed of Material No. 1. Similarly, examples of one- and three-layer flow systems include regions identified as MeshD and MeshACE. Note that the number of layers refers to the number of K_2 layers assigned to the hillside. In all cases, $K_1 > K_2$, and the layers of Material No. 2 will be referred to as "impeding layers".

The characteristic curves corresponding to Material No. 1 and Material No. 2 are derived from those representing Pachapa Fine Sandy Clay and Yolo Light Clay, respectively. These curves are shown in Figure 21. Data for both soils were obtained from Mualem (1976) and were originally reported by Gardner (1959) and Moore (1939). The finite-element program requires the information in the form of tables of θ vs ψ and θ vs K_r where K_r is the relative hydraulic conductivity, defined as:

$$K_r = \frac{K(\psi)}{K_s} \qquad 4.1$$

and K_s is the saturated hydraulic conductivity of the soil. Throughout the sensitivity analysis, the tables of θ vs ψ and θ vs K_r have remained unchanged; they have been derived from the curves shown in Figure 21. Therefore, if the value of K_s is changed the $\theta(\psi)$ curve is not modified and the $K(\psi)$ curve is

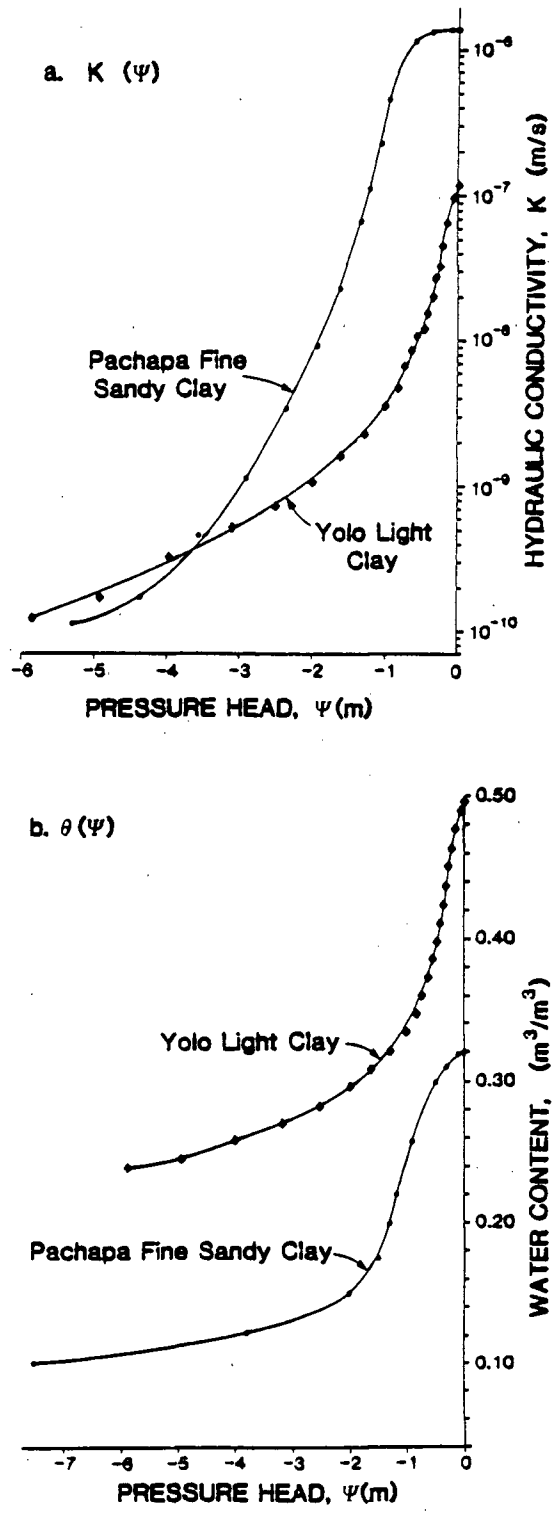

Figure 21. Characteristic curves used in the steady-state sensitivity analysis.

automatically scaled in accordance with Equation 4.1. It should be emphasized that natural soils do not exhibit these idealized properties; $\theta(\psi)$ curves are not independent of the value of K_s nor are $K(\psi)$ curves related by the simple scaling implied in Equation 4.2. However, these assumptions have been made to simplify the numerical procedure. In general, the saturated-unsaturated flow systems are far more sensitive to the relative values of K_s than to the precise nature of the characteristic curves (Stephenson and Freeze, 1974). For the generic modeling effort presented here, the approach embodied in Equation 4.1 is justified.

The generalized boundary-value problem solved in the steady-state analysis is shown in Figure 22a. Note that the rainfall rate applied to the infiltration boundary represents an average annual rate. In reality, annual precipitation patterns form a time series such as the one shown in Figure 22b. Consequently, the water table may fluctuate during the course of the year, as indicated schematically in Figure 22c. It is assumed that by replacing the time series with an average annual rainfall rate, the steady-state solution will approximate the mean annual position of the water table. The rainfall rates used in the steady-state sensitivity analysis will therefore appear to be perhaps an order of magnitude lower than those observed for individual storms. For example, a steady state rainfall of 10^{-7} m/s represents a region that annually receives 3 m of precipitation, while the rainfall rate

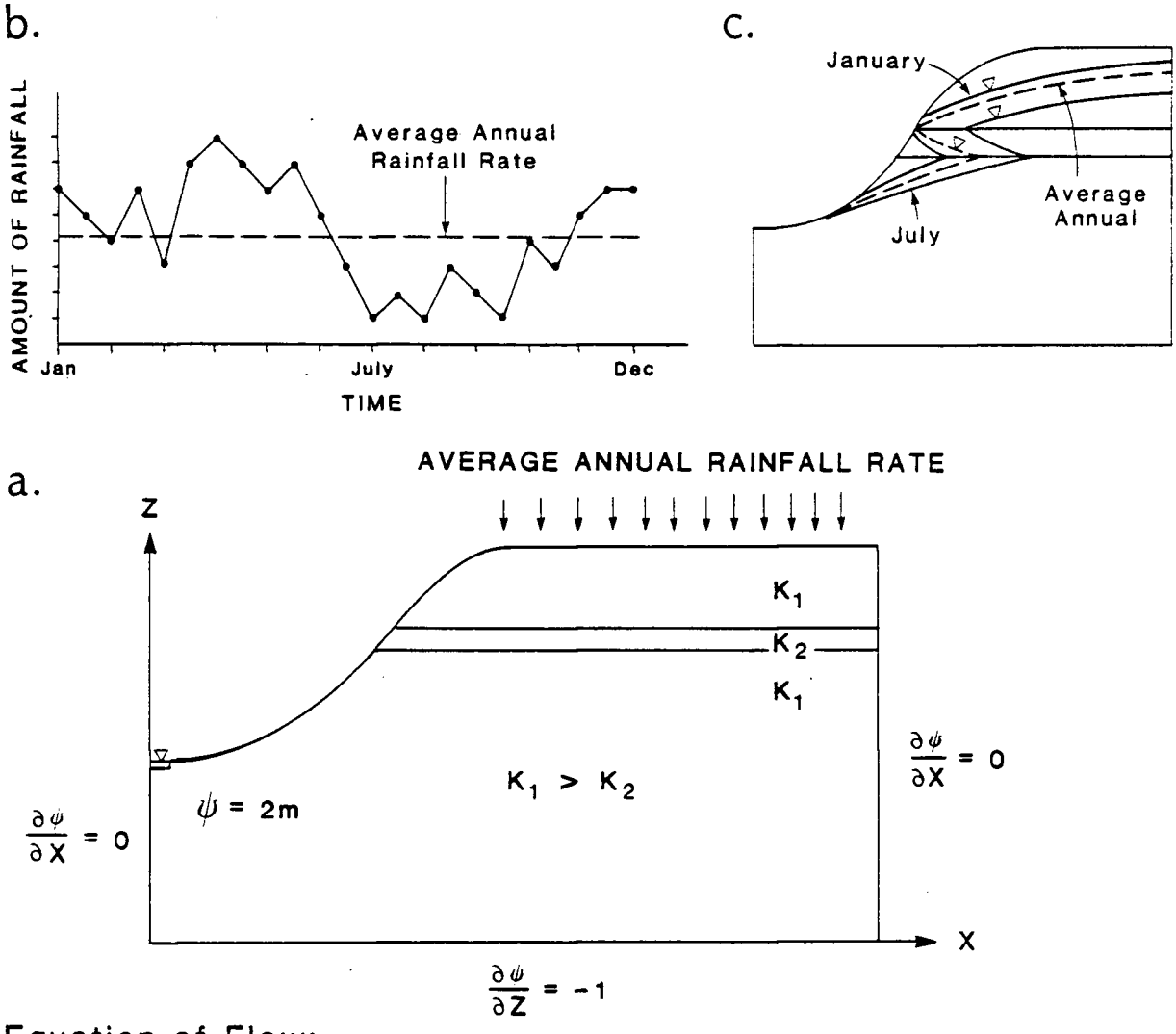

Equation of Flow:

$$\frac{\partial}{\partial x}\left[K(x,z,\psi)\ \frac{\partial \psi}{\partial x}\right] + \frac{\partial}{\partial z}\left[K(x,z,\psi)\left(\frac{\partial \psi}{\partial z} + 1\right)\right] = 0$$

Figure 22. Generalized boundary-value problem solved in the steady state sensitivity analysis.

during an individual storm in that same region may be on the order of 10^{-6} m/s (3.6 mm/hr).

4.2 Results

The results of the sensitivity study are presented in terms of a) the nature of the fluid-pressure distribution, as characterized by the extent of the unsaturated wedge, and b) the percentage of the total outflow passing through each of the seepage faces. Conclusions are drawn from graphs summarizing the results of many simulations in which the layering sequence, the rainfall rate, and the hydraulic conductivity contrast, K_1/K_2, have been varied. It should be noted that throughout the analysis, the effect of increasing K_1/K_2 has been studied by leaving the value of K_1 unchanged and decreasing the value of K_2. The same conclusions apply if K_2 is fixed and K_1 is increased, although individual solutions differ slightly depending upon the way in which K_1/K_2 is increased.

ONE-LAYER FLOW SYSTEMS

Six flow regions were used to investigate the development of multiple seepage faces in one-layer systems, each containing a 10 m thick layer of Material No. 2 at one of the six locations indicated in Figure 20. Hydraulic conductivity contrasts of 20 and 25 were studied initially; K_1 was maintained at 1.4×10^{-6} m/s in both cases. The range of rainfall rates was varied between relatively high values for which the region was transmitting water at a maximum rate, and relatively low values for which numerical instability occurred

due to the development of steep ψ- and K-gradients in the unsaturated zone. These numerical limitations are discussed in more detail later in this chapter.

Figure 23 summarizes the effect of the position of the impeding layer and the hydraulic conductivity contrast on the extent of the unsaturated wedge. Note that for Mesh A, the unsaturated wedge extends the entire length of the hillside for all rainfall rates and a seepage face has not formed above the impeding layer. Two conclusions can be drawn from Figure 23. First, for a given K_1/K_2, an increase in the elevation of the impeding layer increases the extent of the unsaturated wedge. Second, for a given elevation of the impeding layer, an increase in K_1/K_2 increases the extent of the unsaturated wedge. These conclusions are illustrated by the hydraulic-head distributions and water-table configurations shown in Figure 24 for Mesh E and Mesh B.

Figure 25 summarizes the effect of the position of the impeding layer and the hydraulic conductivity contrast on the percentage of the total outflow discharged across the uppermost seepage face. For a given K_1/K_2, an increase in the elevation of the impeding layer decreases the percentage of the total outflow across the uppermost seepage face. For a given elevation of the impeding layer, an increase in K_1/K_2 increases the percentage of the total outflow across the uppermost seepage face. Correspondingly, the length of the uppermost seepage face increases with a decrease in elevation and an increase in K_1/K_2, as shown in Figure 26.

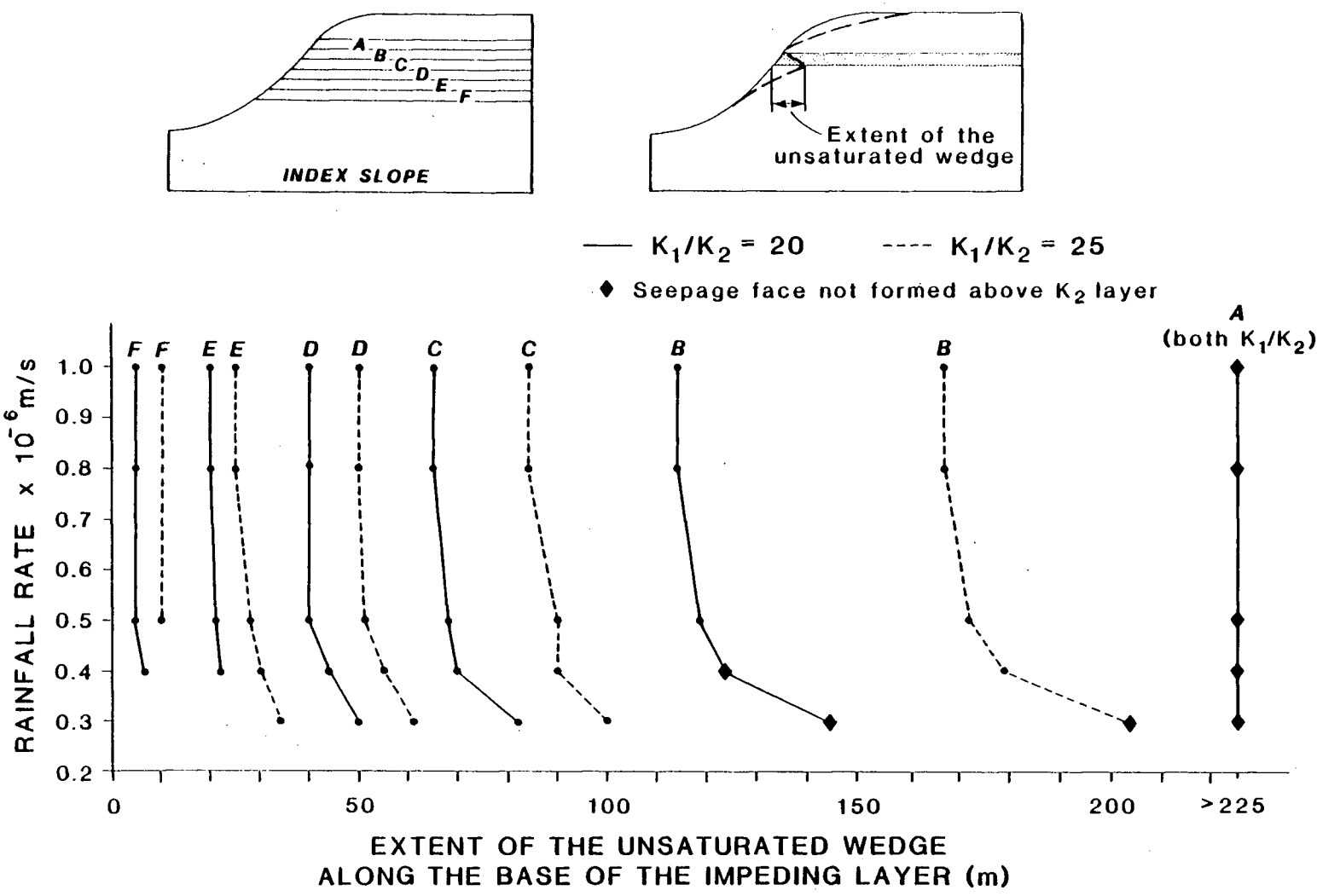

Figure 23. Sensitivity of the unsaturated wedge to the position of the impeding layer and to the hydraulic conductivity contrast.

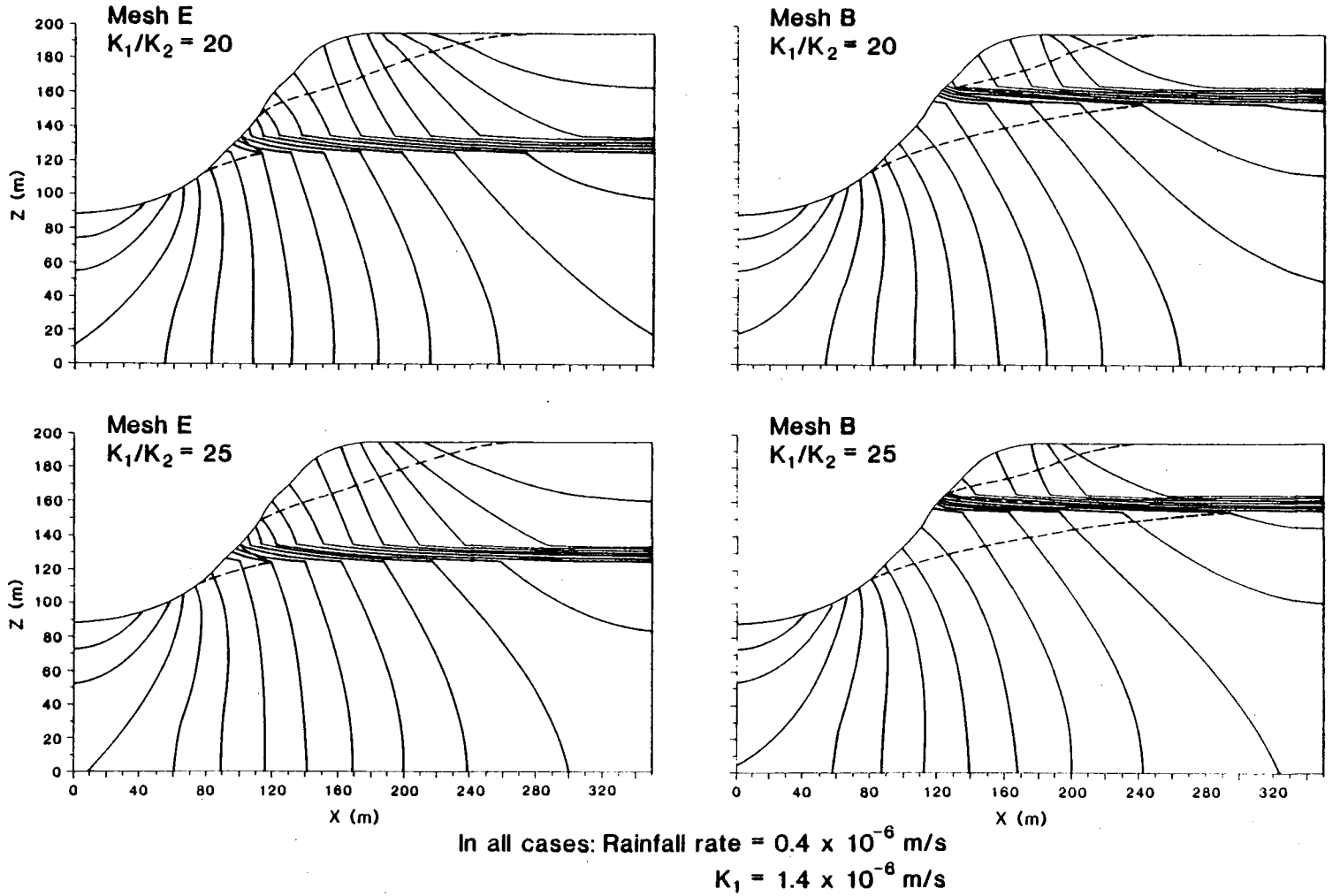

Figure 24. Flow regions exemplifying the effect of the position of the impeding layer and the hydraulic conductivity contrast on the extent of the unsaturated wedge.

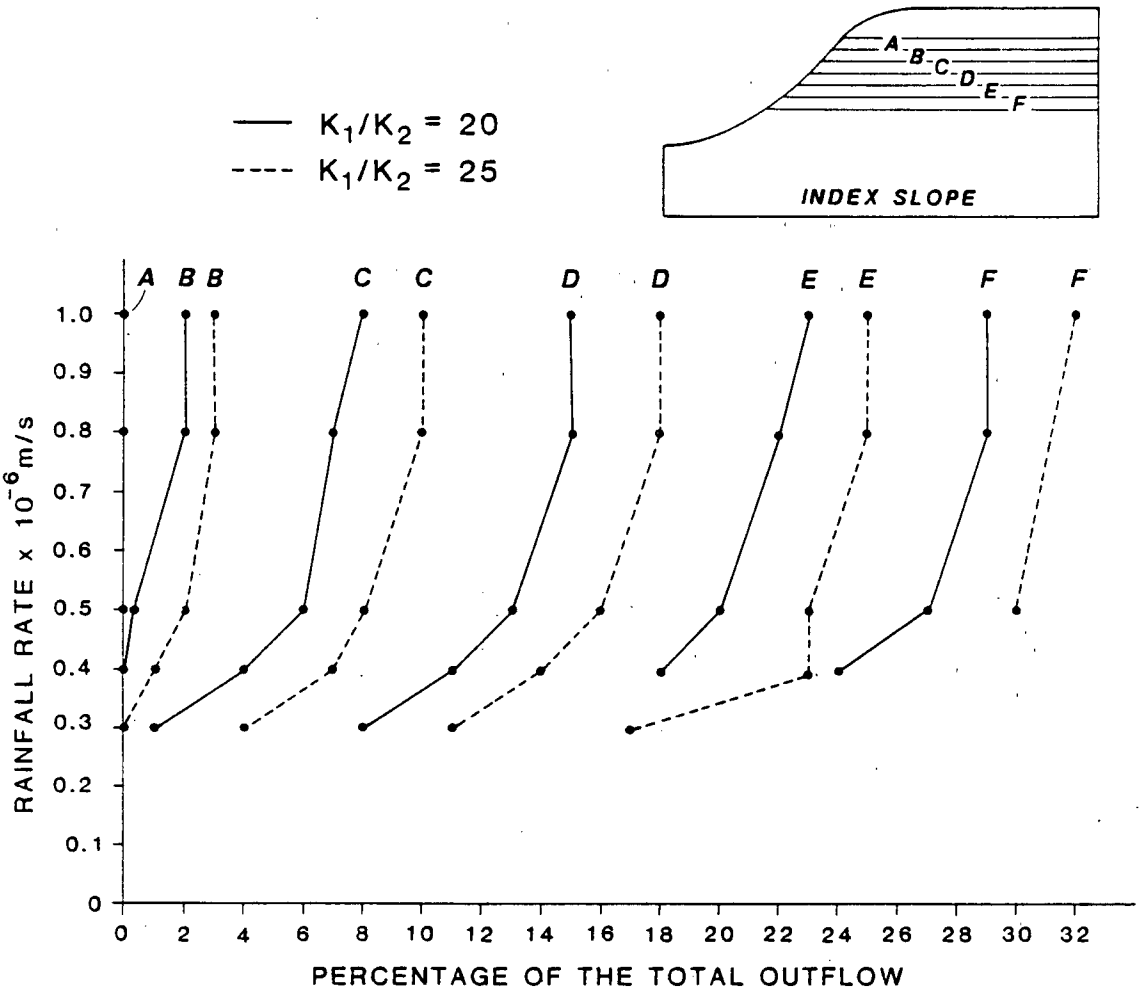

Figure 25. Sensitivity of the outflow to the position of the impeding layer and to the hydraulic conductivity contrast.

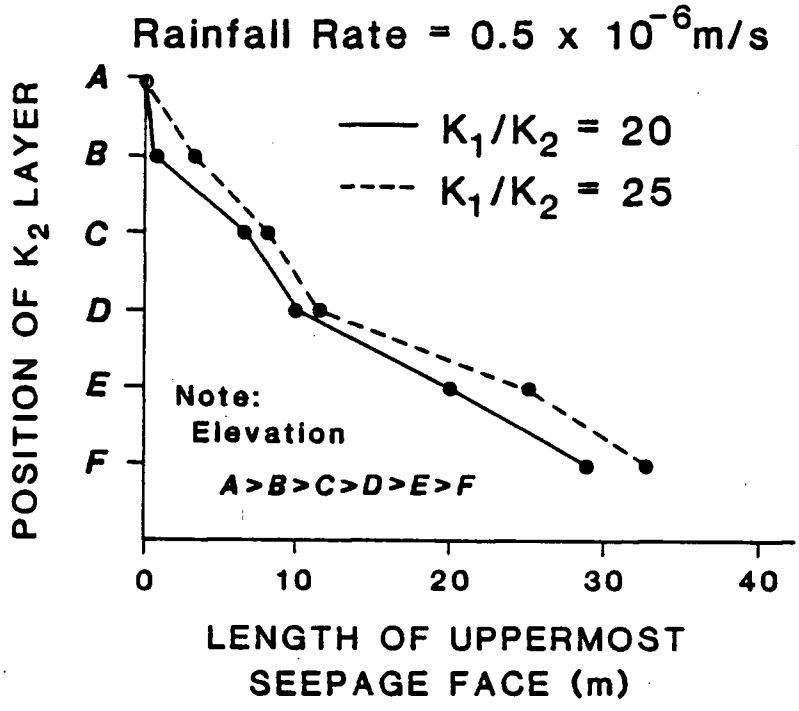

Figure 26. The length of the uppermost seepage face as a function of the position of the impeding layer and the hydraulic conductivity contrast.

The extent of the unsaturated wedge and the percentage of the total ouflow across the uppermost seepage face has been shown to be sensitive to hydraulic conductivity contrasts that differ by less than half an order of magnitude. Natural deposits, however, may have hydraulic conductivities which vary over many orders of magnitude. Mesh C was selected to investigate the solution as K_1/K_2 is increased over four orders of magnitude. To do this, the flow region was extended to x = 3350 m and the extent of the unsaturated wedge was measured for K_1/K_2 = 10, 100, 1000, 2500, 5000 and 10,000. In each case, $K_1 = 10^{-7}$m/s and the rainfall rate was $4x10^{-8}$m/s. The results are shown in Figure 27. For $K_1/K_2 > 5000$, the wedge extends the entire length of the hillside and the saturated zone above the impeding layer is completely perched.

TWO-LAYER FLOW SYSTEMS

The development of multiple seepage faces in two-layer systems was studied with ten layering sequences, distinguished on the basis of the distance separating the impeding layers, as outlined in Table 7. The seepage face formed above the upper

Table 7. Classification of two-layer systems.

Distance separating the impeding layers (m)	Mesh Name
10	AC, BD, CE, DF
20	AD, BE, CF
30	AE, BF
40	AF

impeding layer will be called the upper seepage face; the seepage face associated with the lower impeding layer will be

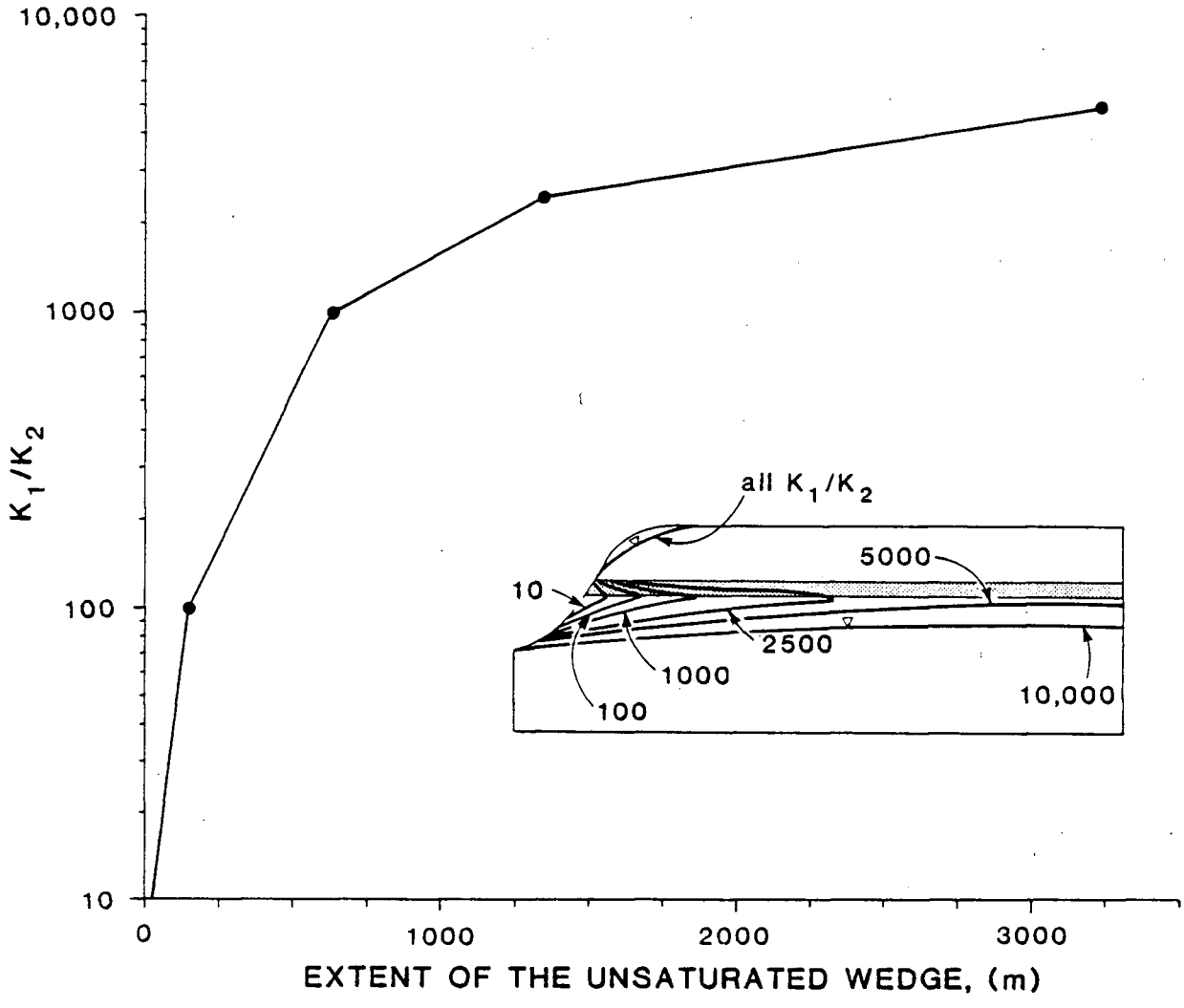

Figure 27. The extent of the unsaturated wedge as the hydraulic conductivity contrast increases over several orders of magnitude for $K_1 = 10^{-7}$ m/s and a rainfall rate of 4×10^{-8} m/s.

called the middle seepage face; and, the seepage face which forms at the base of the hillside will be called the basal seepage face.

For a given distance separating the impeding layers, the conclusions concerning the fluid-pressure distribution are the same as those made for one-layer systems. If the hydraulic conductivity contrast is constant, then an increase in the elevation of the impeding layers increases the extent of both unsaturated wedges; if the elevation of the layers is constant, then an increase in K_1/K_2 increases the extent of the wedges. These conclusions are exemplified by the flow regions shown in Figure 28 for the case in which the distance separating the impeding layers is 10 m. The conclusions also hold for 20, 30, and 40 m of separation.

The relative extent of the unsaturated wedges depends upon the distance separating the impeding layers. In Figure 29, the extent of both wedges is plotted for Meshes AC, AD, AE, and AF, corresponding to 10, 20, 30, and 40 m of separation, respectively. In all cases, the extent of the lower wedge is less than that of the upper wedge, except for 10 m of separation. The hydraulic-head distributions and water-table configurations in Figure 30 illustrate this for Meshes BD, BE, and BF.

The percentages of the total outflow discharged across the upper and middle seepage faces, %Qu and %Qm, are summarized in Figure 31 for K_1/K_2=20. A comparison of the results down each column shows that if the position of the upper impeding layer

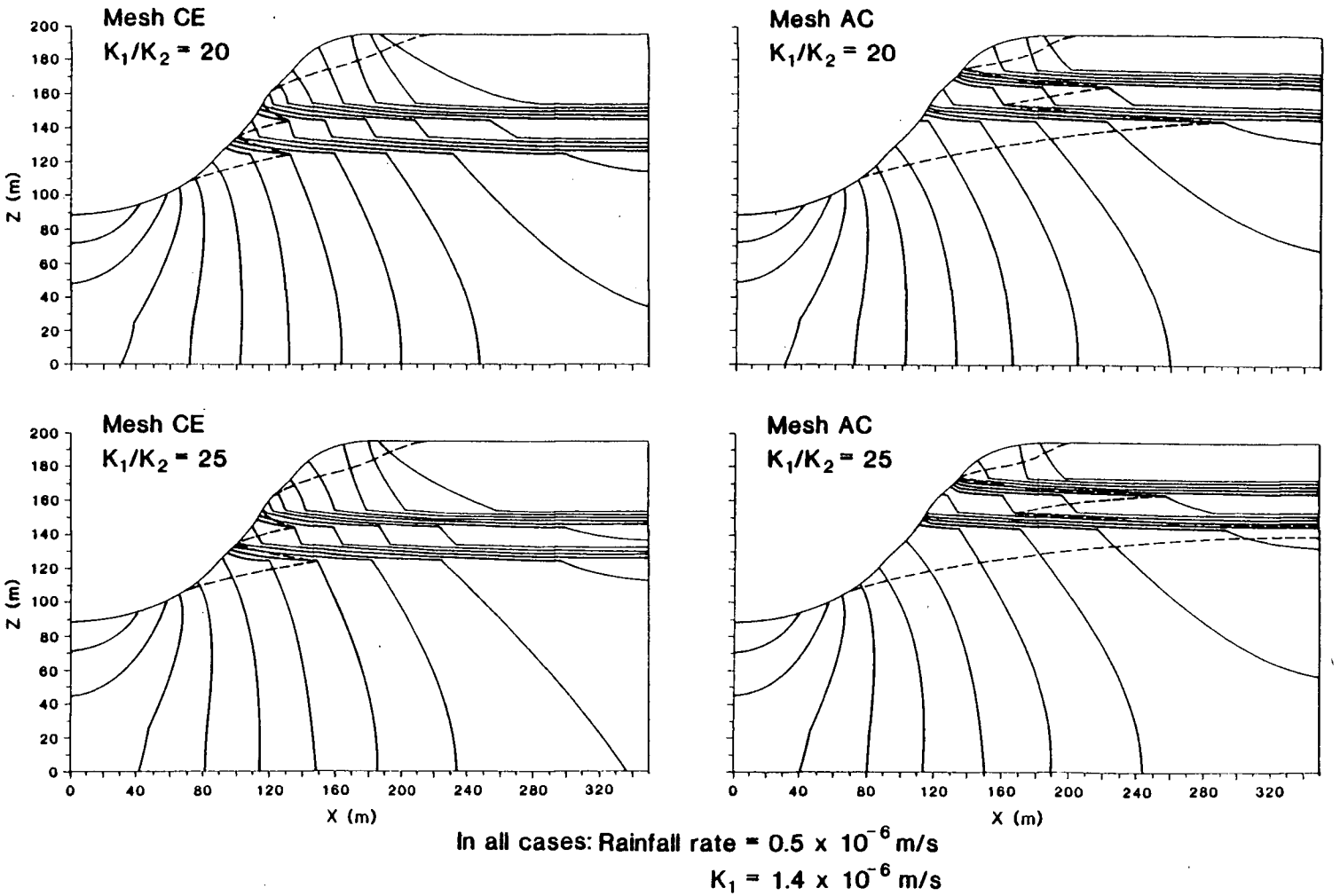

Figure 28. The effect of the elevation of the impeding layers and the hydraulic conductivity contrast on the unsaturated wedges for a constant distance separating the impeding layers.

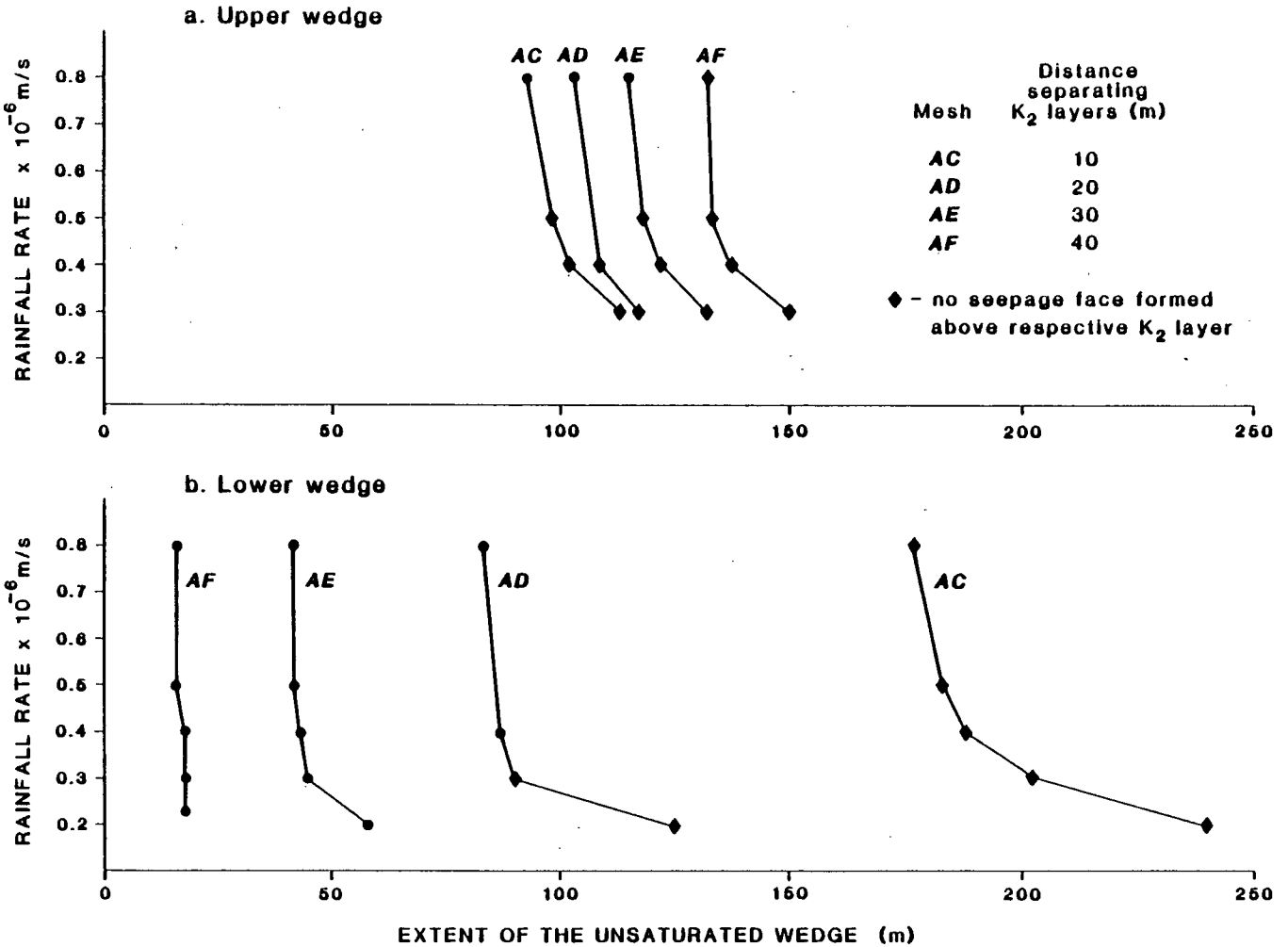

Figure 29. The relative extent of the unsaturated wedges for $K_1/K_2 = 20$.

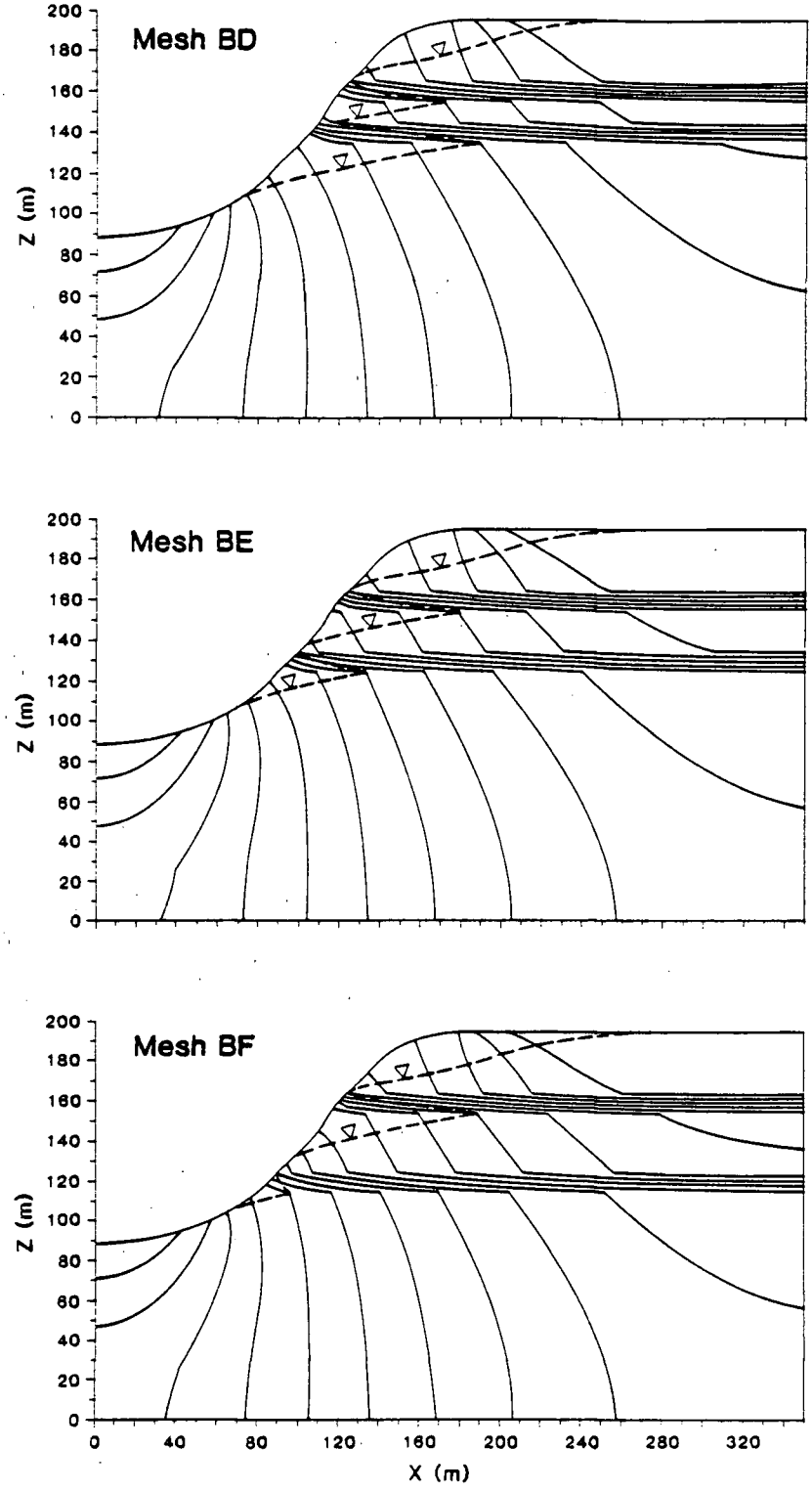

Figure 30. Comparison of the relative extent of the unsaturated wedges for K_1/K_2 = 20, K_1 = 1.4 x 10^{-6} m/s, and a steady-state rainfall rate of 0.3 x 10^{-6} m/s.

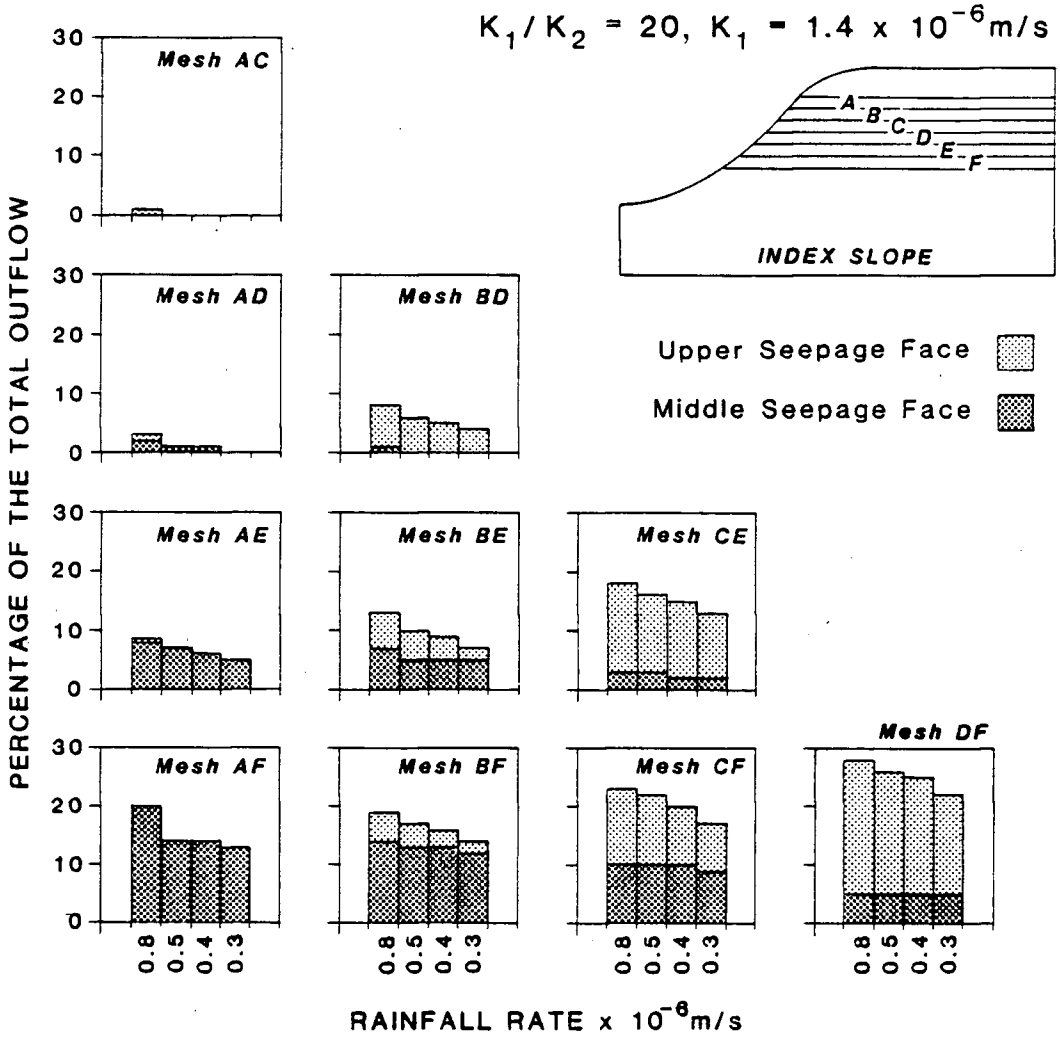

Figure 31. A comparison of the percentage of the total outflow discharged across the upper and middle seepage faces in two-layer systems.

remains fixed, then as the second layer is placed at successively lower positions, %Qu decreases and %Qm increases. Conversely, a comparison of the results along each row shows that if the position of the lower impeding layer remains fixed, then as the upper layer is placed at successively lower positions, %Qu increases and %Qm decreases. A comparison of the results along each diagonal shows that for a given distance separating the layers, an increase in the elevation of the layers decreases both %Qu and %Qm. The relative partitioning of the total outflow between the seepage faces depends upon the distance separating the impeding layers. For 10m of separation (Meshes AC, BD, CE, DF) %Qu > %Qm; for 20m of separation (Meshes AD, BE, CF), a consistent pattern is not developed; for 30 and 40 m of separation (Meshes AE, BF, AF), %Qu < %Qm.

The effect of K_1/K_2 on the percentage of the total outflow from each seepage face is summarized in Figure 32 for K_1/K_2 = 20, 30, 100, and 1000. Because of the reduction in K_2, the total flow through the hillside is decreased, on average, by 74% as K_1/K_2 is increased from 20 to 1000. In all cases, %Qu increases for an increase in K_1/K_2. The percentage from the middle seepage face remains relatively constant until K_1/K_2 is increased from 100 to 1000 where it is noticeably reduced. For $K_1/K_2 \geq 100$, %Qu >> %Qm and the middle seepage face is present only in association with layers E and F. The hydraulic-head distribution and water-table configuration is shown in Figure 33 for Mesh BF as K_1/K_2 is increased from 20 to 1000.

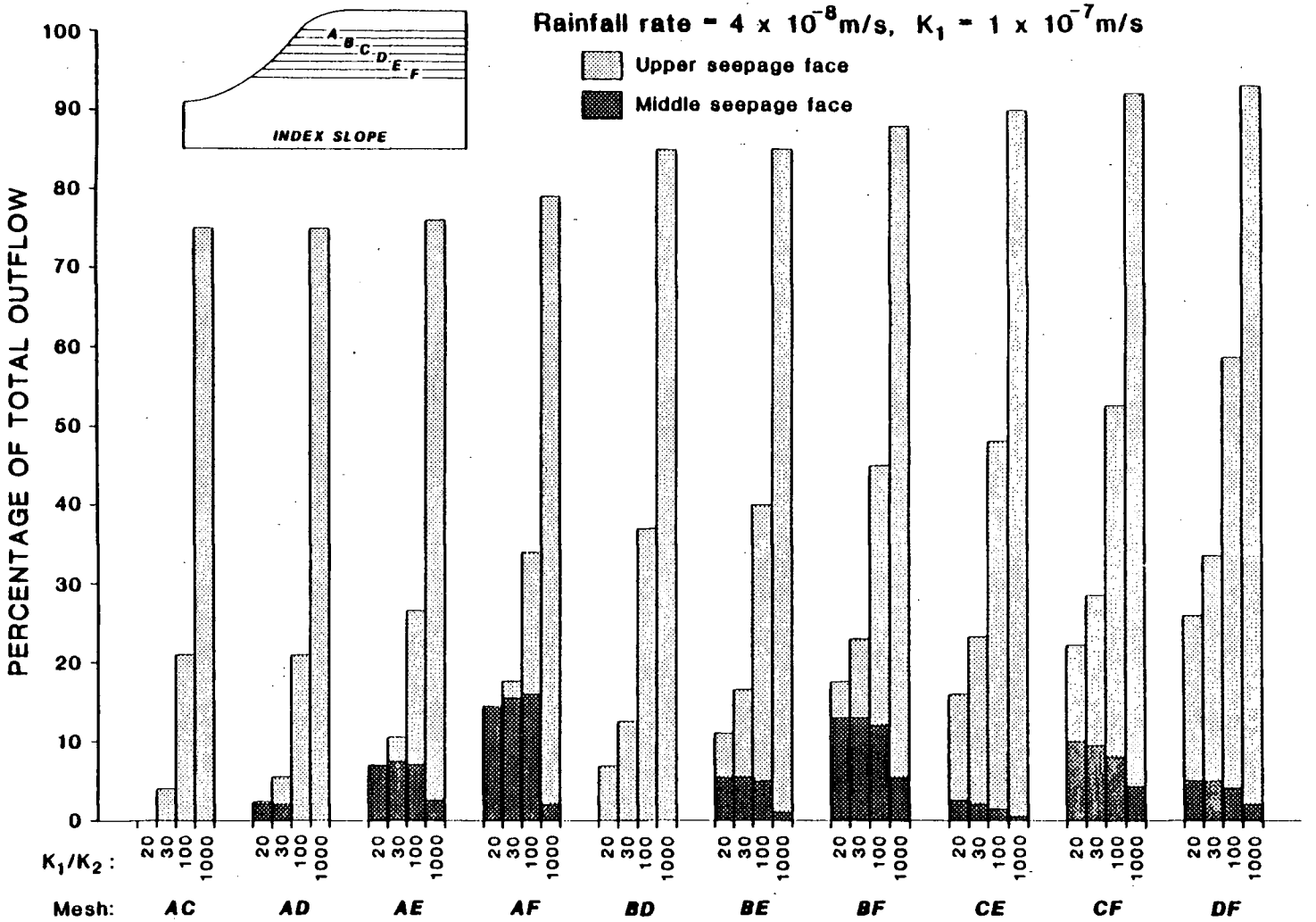

Figure 32. The effect of the hydraulic conductivity contrast on the percentage of the total outflow discharged across the upper and middle seepage faces formed in two-layer systems.

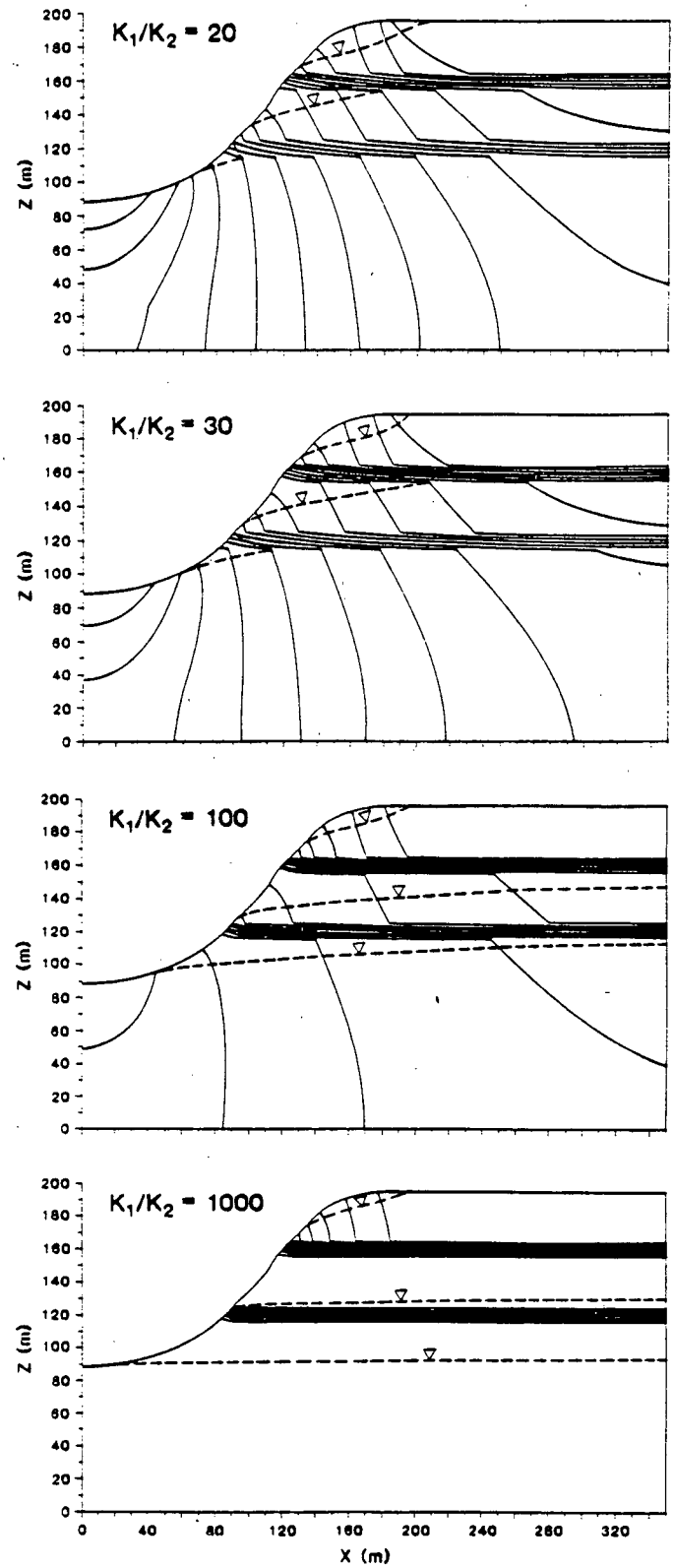

Figure 33. The effect of increasing the hydraulic conductivity contrast over several orders of magnitude for MeshBF, $K_1 = 10^{-7}$ m/s, and a rainfall rate of 4 x 10^{-8} m/s.

THREE-LAYER FLOW SYSTEMS

The development of multiple seepage faces in three-layer systems was studied with four layering sequences: ACE, BDF, ACF, and ADF. The addition of a third layer reduces the extent of all the unsaturated wedges, as shown in Figure 34. The total flow through the hillside decreases by 26% from the one-layer system to the three-layer system.

The relative extent of the unsaturated wedges for the three-layer systems is shown in Figure 35 for $K_1/K_2 = 20$. A comparison of Mesh ACE and Mesh BDF again illustrates that an increase in the elevation of the impeding layers increases the extent of the unsaturated wedges. For 10m separating two of the impeding layers, the extent of the upper wedge is less than or equal to that of the lower wedge; for 20 m separating two of the impeding layers, the reverse is true.

Figure 36 summarizes the relative percentages of the total outflow discharged across each seepage face for $K_1/K_2 = 20$, 30, 100, and 1000. Because of the reduction in K_2, the total flow through the hillside decreases, on average, by 82% as K_1/K_2 is increased from 20 to 1000. In all cases shown, the percentage of the total outflow from the uppermost seepage face increases as K_1/K_2 increases. For $K_1/K_2 \geq 100$, more than 80% of the flow through the hillside exits across it. The behavior of the seepage face formed above the middle impeding layer is less clear-cut. The percentage of the total outflow increases as K_1/K_2 increases from 20 to 30 and decreases from 100 to 1000. As K_1/K_2 increases from 30 to 100, the response depends upon

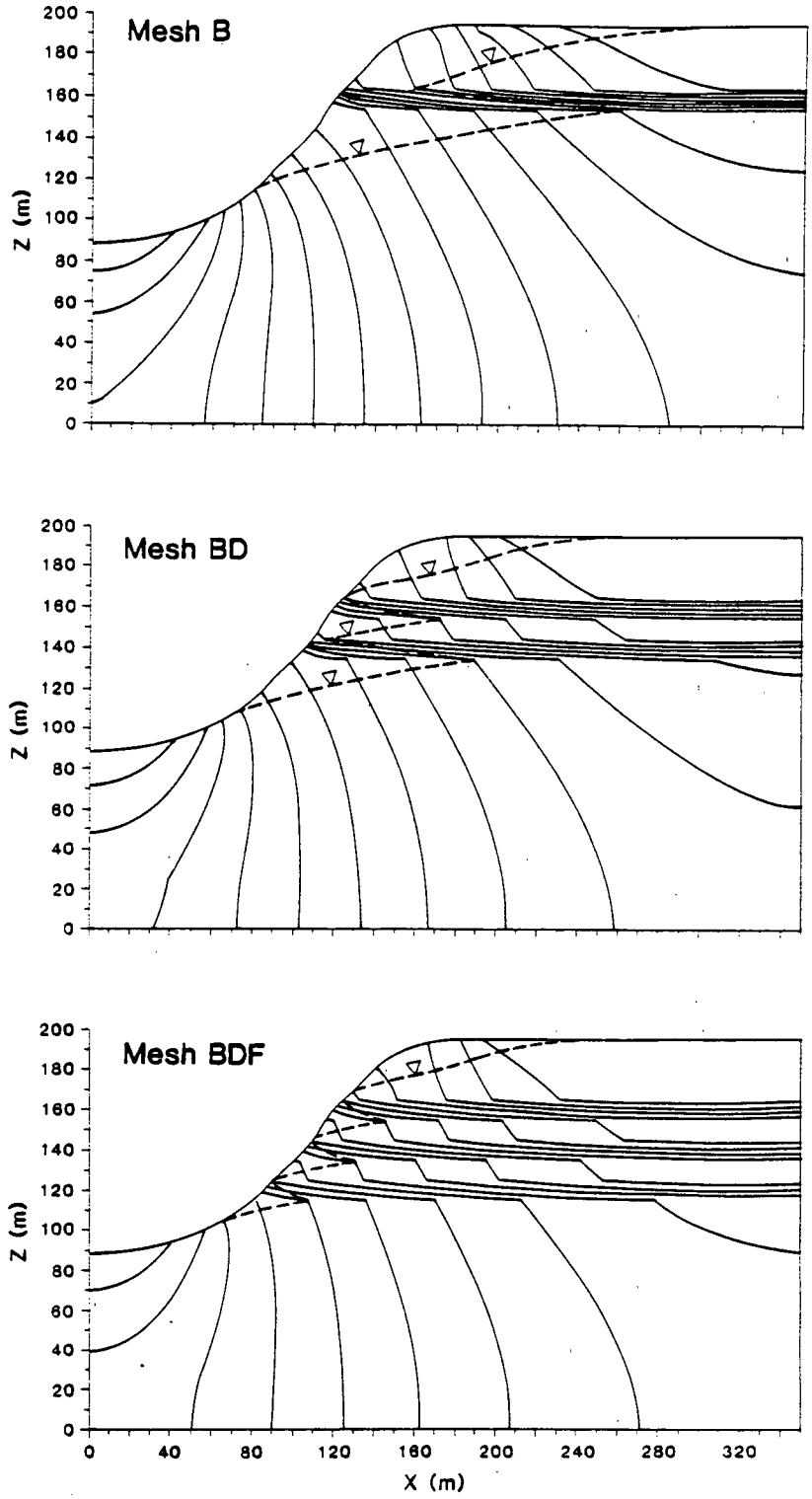

Figure 34. The effect of increasing the number of impeding layers for K_1/K_2 = 20, K_1 = 1.4 x 10^{-6} m/s, and a rainfall rate of 0.3 x 10^{-6} m/s.

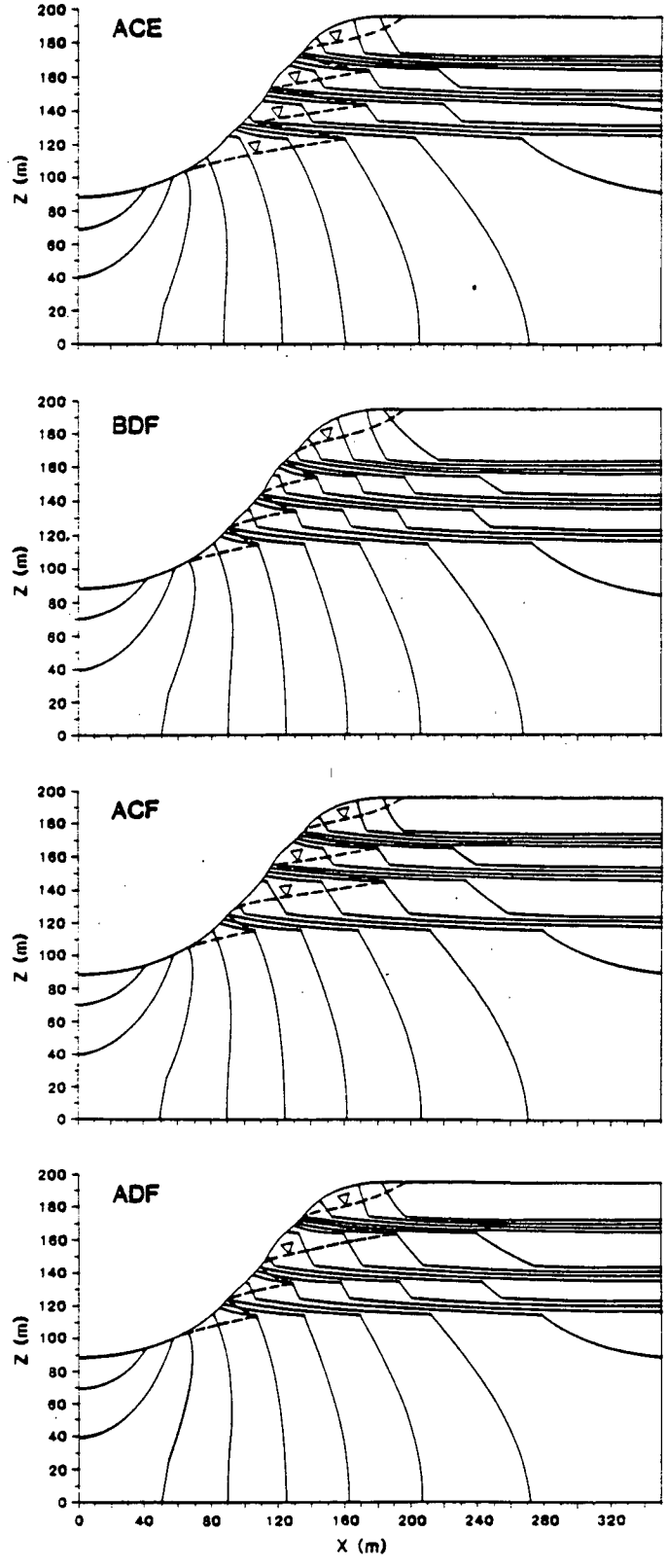

Figure 35. Three-layer systems for $K_1/K_2 = 20$, $K_1 = 10^{-7}$ m/s, and a rainfall rate of 4×10^{-8} m/s.

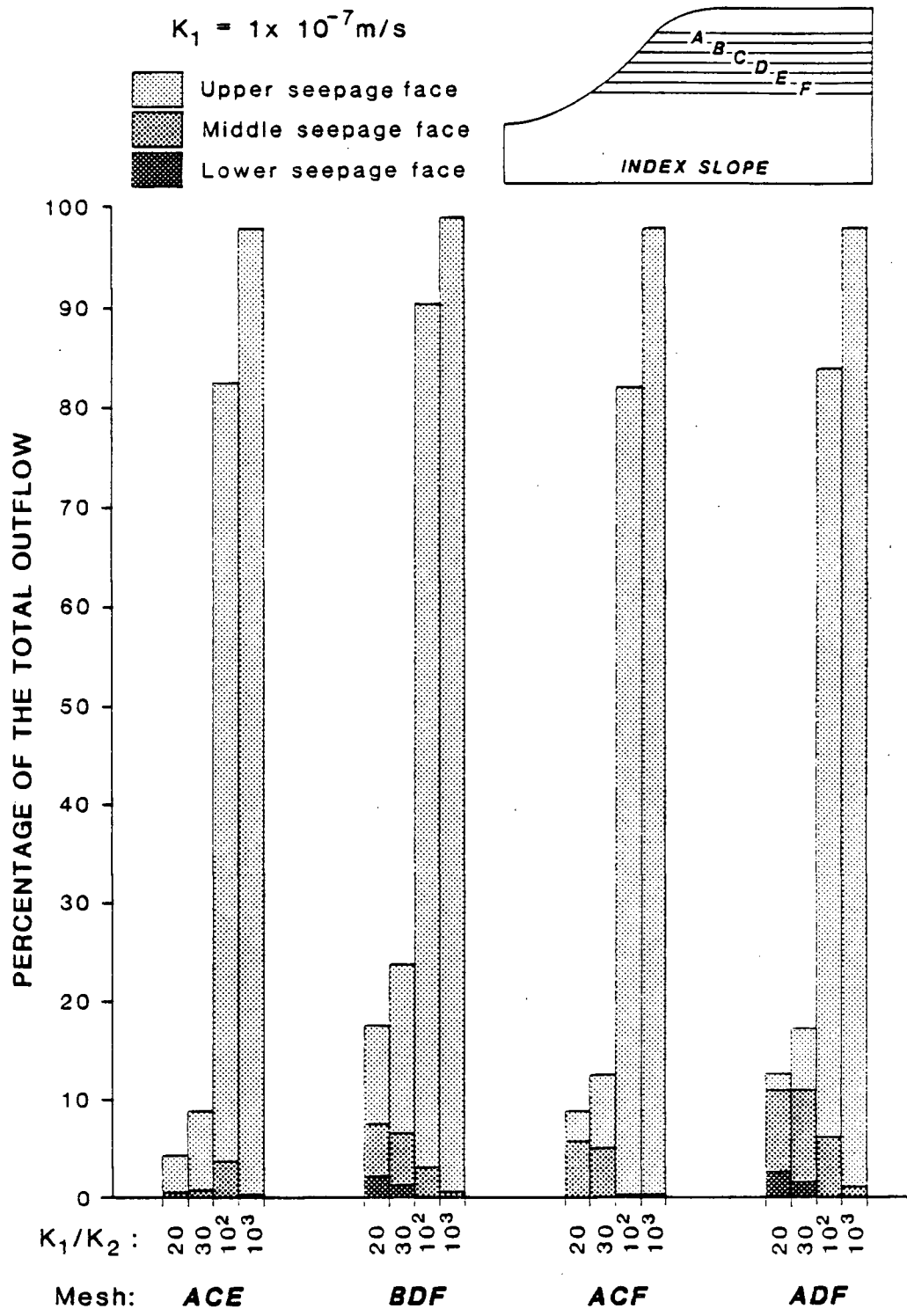

Figure 36. The effect of the hydraulic conductivity contrast on the percentage of the total ouflow discharged across the seepage faces formed in three-layer systems for a rainfall rate of 4 x 10^{-8} m/s.

the position of the middle impeding layer. If the seepage face is formed above layer C, the percentage of the total outflow increases; if formed above layer D, the percentage of the total outflow decreases. The seepage face formed above the lowermost impeding layer is present only in association with layer F. The percentage of the total outflow decreases as K_1/K_2 increases from 20 to 30 and the seepage face is absent for $K_1/K_2 \geq 100$.

ANISOTROPY

For flat-lying sedimentary rocks, it is common for the saturated hydraulic conductivity in the horizontal direction, K_x, to be up to ten times that in the vertical direction, K_z, within a given layer (Freeze and Cherry, 1979). It is also possible that in fractured rocks, K_z may exceed K_x. A preliminary study to investigate the effect of anisotropy was performed for a one-layer system. Throughout the entire analysis, the hydraulic conductivity contrast, measured in the vertical direction, was held constant and equal to 30. The results are shown in Figure 37. For the flow region shown in Figure 37a, both Material No. 1 and Material No. 2 are isotropic. In Figure 37b, Material No. 1 has been made anisotropic by increasing the value of K_x so that $K_x = 10K_z$. Material No. 2 has not been changed and remains isotropic. Note that in comparison with Figure 37a, the unsaturated wedge is more extensive and there is no longer ponding along the infiltration surface. Because K_x has been increased for Material No. 1, the total flow through the hillside increased

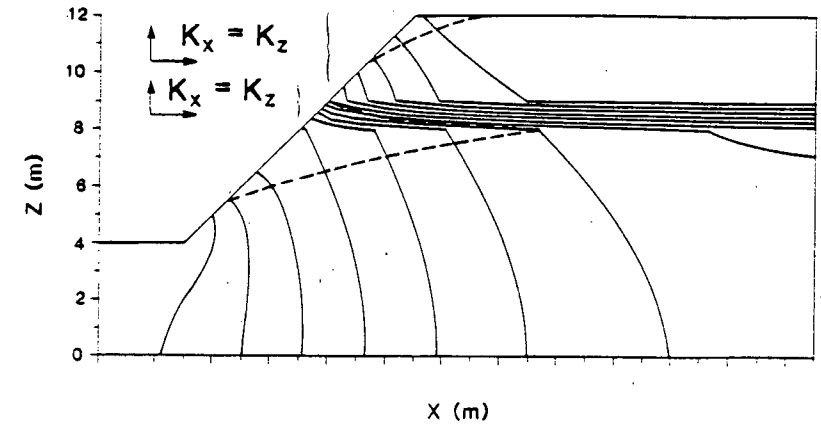

a. $K_{1x} = K_{1z} = 1 \times 10^{-7}$ m/s

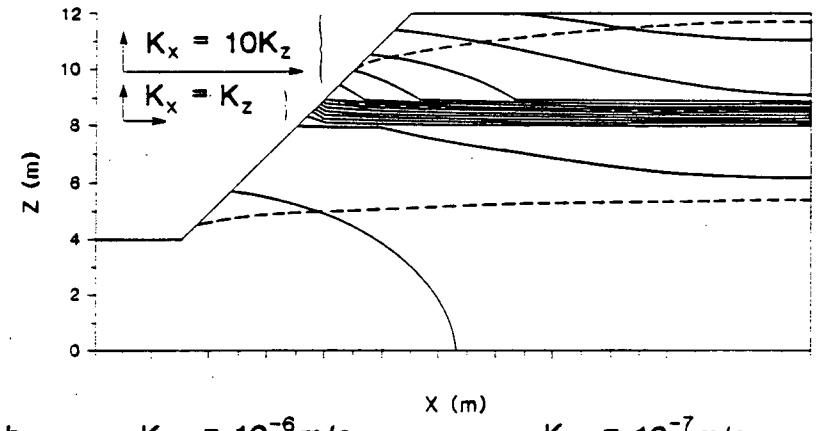

b. $K_{1x} = 10^{-6}$ m/s $K_{1z} = 10^{-7}$ m/s

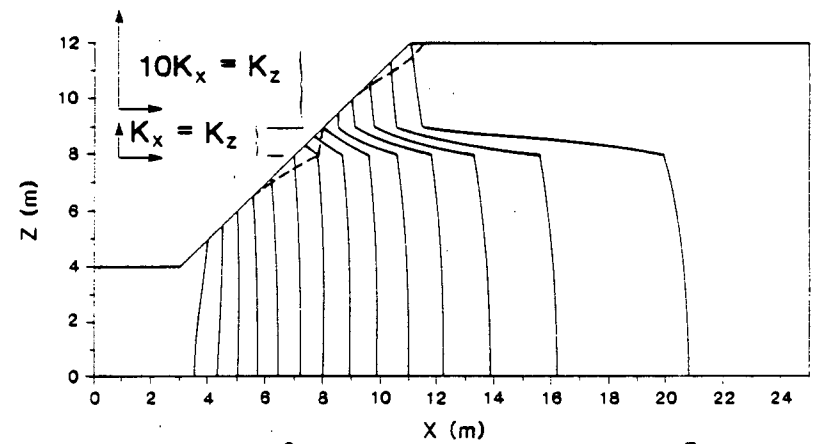

c. $K_{1x} = 10^{-8}$ m/s $K_{1z} = 10^{-7}$ m/s

Figure 37. The effect of anistropy for $K_1/K_2 = 30$ and a steady-state rainfall rate of 4×10^{-8} m/s.

by approximately 120%. In Figure 37c, Material No. 1 has been made anisotropic by reducing the value of K_x so that K_x = 1/10 K_z; Material No. 2 again remains isotropic. Note that in comparison with Figure 37a, the unsaturated wedge is greatly reduced. Because K_x has been reduced for Material No. 1, the total flow through the hillside is decreased by approximately 78% from Figure 37a.

Figure 37 has shown that the water-table configuration is sensitive to anisotropy within Material No. 1. However, similar studies showed that anisotropy within Material No. 2 did not produce solutions that were significantly different from that shown in Figure 37a. It appears that anisotropy within the impeding layer is secondary to the effect on the system of a hydraulic conductivity contrast of 30, measured in the vertical direction.

SLOPE ANGLE

Figure 38 shows the water-table configuration as a function of the hydraulic conductivity contrast for a relatively low slope angle of 8°. Multiple seepage faces do not form until the ratio K_1/K_2 exceeds 200. Recall that one order of magnitude difference in K_1 and K_2 was sufficient to produce multiple seepage faces on the 40° slopes studied previously. Therefore, if all else is constant, then a greater hydraulic conductivity contrast is required to produce multiple seepage faces on gentle slopes as compared with steep slopes.

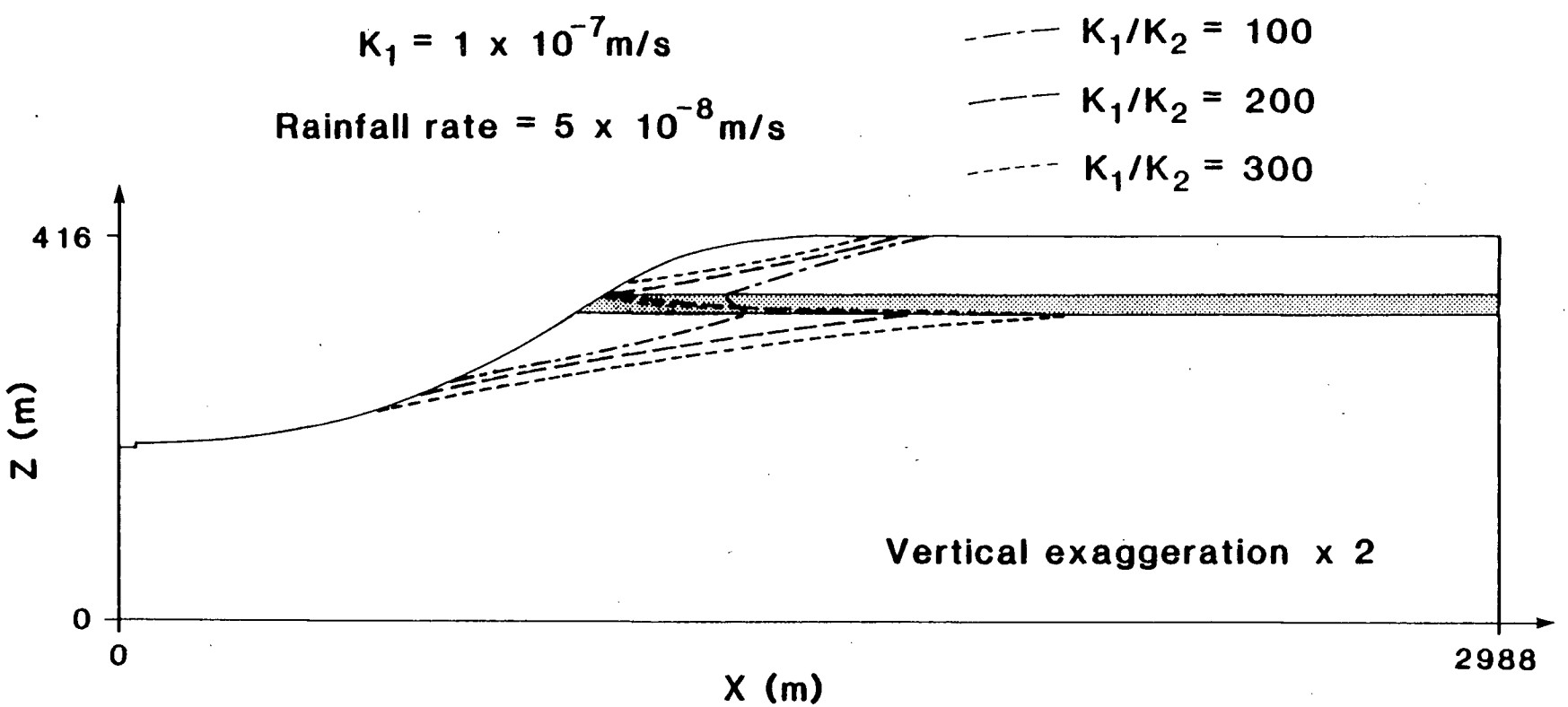

Figure 38. The water-table configuration as a function of the hydraulic conductivity contrast for a slope angle of 8°.

4.3 Discussion

The results presented in the previous section have shown the hydraulic-head distribution and water-table configuration to be complex in layered slopes. From these results, generalizations can be made regarding the effect of the hydraulic conductivity contrast and the position of the impeding layer on the solution. These generalizations are made with reference to the one-layer flow systems in which they are particularly clear, but they are also evident in the more complex results presented for two- and three-layer systems.

First, if all other factors are equal, then an increase in the ratio K_1/K_2 increases both the extent of the unsaturated wedge and the percentage of the total outflow from the seepage face formed above the impeding layer. To explain this, consider the refraction of flow that occurs within a fully-saturated flow region containing a less-permeable soil layer, as shown in Figure 39. When this type of refraction occurs in the vicinity of a slope, water leaves the flow region through the more permeable material above and below the impeding layer. The flux through the layer cannot match the outflow rate from the material below it unless an unsaturated wedge forms. If the ratio K_1/K_2 is increased by decreasing K_2, the flux through the layer decreases and a smaller hydraulic gradient is required to deliver the reduced quantity of water to the discharge area below. Consequently, the slope of the water table beneath the impeding layer decreases and the extent of the unsaturated wedge increases. Since less of the total inflow can pass

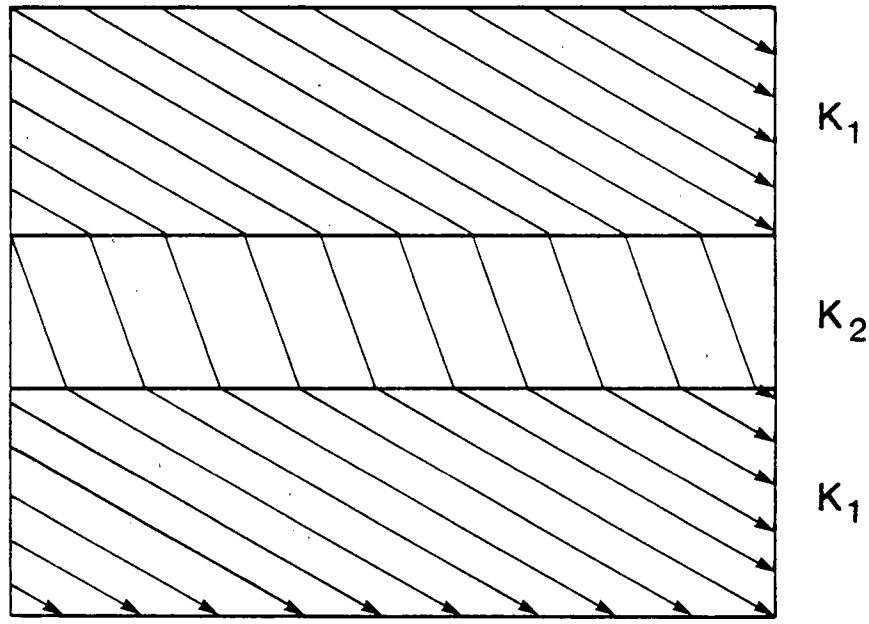

$K_1 > K_2$ $\quad$ $K_1/K_2 = 10$

Source: Freeze and Cherry, 1979.

Figure 39. Refraction of groundwater across a less-permeable layer.

through the impeding layer, a larger percentage of the total outflow exits across the seepage face formed above the impeding layer.

The second generalization is that if all other factors are equal, then a decrease in the elevation of the impeding layer decreases the extent of the unsaturated wedge and increases the percentage of the total ouflow from the uppermost seepage face. To explain this, one needs to recognize that the lower portion of the slope is a discharge area and the major component of flow is directed horizontally towards the water table bounding the unsaturated wedge and towards the uppermost seepage face. This reduces the extent of the unsaturated wedge and increases the percentage of the total outflow across the uppermost seepage face. The converse is true if the impeding layer is located in the upper portion of the slope where the major component of flow is directed vertically downwards.

These generalizations can be used to predict the combination of hydrogeologic variables most likely to produce multiple seepage faces in one-layer flow systems. In general, multiple seepage faces are likely to be present on steep slopes in which the ratio of K_1/K_2 is at least an order of magnitude. For K_1/K_2 on the order of 20 or 30, steady-state multiple seepage faces are more likely to be present if the impeding layer is located in the lower two-thirds of the slope. Regardless of the position of the layer, steep slopes in which $K_1/K_2 \geq 100$ feature multiple seepage faces and an unsaturated

zone beneath the layer that may be quite extensive, as indicated in Figure 27.

With regard to the effect of the rainfall rate, note that in Figures 23 and 25, $K_1 = 1.4 \times 10^{-6}$ m/s and the steady-state rainfall rate has been varied between 1.0×10^{-6} m/s (32 m/year) and 0.3×10^{-6}m/s (9m/year). These steady-state rainfall rates are unrealistic; average annual rainfall rates in North America generally vary between 8.0×10^{-8}m/s (2.5m/year) and 8×10^{-9}m/s (.25 m/year) (Barry and Chorley, 1976). However, by an appropriate scaling of the hydraulic conductivity, the same results shown in Figure 23 and 25 can be obtained for steady-state rainfall rates within the range expected in North America. One can invoke similitude considerations to show that this is so. In essence, if we model two flow regions that have the same size and geometry, the same type of boundary conditions, and the same hydraulic conductivity contrast, then the hydraulic-head distributions predicted by the finite-element model will be identical if:

$$\frac{(R)_1}{(K_1)_1} = \frac{(R)_2}{(K_1)_2} \qquad 4.2$$

where R is the rainfall rate and the subscripts outside the parentheses refer to the respective flow region. This is true only if the $K(\psi)$ curves are scaled in accordance with Equation 4.1 and if the $\theta(\psi)$ curves remain constant, as discussed in Section 4.1.

A proof of Equation 4.2 can be given for one-dimensional, saturated flow through a layered soil column. Proof of

Equation 4.2, as applied to saturated-unsaturated flow through layered hillsides, would require an analysis similar to that of Verma and Brutsaert (1971) in which the boundary-value problem is formulated and solved in terms of dimensionless variables selected to characterize the flow process. Kline (1965) presents a detailed discussion of the general methods used in such analyses and Hubbert (1937) provides a good introduction to the subject of similitude. To the author's knowledge, a rigorous proof of Equation 4.2 has not been performed for the boundary-value problem considered in this thesis. However, the empirical validity of Equation 4.2 has been tested and confirmed by the author with computer simulations.

In view of Equation 4.2, the results presented in Figures 23 and 25 would hold for an infinite number of combinations of R and K_1, some of which are realistic and some are not. The results of the sensitivity study apply to the range of annual rainfall rates encountered in North America for values of K_1 between 10^{-7} m/s and 10^{-8} m/s. For K_1 $<10^{-8}$ m/s, the solutions are insensitive within this range of rainfall rates because the maximum amount of water the hillside can transmit is less than that delivered to the infiltration boundary. Problems involving numerical instability prevented the study of realistic rainfall rates applied to regions in which $K_1 > 10^{-7}$ m/s.

LIMITATIONS AND ASSUMPTIONS

Of the assumptions and limitations associated with the mathematical model, the following three are the most important

in terms of their potential effect on the steady-state analysis:

1. Flow is two-dimensional. This assumption restricts the applicability of the results to flow regions in which the hydraulic gradient in the third dimension is negligible. For example, a three-dimensional analysis would be required to model flow along slopes that are deeply incised by gulleys or in cases where the lower permeability material exists in the form of lenses as opposed to layers. In addition, the assumption implies that infiltration and the soil properties are uniform in the third dimension.

2. There is no infiltration along the seepage-face boundary. In reality, water may be available to infiltrate along the slope as a result of direct rainfall or surface runoff; neither has been modeled. For near-vertical slopes, restriction of infiltration to the flat upland surface is a reasonable assumption. It is not reasonable, however, for gentle slopes and one would expect that the unsaturated wedge would be considerably less extensive if infiltration were to be modeled along the seepage-face boundary. For the steep slopes considered in the present study, this assumption might introduce error for relatively low values of K_1/K_2. However, for $K_1/K_2 \geq 100$, it seems reasonable to believe that the relative importance of infiltration along the slope would decrease and extensive unsaturated wedges would prevail.

3. A numerical solution may not be possible when steep gradients in pressure head and hydraulic conductivity develop

within the unsaturated zone. This limitation prevented the study of layered systems for low rainfall rates. A new model developed by Cooley (1983) that uses the subdomain finite-element method appears to have overcome the numerical problems encountered in the present study. Stephenson and Freeze (1974) found that by modifying the shape of the $K(\psi)$ curve until K varied over only one order of magnitude, their instability problems could be controlled. In the present study, this latter approach reduced, but did not cure, the problem. An alternative solution is to design the finite-element mesh with closely spaced nodal points in areas where the driest conditions are anticipated. This was done for the transient analysis, but not for the steady-state simulations. For the purposes of the steady-state analysis, the lower limit on the rainfall rate imposed by numerical instability was simply accepted because multiple seepage faces generally formed at higher rainfall rates for the majority of geologic materials.

Chapter 5

TRANSIENT ANALYSIS

The sensitivity study in the previous chapter provided information about the steady-state conditions under which multiple seepage faces occur. In order to examine the response of these flow systems to individual rainfall events and to examine the mechanisms by which multiple seepage faces develop, a transient analysis must be performed.

Freeze (1971) studied the transient development of perched water tables with a finite-difference model of saturated-unsaturated flow. The flow region he modeled is shown in Figure 40a. There is an impeding layer in the center of the hillside and a region of relatively high hydraulic conductivity at the base of the hillside. The remainder of the flow region is composed of material with an intermediate value of hydraulic conductivity. The flow region is 37 m by 7 m. The boundary conditions include a constant-head boundary, AB, and impermeable boundary, AFED, and an infiltration boundary, BCD. Static initial conditions were used for the simulation. Rainfall was simulated at a rate of $0.09K_o$ (1.5 mm/hr) where K_o is the saturated hydraulic conductivity of the soil present along the infiltration boundary. Figure 40b shows the transient response of the water table. A perched water table formed as a small lens above the impeding layer after 210 hours. The lens extended to the far-right impermeable boundary after 260 hours and continued to build until at 460 hours, the perched water

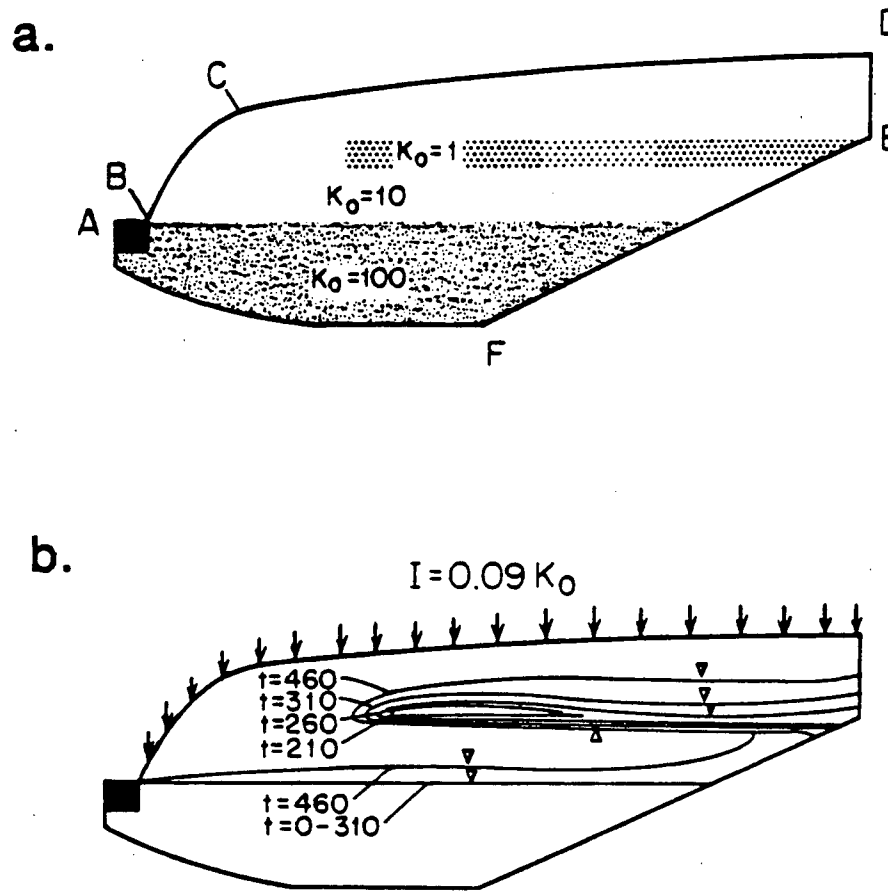

(Source: Freeze, 1971)

Figure 40. Transient simulation of the development of a perched flow system, (t, time in hours).

table joined the slowly rising main water table. This example provides insight into the mechanisms by which perched water tables form. The simulations presented in this chapter extend our knowledge to include hillside in which the impeding layer intersects the slope and multiple seepage faces develop. The results of two transient simulations are presented below, followed by a discussion of the numerical difficulties that were encountered.

The finite-element mesh shown in Figure 41 was used for the transient simulations. The flow region is 12 m by 25 m and has a slope of 45°. In an attempt to circumvent problems with numerical instability, nodes were spaced closely in these portions of the flow region where the steepest ψ-gradients were expected to occur. Near the infiltration boundary, the nodal spacing in the vertical direction was 0.1 m. This distance increased to 2 m in the basal portion of the flow region. It should be noted that the sensitivity of the solution to the nodal spacing was not tested. The first transient simulation using this mesh involves a hillside containing one impeding layer; the second simulation contains two.

The one-layer flow system is shown in Figure 42. AF is a constant-head boundary along ψ = 0.5 m, ABCD is an impermeable boundary, DE is an infiltration boundary, and EF is a seepage-face boundary. A 1-m thick layer of less permeable material is located in the upper portion of the hillside; the hydraulic conductivity contrast is 25. The hydraulic properties of the two soil types are listed in Table 8.

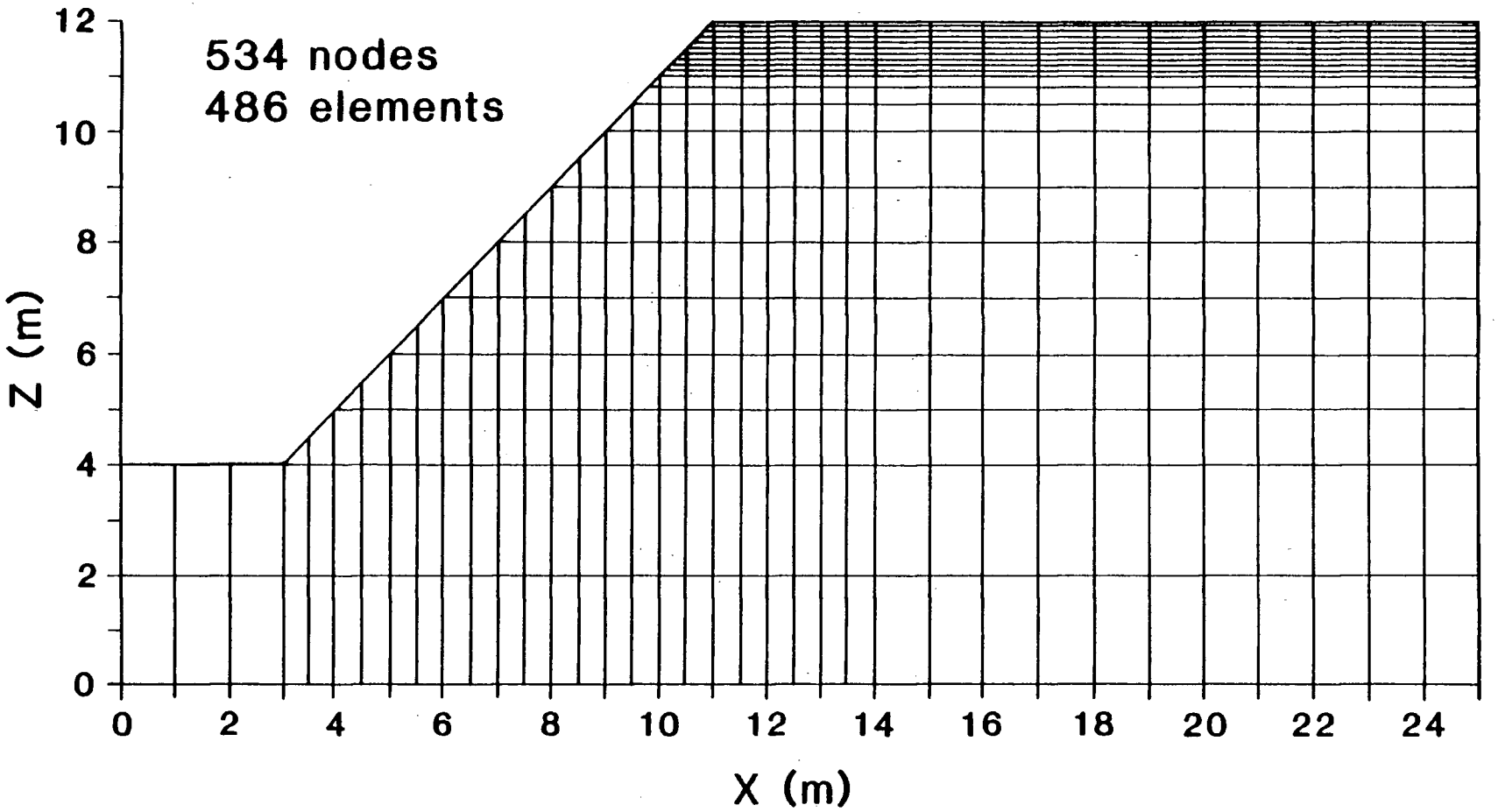

Figure 41. Finite-element mesh used in transient simulation.

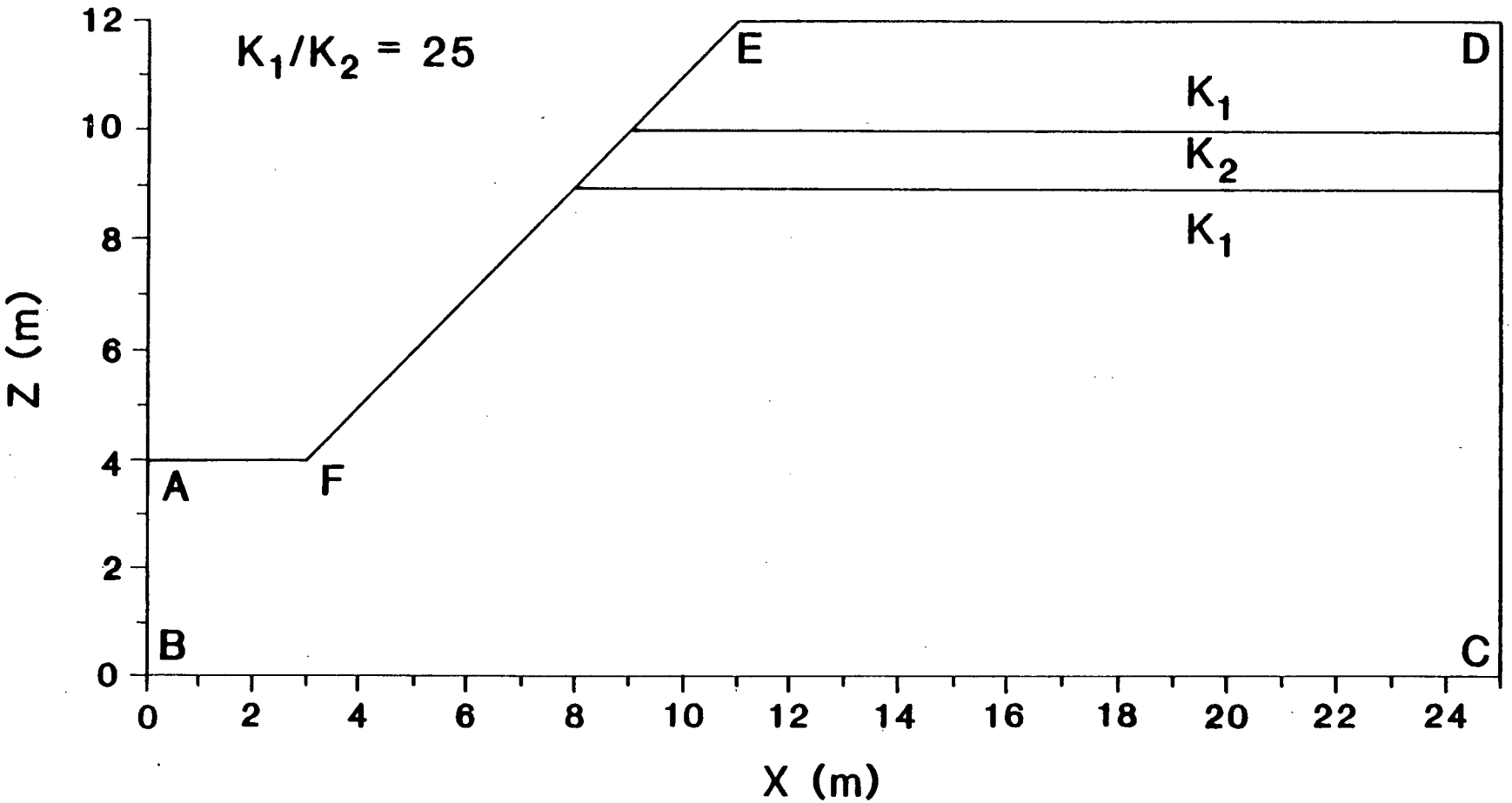

Figure 42. One-layer flow system for the transient simulation.

The values for the compressibility of the materials were taken from Table 1 and are in the middle of the range measured for a variety of geological materials. The specific storage was calculated from Equation 2.7. The characteristic curves used in the transient analysis have the same shape as those used in the steady-state analysis (Figure 21) except that they have been scaled to correspond to the values of the saturated hydraulic conductivity and porosity shown in Table 8.

Table 8. Hydraulic properties used in the transient simulations.

	Material No. 1	Material No. 2
saturated hydraulic conductivity, K, (m/s)	10^{-6}	4×10^{-8}
porosity, n	.450	.150
compressibility, α, $(\frac{ms^2}{kg})$	10^{-8}	10^{-9}
specific storage, S_s,(m)	9.994×10^{-5}	1.045×10^{-5}

The initial conditions were taken as the steady-state ψ values for an average annual rainfall rate of 1.2×10^{-7} m/s (3.8 m/yr). At time, t, greater than zero a rainfall rate of 9.0×10^{-7} m/s (3.24 mm/hr) was simulated along the infiltration boundary. The size of the initial timestep was one hour and each subsequent timestep was increased by a factor of 1.4 to a maximum size of 12 hours. Convergence was generally obtained within three to five iterations per timestep; the cumulative material balance error remained within 3% for the 14-day storm.

Figure 43 shows the transient response of the water table. After 24 hours, the perched water table intersected the infiltration boundary and continued to build until at t=118 hours, a seepage face formed above the impeding layer. After t=118 hours, the uppermost seepage face became more extensive. Note, however, that in this simulation the main water table adjacent to the constant-head boundary dropped slightly during the storm. This feature will be discussed following the second transient example.

A transient simulation was also made with the two-layer flow system shown in Figure 44. The only change from Fig 42 is the introduction of a second impeding layer. The boundary conditions, the hydraulic properties, the initial conditions, and the rainfall event are unchanged from the previous example. Figure 45 shows the response of the water table. After 58 hours, the uppermost perched water table intersected the infiltration boundary. A seepage face formed above the impeding layer at t = 154 hours. The perched water table associated with the lower impeding layer extended slightly towards the slope during the 14-day storm. Once again, the main water table dropped slightly during the simulation. In comparison with the one-layer case, approximately 34 additional hours were required in the two-layer system for ponding to occur along the infiltration surface and for a seepage face to form. This difference is due to the initial water-table configuration; in the one-layer case, the perched water table

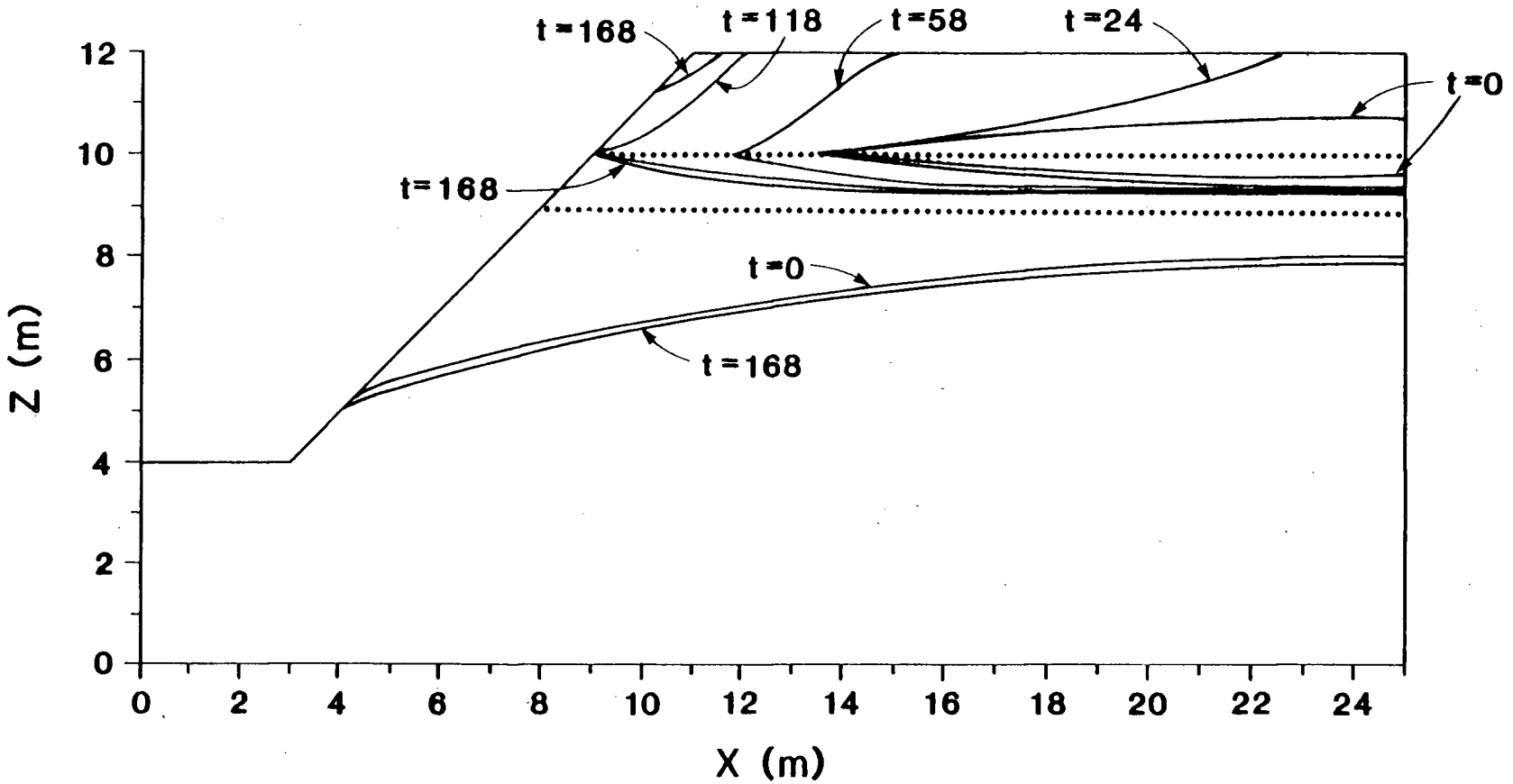

Figure 43. Transient response of the water-table for the one-layer flow system; t = time in hours.

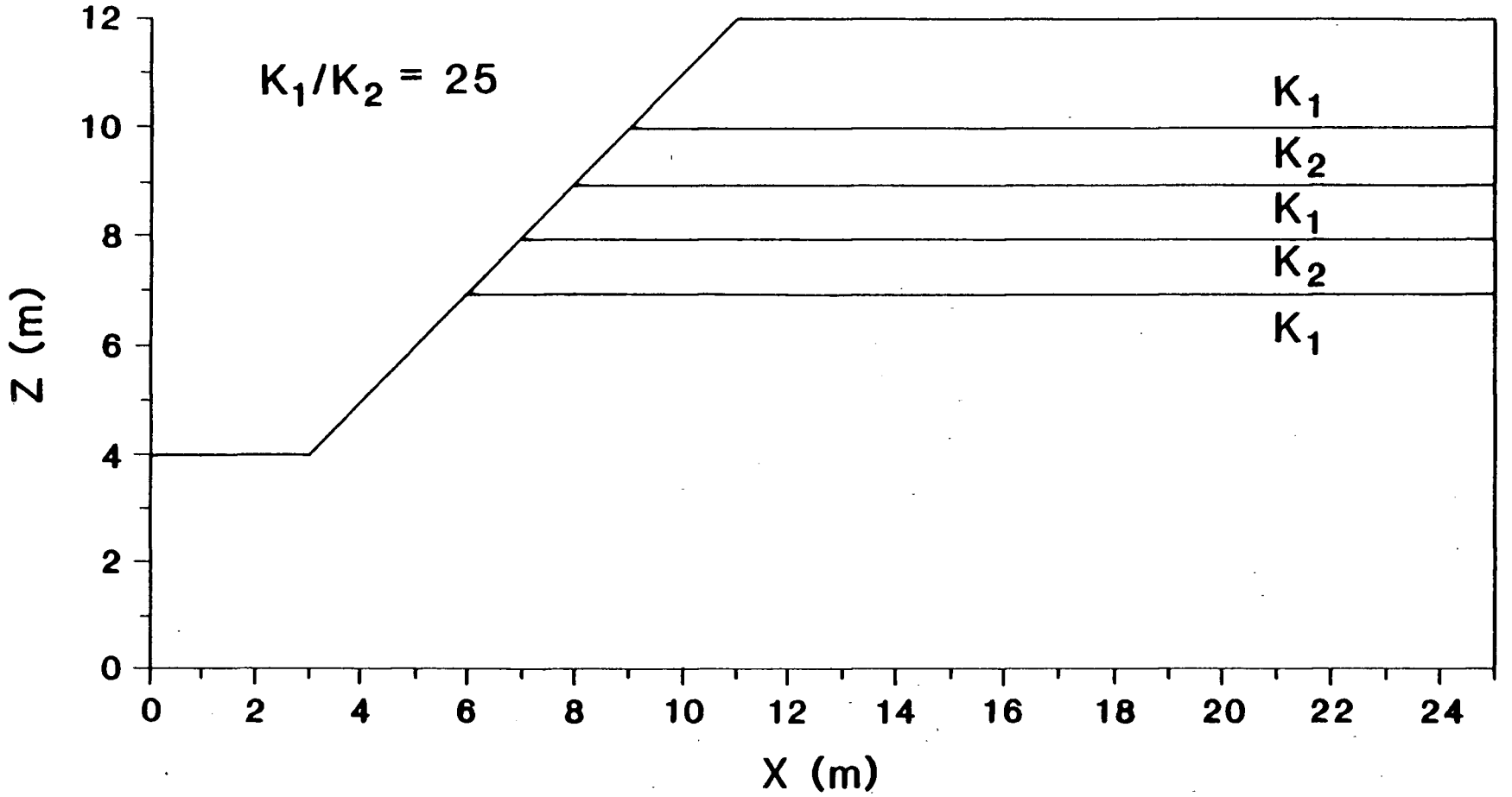

Figure 44. Two-layer flow system for the transient simulation.

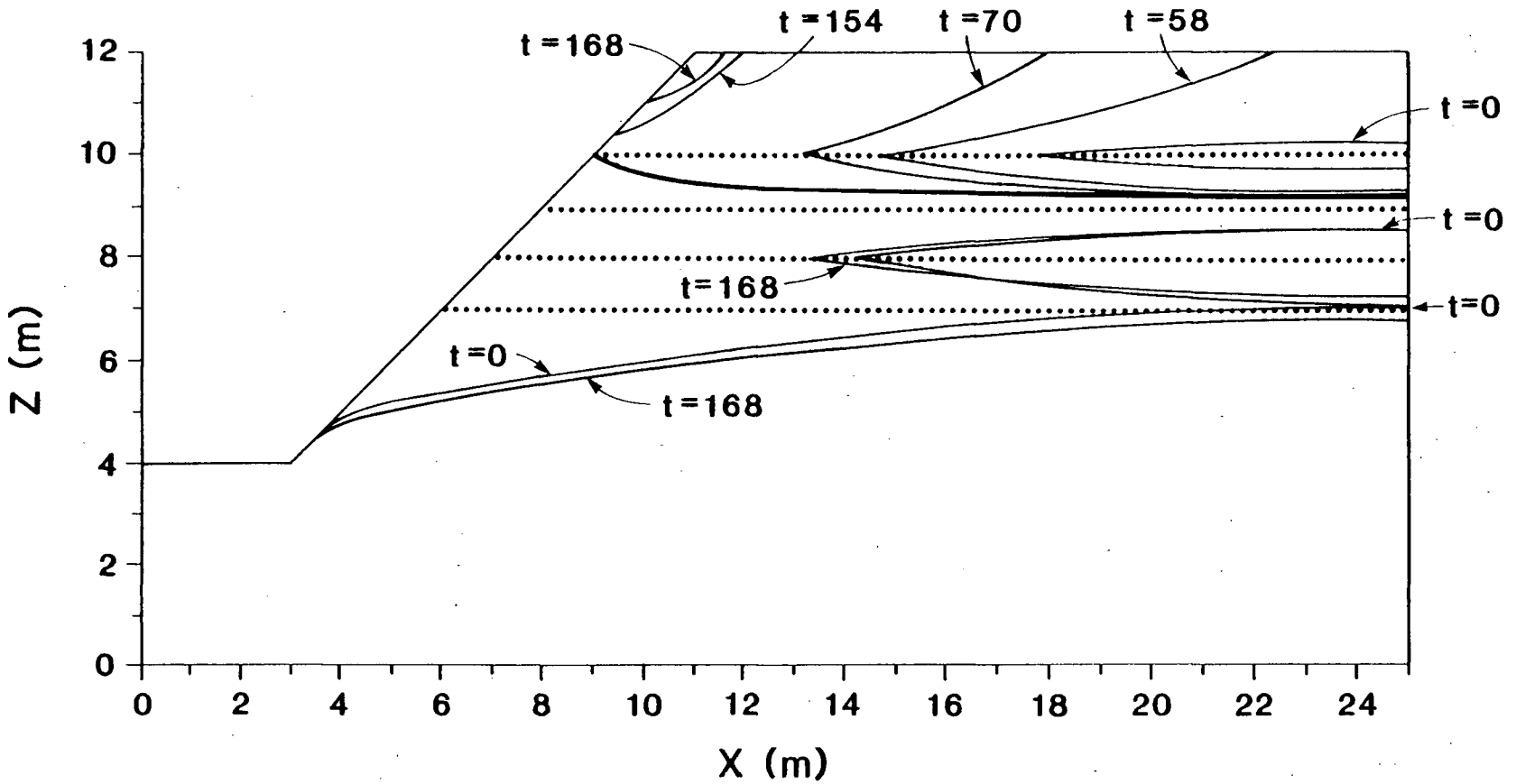

Figure 45. Transient response of the water table for the one-layer flow system; t = time in hours.

is closer to the soil surface at t=0 and therefore responds more quickly.

As noted in both transient simulations, the main water table dropped with time. For the cases at hand, which involve infiltration into a steady-state initial condition, one would not expect a decline in the main water table during the infiltration event. A failure to rise can be defended on the ground that the rate of propagation of the wetting front is retarded by the low-permeability layers, but a decline, even the slight one observed, probably points to a minor numerical problem in the program. Investigations of this issue were carried out and it is now apparent that the discrepancy arises from the slightly different numerical algorithms that are used to produce steady-state solutions in: (a) a true steady-state analysis in which the right-hand side of the transient equation is set equal to zero as in Equation 2.11, and (b) a steady-state analysis obtained by extending a transient simulation to steady state. In the two transient simulations under discussion, the initial conditions were set with method (a), but the simulation is proceeding by method (b). In the time period prior to the arrival of the wetting front, the heads at depth are moving towards a slightly different steady-state configuration than the one initially imposed. The numerical problem is probably a minor one, but it ought to be addressed before a full transient sensitivity analysis is carried out.

Chapter 6

APPLICATIONS

The information contained in this thesis has application to studies that require an understanding of the groundwater conditions in layered slopes. Applications to geotechnical, hydrogeological, and geomorphological problems will be discussed in this chapter. The first section deals with applications to slope-stability problems; the second section contains a descriptive analysis of other possible applications, such as controlling groundwater inflows into excavations, predicting regional groundwater flow patterns, and studying hillslope processes involved in landform development.

6.1 Slope Stability

Slope stability problems arise in both manmade and natural slopes. For manmade slopes, geotechnical engineers must ensure that the height and slope angle are designed with an adequate margin of safety against slope failures. Such projects include the design of highway and railway cuts, the design of embankments, and the design of open-pit mines. The problems associated with natural slopes generally involve the assessment of the stability of an existing slope.

Evaluation of the long-term stability of a slope is based on the following expression for the shear strength of the soil, S:

$$S = \bar{c} + (\sigma - p) \tan \bar{\phi} \qquad 6.1$$

where $\bar{c}$ = effective cohesion, $(\sigma-p)$ = effective stress, σ = total stress, p = fluid pressure, and $\bar{\phi}$ = effective angle of internal friction. All terms except the latter have units of $[ML^{-1}T^{-2}]$. The effective cohesion and the effective angle of internal friction are empirical soil parameters that are determined from laboratory tests. The total stress is generally calculated from the statics of the problem. The fluid pressure can be calculated either from direct measurement of the pressure head along the failure surface, or from the hydraulic-head values obtained from flownet construction. Recall from Chapter 2 that fluid pressure, p, pressure head, ψ, and hydraulic head, h, are related through the following two equations:

$$p = \rho g \psi$$

$$h = \psi + z$$

For unsaturated soils, an empirical parameter χ has been introduced by Bishop and Blight (1963) to relate effective stress to fluid pressure as follows:

$$\bar{\sigma} = \sigma - \mu_a + \chi(\mu_a - \mu_w)$$

where $\bar{\sigma}$ = effective stress, μ_a = air pressure in the pore spaces, μ_w = water pressure, and χ = parameter related to the degree of saturation of the soil. Recent research on the strength of unsaturated soils is reviewed by Fredlund, et al. (1978) and Fredlund (1979).

The factor of safety against slope failure, F.S., is defined as the ratio of the shear strength along a potential failure surface to the shear stress along that surface. For a stable slope, F.S.>1. From Equation 6.1, it can be seen that an increase in the fluid pressure decreases the shear strength and hence, the factor of safety. Or, viewed another way, if all other factors are equal, then the lower the fluid pressures, the steeper the stable slope angle. Knowledge of the groundwater conditions that exist within a hillside are therefore of fundamental importance to long-term stability analyses.

Practicing engineers are well aware that the geology of a site can have a profound effect on the fluid-pressure distribution. Studies that have emphasized the importance of the hydrogeologic environment in stability analysis include Patton and Deere (1971), Deere and Patton (1971), Patton and Hendron (1974), and Hodge and Freeze (1977). However, collection of hydrogeologic data in the field is an expensive and difficult technical problem. The sophistication of the fluid-pressure distribution used in a stability analysis will therefore depend upon the amount of data that is available and its quality. To illustrate this, suppose a stability analysis is to be performed for the hillside shown in Figure 46a. One could envision the following four types of groundwater conditions that might be invoked in the analysis, depending upon the availability of data:

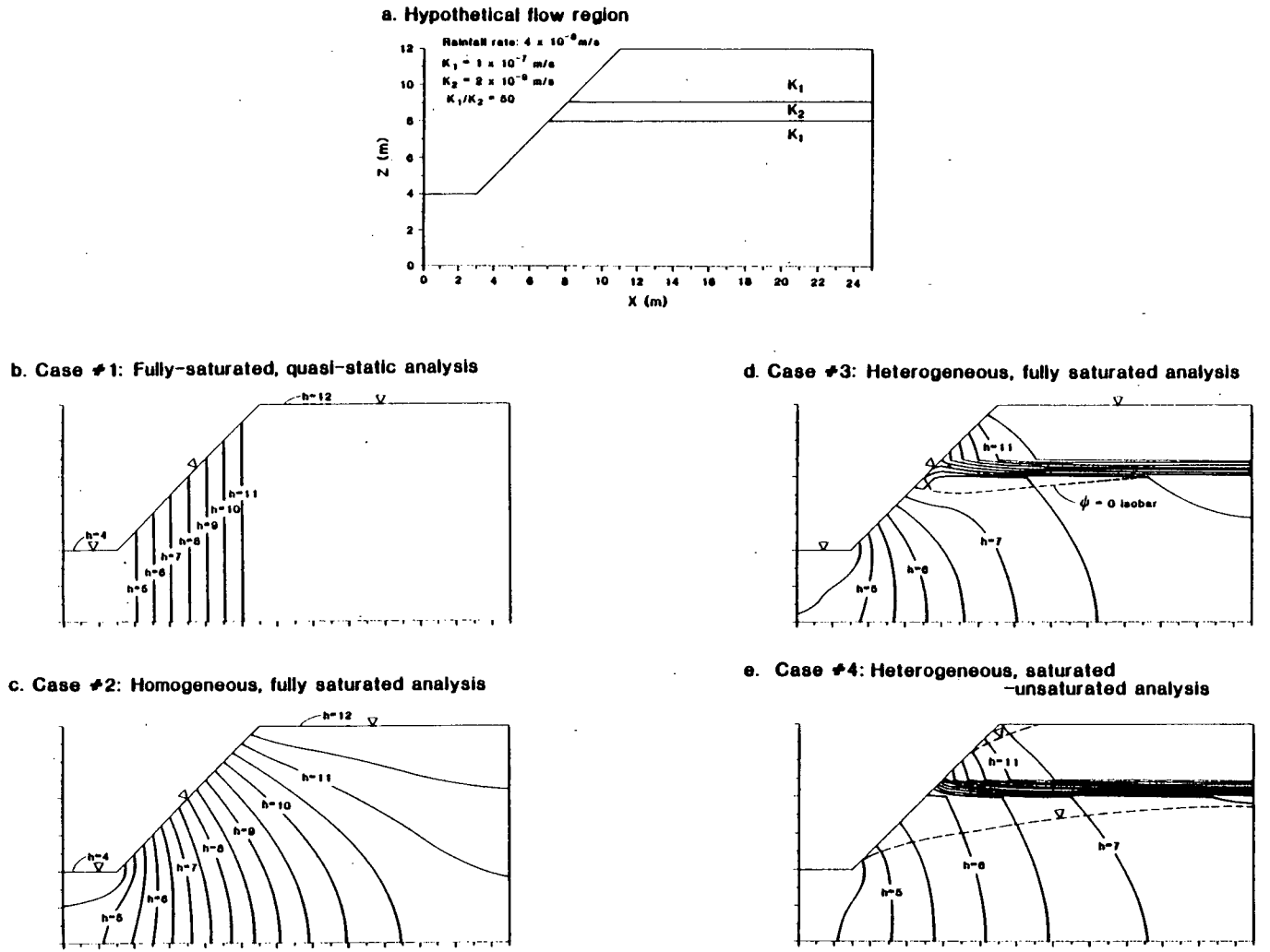

Figure 46. Possible hydraulic-head distributions for use in slope-stability analysis.

Case No. 1: In the absence of reliable data, it is common to assume that the region is fully saturated and the pressure head at any given point along a potential failure surface is equal to the vertical distance from that point to the soil surface. This assumption presumes the somewhat unrealistic hydraulic-head distribution shown in Figure 46b. It consists of vertical equipotential lines along the slope face and static conditions elsewhere.

Case No. 2: If the value of K_1 is known, and K_2 is not (or the existence of the K_2 layer is not recognized), it might be considered satisfactory to assume that the hillside is homogeneous and fully saturated. The hydraulic-head distribution shown in Figure 46c would then be appropriate for determining the fluid-pressure distribution along the potential failure surface.

Case No. 3: If both K_1 and K_2 are known, a fully saturated analysis of flow would yield a distribution of hydraulic-head like that shown in Figure 46d. Surprisingly, a calculation of the pressure heads for the simulated hydraulic-head pattern leads to the region of negative fluid pressure enclosed by the $\psi = 0$ isobar. Apparently, the finite-element program used in this study does not reject negative ψ-values even though it is a "fully-saturated" analysis. However, it must be recognized that they are not the correct values that would result from unsaturated flow theory. It is possible that many computer programs currently in circulation for the

prediction of saturated flow may exhibit this type of performance.

Case No. 4: If the data were available to run a saturated-unsaturated analysis, the hydraulic-head distribution shown in Figure 46e could be used in the slope stability analysis.

Figure 47 shows a comparison of the fluid-pressure distributions and pressure-head distributions along a potential failure surface for each of the hydraulic-head distributions shown in Figure 46. Case No. 4 is the most accurate estimate of the actual conditions. Case No. 1 provides the most conservative estimate of the fluid-pressure distribution and requires no hydrogeologic data. However, its use would lead to an overdesign of the slope angle; this may or may not be acceptable. In the case of the design of an open pit mine, the cost of an analysis like Case No. 4 might be justified in light of the savings created by reduced excavation. Case No. 2, in which the hillside is assumed to be homogeneous and fully saturated, leads to serious errors as the fluid pressure is underestimated above the impeding layer at measurement points 16 and 17. The shear strength, the factor of safety, and the stable slope angle would therefore be overestimated. Even greater error would be introduced by the homogeneous analysis if the water table was assumed to lie beneath the ground surface rather than coincident with it. Case No. 3 appears to predict the relatively high fluid pressures above the impeding layer quite well. It should be emphasized, however, that the

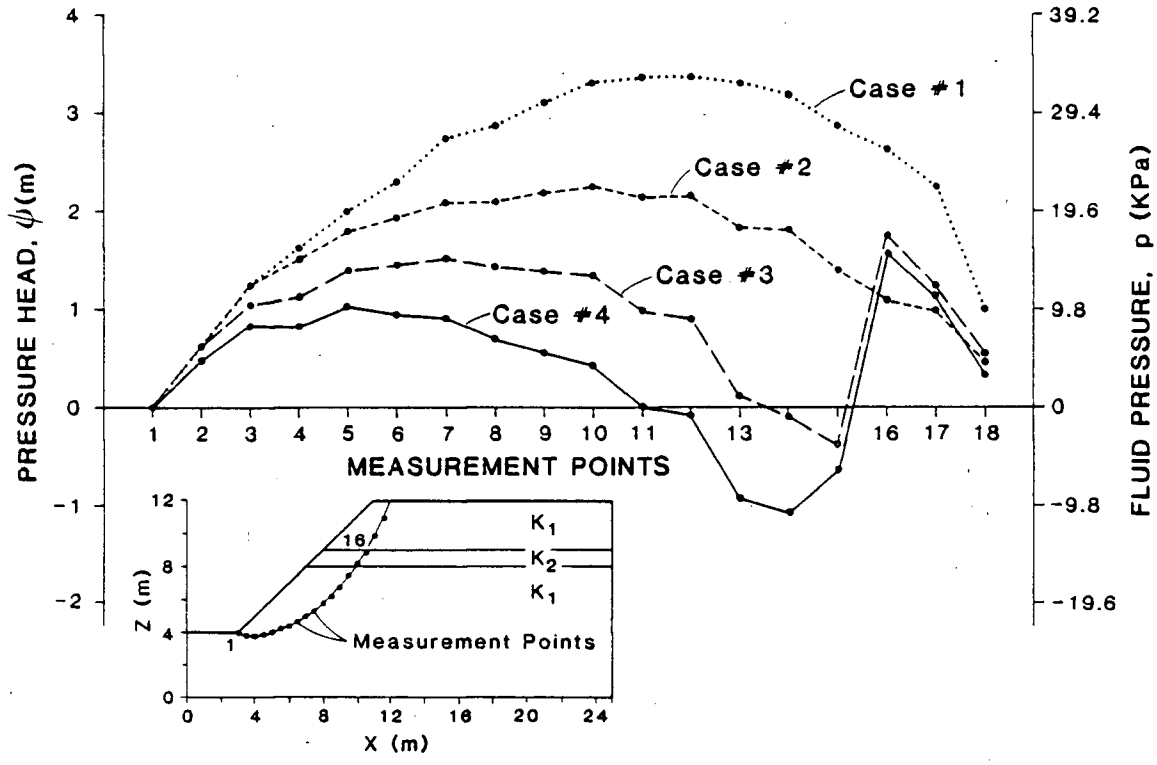

Figure 47. Comparison of pressure-head and fluid-pressure distributions along a potential failure surface.

use of a "fully-saturated" heterogeneous analysis which allows negative fluid pressures is physically incorrect and the approach cannot be recommended.

At least two case histories have been reported in which multiple seepage faces have been present and the associated saturated-unsaturated flow conditions have been taken into consideration during the stability analysis. In both examples, the fluid pressure was set equal to zero in the unsaturated zone for stability calculations. Sterrett and Edil (1982) investigated the stability of a 30m high, layered slope in Wisconsin along the Lake Michigan shoreline. Erosion of up to 10m/year had been observed near the top of the slope. Figure 48 shows the geology at the site and the water-table configuration inferred from field measurements of the pressure head and observation of the seepage face locations. From their stability analysis, they were able to conclude that the uppermost perched flow system was a significant factor in the bluff-top erosion. Eigenbrod and Morgenstern (1972) investigated a landslide that occurred along a highway cut in a river valley near Edmonton, Alberta. The slope had been cut into bedrock consisting of interbedded mudstone, claystone, sandstone, coal, and bentonitic clay. Failure had occurred along the base of a horizontal bentonite layer, 2 to 30 cm in thickness. Directly beneath the failure surface was a partially saturated coal layer. Field measurements revealed the presence of two perched water tables associated with seepage faces formed along the slope, as shown in Figure 49.

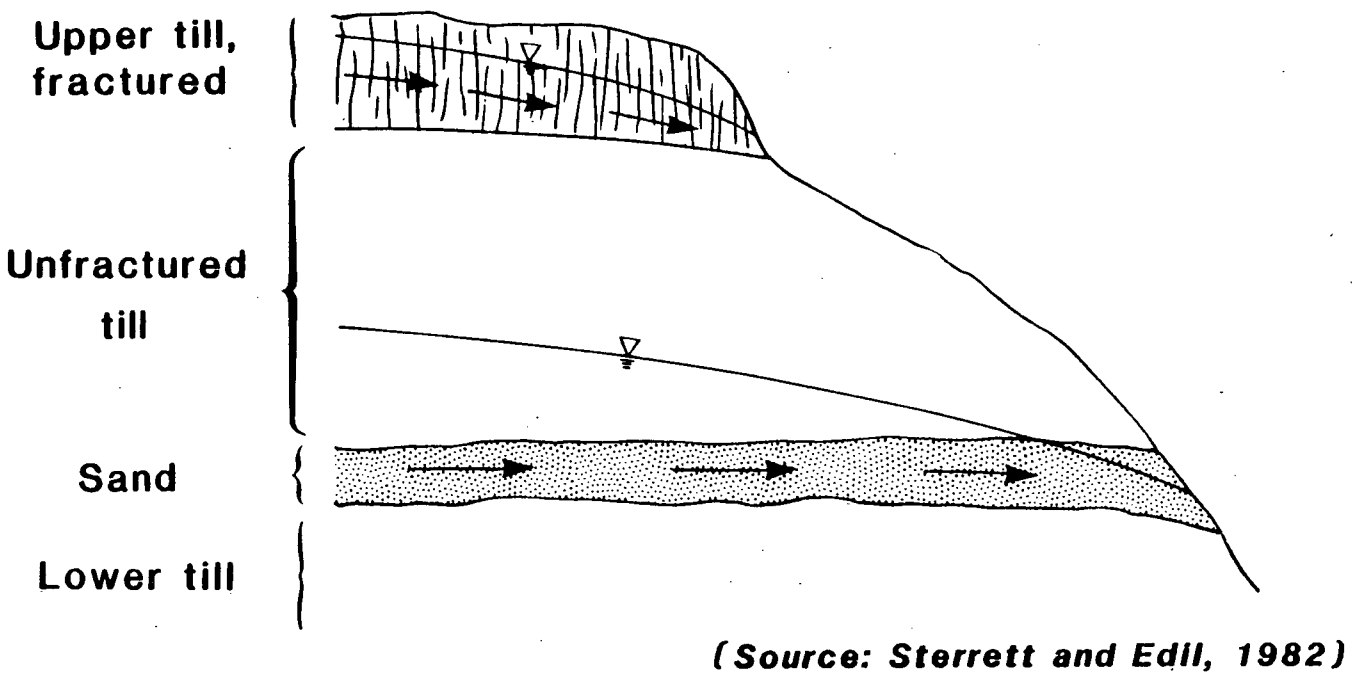

Figure 48. Geology and groundwater conditions at Bender Park site in Wisconsin.

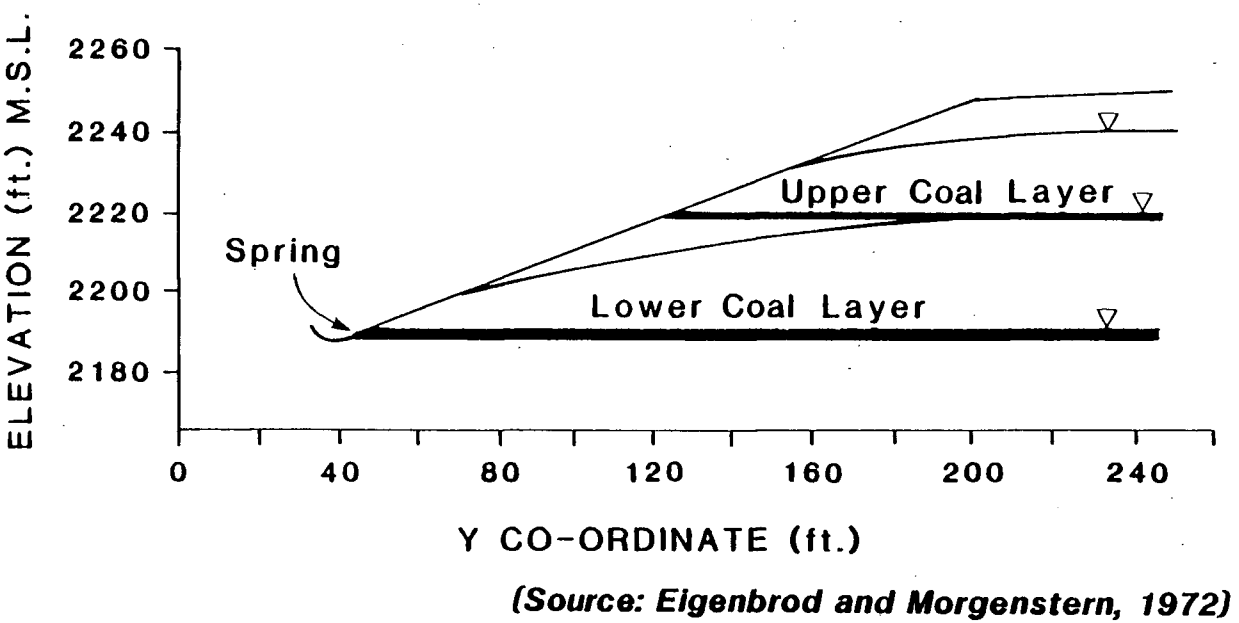

Figure 49. Groundwater conditions at a highway cut in Alberta.

Their stability analysis produced a factor of safety for the slope, prior to failure, of between .82 and 1.13. In both examples, the ability to make a consistent interpretation hinged on careful field observations and appreciation of the complex nature of the flow system present in layered hillsides.

6.2 Other Possible Applications

GROUNDWATER INFLOWS INTO EXCAVATIONS

Groundwater inflows occur when an excavation is taken below the water table. Freeze and Cherry (1979) present an overview of the drainage and dewatering systems that can be used to control groundwater inflows; Sharp et al. (1977) treat the subject in detail. Methods commonly used to lower the water table in the vicinity of an excavation include: a) installation of horizontal drains, b) construction of drainage galleries, and c) installation of a network of pumping wells. These methods are illustrated in Figure 50 for an excavation into homogeneous material.

The success of a dewatering scheme depends upon how well the groundwater flow system is understood. Consider the hypothetical excavation into layered material shown in Figure 51. It would be especially important to characterize the saturated-unsaturated nature of the flow system and to predict the transient response of the water table in a region such as this in order to make accurate estimates of inflow rates, and to provide an effective and efficient design for the drainage scheme. Such a design may include the location of pump intake

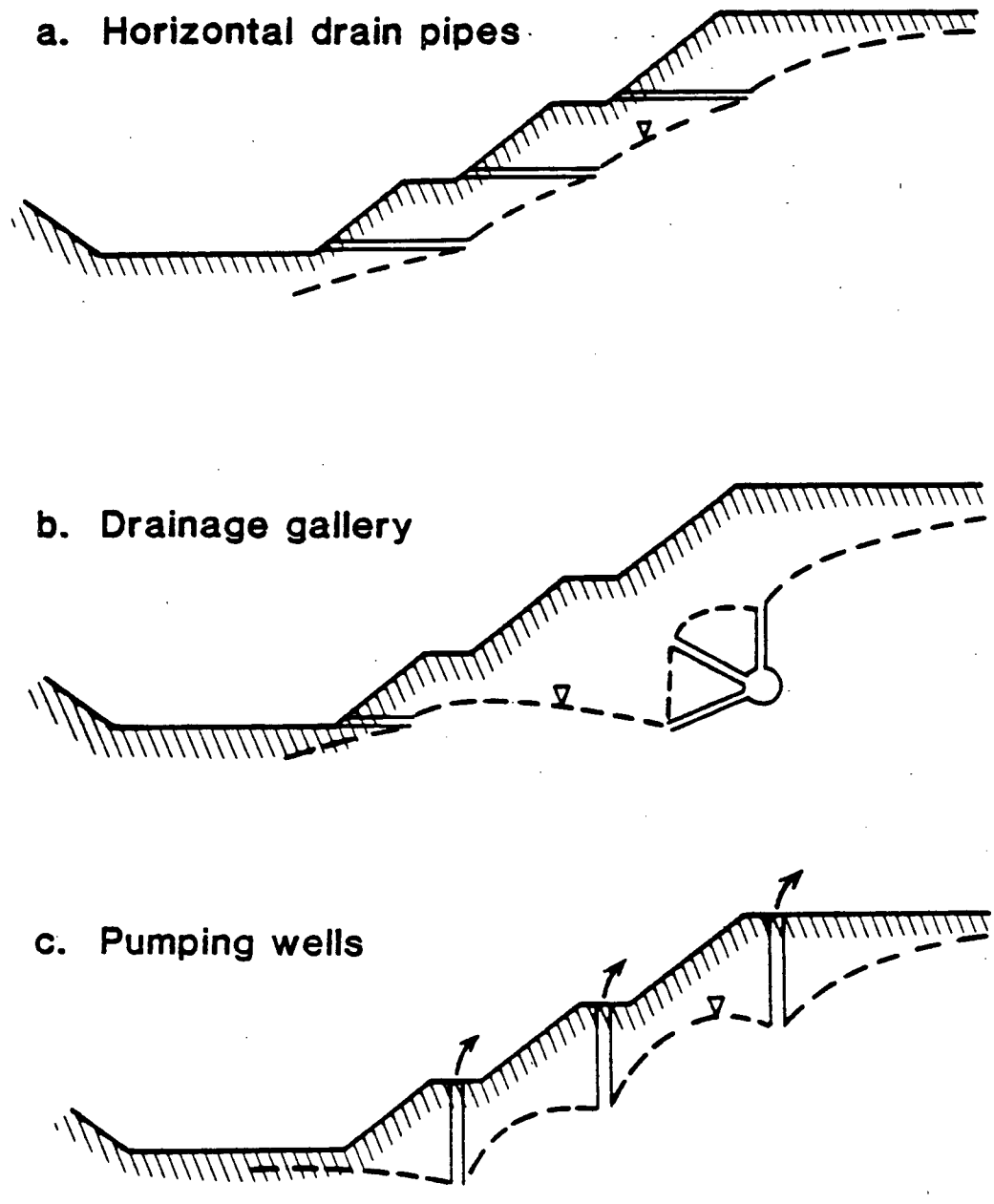

Figure 50. Methods used to control groundwater inflows into excavations.

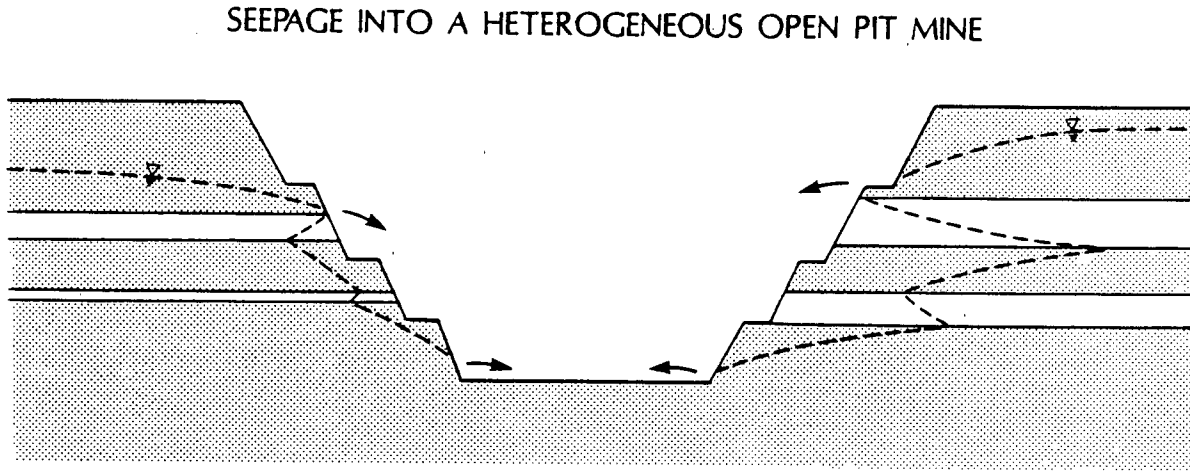

Figure 51. Hypothetical water-table configuration for an excavation into heterogeneous material.

points and their capacities, the positioning and sizing of drainage adits or galleries; and the specification of drainpipe location and length.

REGIONAL GROUNDWATER FLOW

In many groundwater studies, it is essential that the following attributes of the regional hydrogeology be determined: a) the boundaries of the regional flow system, b) the locations of recharge and discharge areas, and c) the magnitude and direction of groundwater flow throughout the region. These attributes are best determined when theoretical studies and field investigations are used in conjunction with one another. Theoretical studies, such as those provided by mathematical models, are valuable in the reconnaissance stage of an investigation. They can give the best estimate of the general flow patterms based on the data that are initially available and guide the investigator to those areas where further data collection would be the most useful. Newly acquired data can then be used to test and refine the theoretical analysis.

In order to obtain a consistent interpretation, however, the assumptions underlying the theoretical model must be met in the field. In most cases, it is sufficient to model steady-state saturated flow through a two-dimensional cross section oriented parallel to the dip of the water table. The classic studies of regional flow systems by Toth (1963) and Freeze and Witherspoon (1967), are based on these assumptions. The results contained in this thesis, however, suggest that in

order to identify the attributes of regions containing layered hillsides correctly, we cannot assume that the region is fully saturated; a saturated-unsaturated analysis must be performed. Figure 27 in Chapter 4 demonstrated that an unsaturated wedge may extend for several kilometers into a hillside if the hydraulic conductivity contrast exceeds three orders of magnitude. Recognition of the saturated-unsaturated nature of these systems could have important implications with respect to the assessment of regional groundwater resources and in the prediction of the movement of contaminants. In such studies, the data collection scheme should be designed to allow for the detection of perched flow systems. Sampling the pressure head at several different depths in each borehole might be an efficient and economical approach to field instrumentation in layered systems.

HILLSLOPE HYDROLOGY

A great deal of progress has been made by geomorphologists in describing the three-dimensional form of hillslopes and in understanding the geologic and hydrologic processes by which hillslopes evolve. Such information is used by geologists to reconstruct geologic history, by geotechnical engineers to correlate hillslope form with the strength of the underlying soil and rock mass, and by land-use planners to evaluate how hillslope processes might affect a siting of human activity.

Most descriptive models of slope development distinguish between the effects of mass movements and surface-water erosion. For example, Carson (1969) proposed a two-phase model

in which, initially, rapid mass movements reduce steep slopes to gentle slopes. In the second phase, surface-water erosion dominates slope development. Others suggest that mass movements control the upper, convex and straight segments of a hillslope profile and that surface-water erosion controls the lower, often concave, portion of the slope (Bloom, 1978). The models of slope development will not be reviewed in detail in this section; the interested reader is referred to Carson and Kirkby (1972), Young (1972), Kirkby (1978), Dunne and Leopold (1978), and Ritter (1978). Instead, the following discussion of mass movements and surface-water erosion is intended to indicate those areas where an understanding of the development of multiple seepage faces could be important to studies of slope devlopment.

Mass Movements

Mass movements refer to the processes by which sediment is transported downslope under a gravitational stress field. They are further subdivided into slow and rapid mass movements. Slow mass movements, or soil creep, may be the result of two processes. The first involves the plastic flow of clay-rich soils in wet climates. The second involves the movement of soil particles and soil aggregates due to swelling and settlement during freeze-thaw and wetting-drying cycles. The effectiveness of soil creep in transporting sediments downslope is a function of the hillslope gradient, the soil type, the water content of the soil, and the climate. The groundwater

conditions that give rise to multiple seepage faces would be expected to promote localized areas of accelerated soil creep.

Rapid mass movements are collectively termed landslides. Depending on the nature of the material which failed and on the style of movement, landslides are classified as either falls, slides, or flows. Regardless of the precise classification, the generation of most rapid mass movements is controlled to a large extent by the fluid-pressure distribution within the hillslope. In essence, the study of rapid mass movements reduces to the study of slope stability, discussed in Section 6.1. The work presented in this thesis should be of interest, therefore, to those geomorphologists studying the role of mass movements in the development of slopes in layered geologic environments.

Surface-Water Erosion

Surface-water erosion refers to the entrainment and transport of soil particles downslope by surface water. This can only occur if hydrogeologic factors combine to produce runoff. The mechanisms by which runoff is generated are summarized by Dunne (1978). They will be outlined here with reference to four flow paths water might follow as it moves downhill; these pathways are shown in Figure 52 for a homogeneous hillside.

If the rainfall rate exceeds the infiltrability of the soil and the rainfall duration exceeds the time required for the soil surface to become saturated, then a portion of the rainfall will runoff and follow Path No. 1 as Horton overland

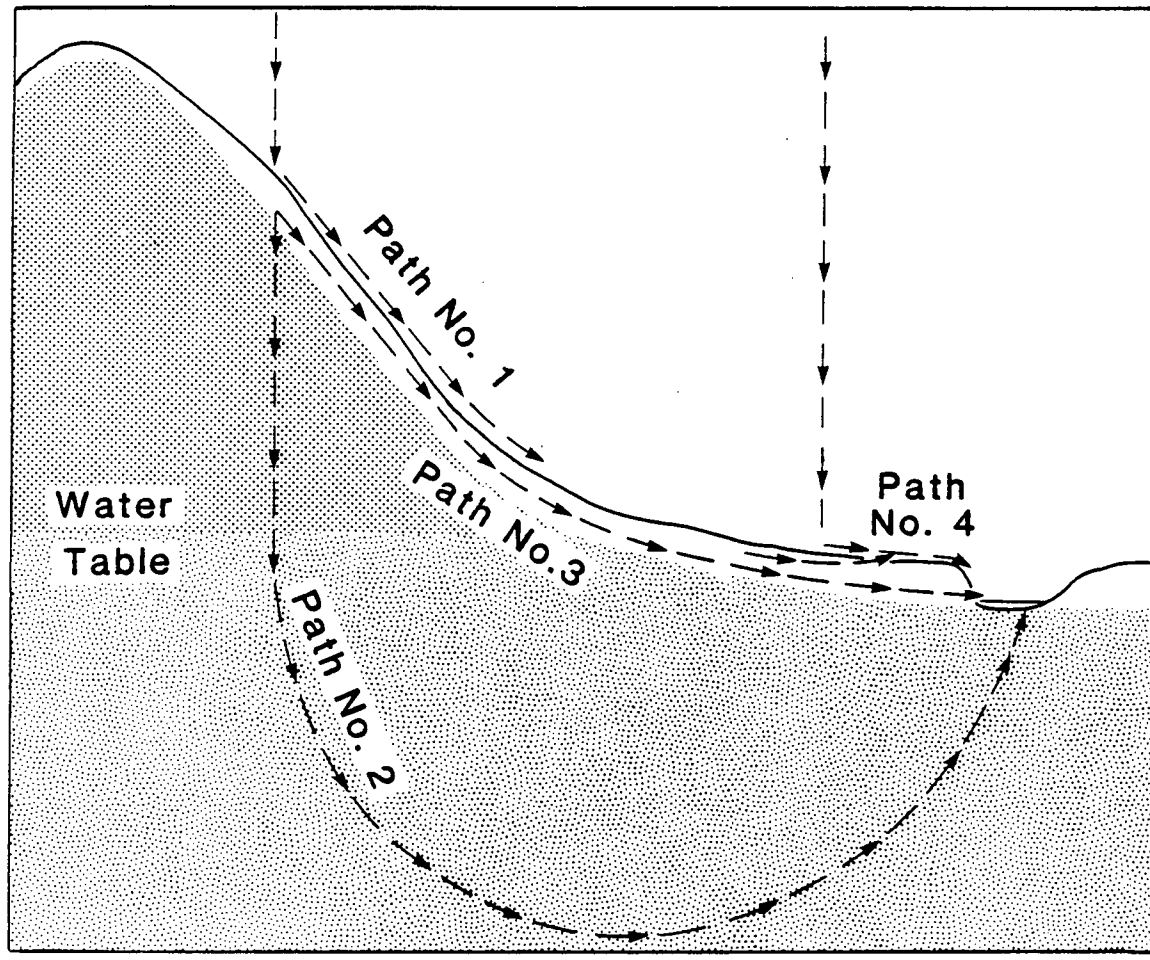

(Source: Dunne, 1978)

Figure 52. Possible flow paths for water to follow for a homogeneous hillside.

flow. Some of the water that infiltrates may enter the groundwater flow system and follow Path No. 2 to the stream channel. If there is a layer of permeable topsoil overlying the less permeable substrate, a portion of the rainfall that infiltrates may travel along Path No. 3 as subsurface stormflow. And finally, if during a storm the water table rises and intersects the soil surface, then a seepage face will form. The runoff produced at the seepage face is termed saturation overland flow and is labeled as Path No. 4 in Figure 52. Saturation overland flow includes water generated from a) the emergence of subsurface stormflow, b) direct precipitation onto the saturated soil surface, and c) groundwater discharge. Note that for a homogeneous hillside, saturation overland flow is most likely to occur near the stream channel where the water table is relatively close to the soil surface. For layered slopes, the results presented in this thesis demonstrate that multiple seepage faces could produce additional areas of saturation overland flow, possibly quite far from the stream channel. Understanding the occurrence of multiple seepage faces is therefore relevant to studies of surface-water erosion.

In addition to mass movements and surface-water erosion, groundwater conditions within a hillside can exert a strong influence on the location of stream heads within a watershed. The initiation and headward erosion of tributary streams can be the direct result of a form of subsurface erosion known as piping. As water flows through the pore spaces of a soil,

energy is transferred from the water to the soil particles in the form of a frictional drag. The force associated with this energy transfer, as reflected by the hydraulic gradient, may be sufficient to erode soil particles at the exit point of the subsurface flow path. This erosive process is termed piping. Prediction of the location of seepage faces is therefore basic to understanding the location of areas where piping may occur. It is possible that the two-dimensional analysis presented in this thesis could aid the study of the three-dimensional development of drainage networks in layered, heterogeneous regions.

Chapter 7

SUMMARY AND CONCLUSIONS

The work and conclusions contained in this thesis will be summarized in terms of the four objectives of the research.

The first objective was to select a finite-element model to predict the fluid-pressure distribution and seepage-face locations in layered, heterogeneous hillsides. The finite-element model that was chosen for the study was written by Shlomo Neuman at the University of Arizona. The program was originally titled UNSAT I and is fully documented in Neuman (1972). In its original form, UNSAT I can model transient, two-dimensional, saturated-unsaturated flow through heterogeneous, anisotropic flow regions. UNSAT I was modified for use in this thesis in three ways. First, a steady-state version of the program was created. Second, the treatment of the seepage-face boundary was modified to allow the generalized development of more than one seepage face along a given slope. Third, the numerical treatment of the infiltration process was modified so that the flux entering the system would be determined iteratively in response to the hydraulic-head distribution. With these modifications, the fluid-pressure distribution and seepage-face locations in layered slopes could be studied in either a steady-state or transient mode.

The second objective was to build a laboratory model to verify the physical foundation of the solutions generated by the numerical model; the test met with success. A sand-tank

model was built to represent a hillside containing one impeding layer and two seepage faces. The steady-state response of the flow region to three different rainfall rates was recorded. The numerical model was calibrated against the response of the physical model to the first rainfall rate and verified by its ability to simulate the subsequent response to the two other rainfall rates. The physical model confirmed the existence of a wedge-shaped unsaturated zone separating the two seepage faces and confirmed that the water table responded to changes in the rainfall rate in a manner predicted by the numerical model.

The third objective of this research was to use the numerical model in sensitivity studies designed to reach quantitative conclusions about the factors governing the development of multiple seepage faces. This objective was met by using a detailed steady-state analysis and two preliminary transient simulations. In all simulations, the hydraulic conductivity of the K_2 layer was less than the hydraulic conductivity of the material comprising the remainder of the hillside, K_1. In addition, the impeding layers were horizontal, of uniform thickness, and of uniform hydraulic properties.

The assumptions and limitations of the theoretical analysis are listed below. Following each is an indication of whether the item applies to both the steady-state and transient analysis, or to just the transient analysis:

1. Flow is two-dimensional. (both)
2. Darcy's law is valid. (both)
3. The air phase is continuous and at atmospheric pressure. (both)
4. The unsaturated hydraulic properties are nonhysteretic. (transient)
5. Evapotranspiration is not modeled. (both)
6. The $K(\psi)$ curves are scaled in accordance with Equation 4.2. (both)
7. The porous medium is compressible; the individual soil grains are not. (transient)
8. The porous medium is linearly and reversibly elastic. (transient)
9. The total stress is constant and acts in the vertical direction only. (transient)
10. The specific storage remains constant, regardless of the degree of saturation. (transient)
11. There is no infiltration along the seepage-face boundary. (both)
12. The fate of surface runoff is not modeled. (both)
13. A numerical solution may not be possible where steep gradients in pressure head and hydraulic conductivity develop within the unsaturated zone. (both)
14. Interactions between the subsurface flow system and the stream level are not modeled. (transient)

Of the assumptions related to the steady-state analysis, No. 1 and No. 9 were considered to be the most important, particularly if one were to extrapolate the results to the occurrence of multiple seepage faces on gentle slopes. Limitation No. 11 restricted the study to relatively wet conditions. The assumptions and limitations pertaining to the transient analysis cannot be evaluated as a full transient sensitivity study was not performed.

The conclusions from the steady-state analysis of one-layer systems are as follows:

1. If all else is constant, then for a given K_1/K_2 ratio, an increase in the elevation of the impeding layer:
   a) increases the extent of the unsaturated wedge, and
   b) decreases the percentage of the total outflow across the uppermost seepage face.
2. If all else is constant, then for a given position of the impeding layer, an increase in the K_1/K_2 ratio:
   a) increases the extent of the unsaturated wedge, and
   b) increases the percentage of the total outflow across the uppermost seepage face.
3. For the flow system modeled, K_1/K_2 ratios greater than three orders of magnitude produced an unsaturated wedge that extended more than 1000m into the hillside.
4. For a given hydraulic conductivity contrast measured in the z-direction, the water-table configuration is insensitive to anisotropy within the impeding layer.

However, it is sensitive to anisotropy within the material surrounding the impeding layer. If all else is constant, and if the properties of the material surrounding the impeding layer are such that $K_x > K_z$, then the extent of the unsaturated wedge is increased relative to isotropic conditions.

Conversely, if $K_z > K_x$, then the unsaturated wedge is much less extensive.

5. If all else is constant, then a greater hydraulic conductivity contrast is required to produce multiple seepage faces on gentle slopes as compared to steep slopes. In the example presented in Chapter 4, a hydraulic conductivity contrast of at least two orders of magnitude was required to produce multiple seepage faces on an 8^{o} slope, while one order of magnitude was sufficient to produce multiple seepage faces on a 40^{o} slope.

The conclusions from the steady-state analysis of two-layer systems are as follows:

1. For a given K_1/K_2 ratio, and a given distance separating the impeding layers, an increase in the elevation of the layers: a) increases the extent of both unsaturated wedges, and b) decreases the percentage of the total outflow from the uppermost seepage face, %Qu, as well as the percentage from the middle seepage face, %Qm.

2. Regardless of the distance separating the impeding layers, an increase in the K_1/K_2 ratio: a) increases the extent of both unsaturated wedges, and b) increases %Qu. The value of %Qm remains relatively unchanged until the K_1/K_2 ratio is increased above 100, after which %Qm decreases.
3. In general, the unsaturated wedge beneath the lower impeding layer is less extensive than the unsaturated wedge formed beneath the upper impeding layer.
4. If the position of the upper impeding layer remains fixed, then as the second layer is placed at successively lower elevations, %Qu decreases and %Qm increases. Conversely, if the position of the lower impeding layer remains fixed, then as the upper layer is placed at successively lower positions, %Qu increases and %Qm decreases.

Extension of the steady-state analysis to three-layer systems primarily served to confirm many of the conclusions from one- and two-layer systems and to demonstrate the complexity that can result as the number of impeding layers is increased. The three-layer systems did show, however, that if all else is constant, then as the number of impeding layers within a hillside is increased, the unsaturated wedges become less extensive.

The limited number of transient runs precludes a detailed set of conclusions at this time.

The fourth, and final, objective of this thesis was to form generalized conclusions regarding the importance of multiple seepage faces in geotechnical, hydrogeological, and geomorphological problems. With regard to geotechnical problems, this study has implications with respect to predictions of the fluid-pressure distribution for slope-stability analyses and predictions of groundwater inflows into excavations. In both instances, it can be concluded that predictions based on homogeneous and saturated analyses may be significantly in error when applied to layered slopes. With regard to hydrogeological problems, it has been suggested that because an unsaturated wedge can extend for great distances into a hillside, a saturated-unsaturated analysis should be considered in studies designed to identify the attributes of regional flow systems containing layered slopes. In addition, a versatile data collection scheme is necessary for such studies in order to allow for the detection of perched flow systems. Recognition of the saturated-unsaturated nature of these systems can be important in the assessment of regional groundwater resources and in the prediction of contaminant transport. With regard to geomorphological problems, ground water conditions within a layered slope can exert a strong influence on: a) the occurrence of mass movements, b) the generation of surface-water erosion, and c) the process of piping and the location of stream heads.

BIBLIOGRAPHY

Barry, R.G., and R.J. Chorley, Atmosphere, Weather, and Climate, 3rd Ed., Methuen and Company, London, 432 pp., 1976.

Bathe, K.J., and E.L. Wilson, Numerical Methods in Finite Element Analysis, Prentice-Hall, New Jersey, 1976.

Bear, J., Dynamics of Fluids in Porous Media, American Elsevier, New York, 764 pp., 1972.

Bishop, A.W., and G.E. Blight, Some aspects of effective stress in saturated and partially saturated soils, Geotechnique, 13, 177-197, 1963.

Bloom, A.L., Geomorphology: A Systematic Analysis of Late Genezoic Landforms, Prentice-Hall, New Jersey, 510 pp., 1978.

Carson, M.A., Models of hillslope development under mass failure, Geographical Analysis, 1, 76-100, 1969.

Carson, M.A., and M.J. Kirkby, Hillslope Form and Process, Cambridge University Press, 475 pp., 1972.

Childs, E.C., and N. Collis-George, The permeability of porous materials, Roy. Soc. (London), Proc., A.201, 392-405, 1950.

Chow, V.T., and T.E. Harbough, Raindrop production for laboratory watershed experimentation, Jour. of Geophys. Res., 70 (24), 6111-6119, 1965.

Cooley, R.L., Some new procedures for numerical simulation of variably saturated flow problems, Water Resour. Res., 19(5), 1271-1285, 1983.

Cooper, H.H., Jr., The equation of groundwater flow in fixed and deforming coordinates, Jour. Geophys. Res., 71, 4785-4790, 1966.

Craig, R.F., Soil Mechanics, 2nd Edition, Van Nostrand Reinhold, New York, 318 pp., 1978.

Deere, D.U., and F.D. Patton, Stability of Slopes in residual soils, Proc. 4th Pan Amer. Conf. on Soil Mech. and Found. Eng., San Juan, Puerto Rico, 87-170, 1971.

Dunne, T., Field studies of hillslope flow processes, Chapter 7 in Hillslope Hydrology (M.J. Kirkby, ed.), John Wiley and Sons, 227-293, 1978.

Dunne, T., and L.B. Leopold, Water in Environmental Planning, W.H. Freeman, 818 pp., 1978.

Eigenbrod, K.D., and N.R. Morgenstern, A slide in Cretaceous bedrock at Devon, Alberta, in Geotechnical Practice for Stability in Open Pit Mining (C.O. Brawner and V. Milligan, eds.), Soc. of Mining Eng., Am. Inst. of Mining, Metallurgical and Petroleum Eng., New York, 233-238, 1972.

Freeze, R.A., Three-dimensional, transient, saturated-unsaturated flow in a groundwater basin, Water Resour. Res., 7, 347-366, 1971.

Freeze, R.A., Mathematical models of hillslope hydrology, in Hillslope Hydrology (M.J. Kirkby, ed.) John Wiley and Sons, 177-225, 1978.

Freeze, R.A., and J. Banner, The mechanism of natural groundwater recharge and discharge: 2. Laboratory column experiments and field measurements, Water Resour. Res., 6, 138-155, 1970.

Freeze, R.A., and J.A. Cherry, Groundwater, Prentice Hall, New Jersey, 604 pp., 1979.

Fredlund, D.G., Second Canadian Geotechnical Colluquium: Appropriate concepts and technology for unsaturated soils, Can. Geotech. Jour., 16, 121-139, 1979.

Fredlund, D.G., Morgenstern, N.R., and R.A. Widger, The shear strength of unsaturated soils, Can. Geotech. Jour., 15, 313-321, 1978.

Gardner, W.R., Mathematics of isothermal water conduction in unsaturated soils, Highway Res. Board, Res. Council Rept. No. 4, 78-87, 1959.

Hillel, D., Fundamentals of Soil Physics, Academic Press, New York, 413 pp., 1980.

Hodge, R.A.L., and R.A. Freeze, Groundwater flow systems and slope stability, Can. Geotech. Jour., 14, 466-476, 1977.

Hubbert, M.K., Theory of scale models as applied to the study of geologic structures, Bull, Geol. Soc. Amer., 48, 1459-1520, 1937.

Jacob, C.E., The flow of water in an elastic artesian aquifer, Trans. Amer. Geophys. Union, part 2, 574-586, 1940.

Kirkby, M.J., editor, Hillslope Hydrology, John Wiley and Sons, 389 pp., 1978.

Kline, S.J., Similitude and Approximation Theory, McGraw-Hill, New York, 229 pp., 1965.

Klute, A., The determination of the hydraulic conductivity and diffusivity of unsaturated soils, Soil Sci., 113, 264-276, 1972.

Lambe, T.W., Soil Testing for Engineers, John Wiley and Sons, 165 pp., 1951.

Moore, F.E., Water conduction from shallow water tables, Hilgardia, 12, 383-424, 1939.

Morgenstern, N.R., and V.E. Price, The analysis of the stability of general slip surfaces, Geotechnique, 15, 79-93, 1965.

Mualem, Y., A catelogue of the hydraulic properties of unsaturated soils, Res. Proj. 442, Technion Israel Institute of Technology, Haifa, Israel, 100 pp., 1976.

Neuman, S.P., Finite element computer programs for flow in saturated-unsaturated porous media, Second Annual Report, Proj. No. A10-SWC-77, Techion Israel Institute of Technology, Haifa, Israel, 87 pp., 1972.

Neuman, S.P., Saturated-unsaturated seepage by finite elements, Jour. Hyd. Div., ASCE, 99, 2233-2250, 1973.

Neuman, S.P., Feddes; R.A, and E. Bresler, Finite element simulation of flow in saturated-unsaturated soils considering water uptake by plants, Third Annual Rept., Part 1, Proj. No. A10-SWC-77, Technion Israel Institute of Technology, Haifa, Israel, 104 pp., 1974.

Neuman, S.P., Feddes, R.A., and E. Bresler, Finite element analysis of two-dimensional flow in soils considering water uptake by roots: 1. Theory, Soil. Sci. Soc. Amer. Proc., 39, 224-230, 1975.

Nieber, J.L., and M.F. Walter, Two-dimensional soil moisture flow in a sloping rectangular region: Experimental and numerical studies, Water Resour. Res., 17, 1722-1730, 1981.

Patton, F.D., and D.U. Deere, Geologic factors controlling slope stability in open pit mines, in Stability in Open Pit Mining (C.O. Brawner and V. Milligan, eds.), Soc. of Mining Eng., Am. Institute of Mining, Metallurgical and Petroleum Eng., New York 23-47, 1971.

Patton, F.D., and A.J. Hendron, Jr., General report on mass movements, Proc. 2nd International Congr., International Assoc. Eng. Geol., Sao Paulo, Brazil, vol 2, pp. V-GR.1 - V-GR.57, 1974.

Pinder, G.F., and W.G. Gray, Finite Element Simulation in Surface and Subsurface Hydrology, Academic Press, New York, 295 pp., 1977.

Richards, L.A., Capillary conduction of liquids through porous mediums, Physics, 1, 318-333, 1931.

Ritter, D.F., Process Geomorphology, W.C. Brown, 603 pp., 1978.

Rubin, J., Theoretical analysis of two-dimensional, transient flow of water in unsaturated and partially unsaturated soils, Soil Sci. Soc. Amer. Proc., 32, 607-615, 1968.

Sharp, J.C., Ley, G.M.M., and R. Sage, Pit Slope Manual Chapter 4 - Groundwater, Canada Centre for Mineral and Energy Technology, CANMET Report 77-13, 204 pp., 1977.

Stephenson, G.R., and R.A. Freeze, Mathematical simulation of subsurface flow contributions to snowmelt runoff, Reynolds Creek Watershed, Idaho, Water Resour. Res., 10, 284-294, 1974.

Sterrett, R.J., and T.B. Edil, Ground-water flow systems and stability of a slope, Ground Water, 20, 5-11, 1982.

Toth, J., A theory of groundwater motion in small drainage basins in Central Alberta, Canada, Jour. Geophys. Res., 67, 4375-4387, 1962.

Toth, J., A theoretical analysis of groundwater flow in small drainage basins, Jour. Geophys. Res., 68, 4795-4812, 1963.

Verma, R.D., and W. Brutsaert, Unconfined aquifer seepage by capillary flow theory, Jour. Hyd. Div., ASCE, 96, 1331-1344, 1970.

Verma, R.D., and W. Brutsaert, Similitude criteria for flow from unconfied aquifers, Jour. Hyd. Div., ASCE, 97, 1493-1509, 1971.

Wang, H.F., and M.P. Anderson, Introduction to Groundwater Modeling - Finite Difference and Finite Element Methods, W.H. Freeman and Co, San Francisco, 237 pp., 1982.

Young, A., Slopes, Oliver and Boyd, 288 pp., 1972.

Young, D.H., Statistical Treatment of Experimental Data, McGraw-Hill, New York, 172 pp., 1962.

Zienkiewicz, O.C., The Finite Element Method, 3rd Ed., McGraw-Hill, New York, 787 pp., 1977.

APPENDIX A

DEFINITION OF SYMBOLS

Symbol	Definition
A	cross-sectional area, $[L^2]$
[A]	global stiffness matrix
C	specific moisture capacity, [1/L]
[F]	capacitance matrix
ID	inside diameter
K	hydraulic conductivity, [L/T]
K_r	relative hydraulic conductivity
K_s	saturated hydraulic conductivity [L/T]
OD	outside diameter
Q	volumetric flow rate, $[L^3/T]$
$\bar{Q}$	outflow volume, $[L^3]$
R	rainfall rate, [L/T]
S	shear strength $[ML^{-1}T^{-2}]$
SC	seepage collector
S_s	specific storage, [1/L]
T	thickness of impeding layer, [L]
V	flow region
$\bar{c}$	effective cohesion, $[ML^{-1}T^{-2}]$
cm	centimeter
g	gravitational acceleration, $[L/T^2]$
h	hydraulic head, [L]
k	permeability, $[L^2]$
l	length of soil sample, [L]

m	meter
n	porosity, $[L^3/L^3]$
p	gage fluid pressure, $[MT^{-2}L^{-1}]$
t	time, [T]
v	specific discharge, [L/T]
$w(x,z)$	weighting function, [L]
x	horizontal coordinate direction, [L]
z	vertical coordinate direction, [L]
$\bar{z}$	elevation of the base of the impeding layer, [L]
z_s	depth of water overlying stream bed, [L]
α	compressibility of the porous medium, $[LT^2/M]$
β	compressibility of water, $[LT^2/M]$
$\delta_n(x,z)$	basis functions, [L]
Δh	constant-head differential, [L]
μ	dynamic viscosity, $[ML^{-1}T^{-1}]$
μ_a	air pressure in the pore spaces, $[MT^{-2}L^{-1}]$
μ_w	water pressure, $[MT^{-2}L^{-1}]$
ψ	pressure head, [L]
ψ_a	air entry value, [L]
$\hat{\psi}(x,z,t)$	approximate function, [L]
$\psi_n(t)$	exact solution, [L]
ρ	fluid density, $[M/L^3]$
ρ_b	dry bulk density, $[M/L^3]$
ρ_p	particle density, $[M/L^3]$
σ	total stress, $[ML^{-1}L^{-2}]$
σ_a	standard deviation of the measured quantity a
σ_a^2	variance of the measured quantity a

θ	volumetric water content, $[L^3/L^3]$
$\overline{\phi}$	effective angle of internal friction
χ	empirical soil strength paramter

APPENDIX B

EXPERIMENTAL DATA

In this appendix, the experimental data from the final run are given. Figure 53 shows the finite-element discretization of the experimental flow region and the location of the nodal points, or ports, at which data were collected. Port #1 was used for caliboration and is therefore not shown. Note that 46 of the ports contained tensiometers connected to the Scanivale; the measured and predicted hydraulic-head values for these are presented in Table 9. The remaining 10 ports shown in Figure 53 contained tensiometers connected to manometers; the corresponding measured and predicted hydraulic-head values are given in Table 10. The evaluation head and pressure head data are presented in Table 11 and Table 12. The predicted elevation head data can be obtained from Figure 53; The predicted pressure head data can be calculated from the predicted hydraulic head and elevation head data.

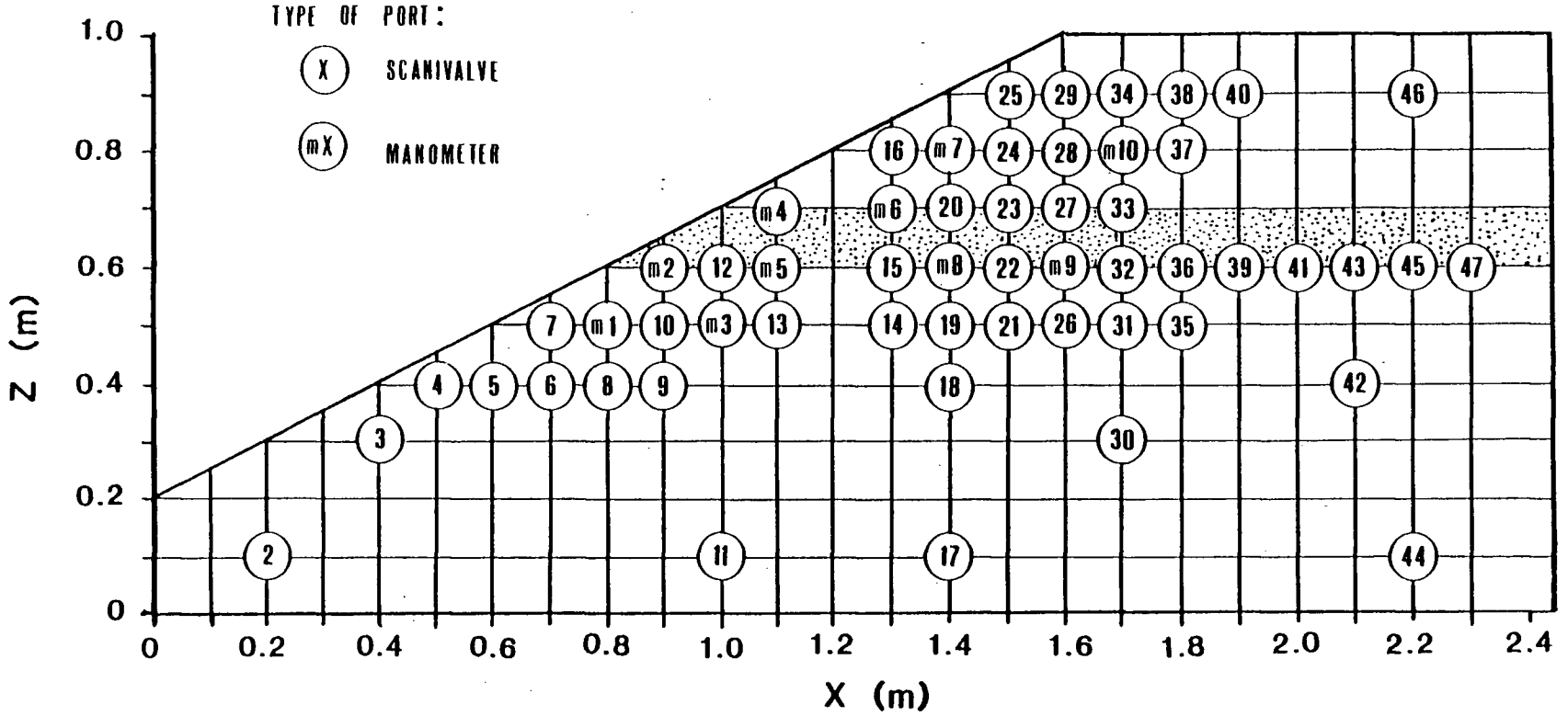

Figure 53. Index for tensiometer locations in the experimental flow region.

Table 9. Comparison of hydraulic-head data for tensiometers read with the Scanivalve.

h_m = measured hydraulic head; h_p = predicted hydraulic head (all values in cm)

	RUN #1			RUN #2			RUN #3		
PORT	h_m	h_p	h_m-h_p	h_m	h_p	h_m-h_p	h_m	h_p	h_m-h_p
2	44.5	34.0	10.5	43.8	34.0	9.8	43.5	33.9	9.6
3	38.5	39.1	-.6	39.1	39.0	0.1	39.4	38.7	0.7
4	40.4	43.2	-2.8	40.1	43.1	-3.0	40.1	42.6	-2.5
5	43.0	45.9	-2.9	42.0	45.7	-3.7	41.2	45.0	-3.8
6	52.0	48.3	3.7	49.9	48.0	1.9	49.4	47.1	2.3
7	47.0	49.0	-2.0	47.9	48.8	-0.9	45.6	47.8	-2.2
8	50.9	50.5	0.4	49.7	50.2	-0.5	49.0	49.1	-0.1
9	52.5	52.6	-0.1	51.6	52.3	-0.7	50.9	51.1	-0.2
10	53.1	53.0	0.1	52.2	52.7	-0.5	51.2	51.5	-0.3
11	53.7	53.8	-0.1	52.6	53.5	-0.9	51.5	52.1	-0.6
12	56.5	55.6	0.9	54.1	55.2	-1.1	53.7	53.9	-0.2
13	57.6	57.2	0.4	56.2	56.8	-0.6	54.1	55.3	-1.2
14	61.1	61.0	0.1	59.4	60.5	-1.1	56.1	58.6	-2.5
15	62.3	61.7	0.6	60.6	61.2	-0.6	57.1	59.3	-2.2
16	81.8	82.4	-0.6	79.0	81.5	-2.5	76.2	78.5	-2.3
17	61.2	61.1	0.1	59.4	60.6	-1.2	57.4	58.7	-1.3
18	62.0	62.1	-0.1	60.2	61.6	-1.4	58.2	59.6	-1.4
19	62.6	62.7	-0.1	60.7	62.2	-1.5	58.6	60.1	-1.5
20	85.7	84.0	1.7	81.6	82.9	-1.3	78.3	79.5	-1.2
21	63.9	64.3	-0.4	61.9	63.7	-1.8	59.7	61.5	-1.8
22	65.5	65.0	0.5	63.3	64.5	-1.2	61.0	62.2	-1.2
23	88.6	86.4	2.2	83.6	85.1	-1.5	79.8	81.2	-1.4
24	89.8	87.3	2.5	84.4	86.0	-1.6	80.5	82.0	-1.5
25	91.4	88.4	3.0	85.3	87.0	-1.7	81.3	82.8	-1.5
26	65.2	65.7	-0.5	63.0	65.1	-2.1	60.6	62.7	-2.1
27	91.3	88.6	2.7	85.5	87.2	-1.7	81.4	82.9	-1.5
28	92.5	89.5	3.0	86.4	88.1	-1.7	82.2	83.7	-1.5
29	94.4	90.6	3.8	87.3	89.1	-1.8	83.1	84.5	-1.4
30	65.3	65.8	-0.5	63.1	65.2	-2.1	60.9	62.8	-1.9
31	66.5	67.0	-0.5	64.1	66.4	-2.3	61.7	63.8	-2.1
32	67.2	67.8	-0.6	64.4	67.1	-2.7	63.0	64.6	-1.6
33	93.7	90.6	3.1	87.5	89.1	-1.6	83.1	84.4	-1.3
34	97.1	92.9	4.2	89.8	91.2	-1.4	85.1	86.3	-1.2
35	67.6	68.1	-0.5	65.1	67.5	-2.4	62.6	64.8	-2.2
36	69.1	69.0	0.1	66.4	68.3	-1.9	63.7	65.6	-1.9
37	96.6	93.5	3.1	90.4	91.8	-1.4	85.4	86.8	-1.4
38	98.5	94.5	4.0	91.7	93.1	-1.4	86.7	87.9	-1.2
39	70.6	70.0	0.6	68.0	69.2	-1.2	65.2	66.4	-1.2
40	99.2	96.4	2.8	93.0	94.7	-1.7	87.9	89.2	-1.3
41	70.7	70.7	0.0	67.9	70.0	-2.1	65.1	67.1	-2.0
42	69.3	69.8	-0.5	66.7	69.1	-2.4	64.0	66.3	-2.3
43	71.2	71.4	-0.2	68.3	70.7	-2.4	65.5	67.7	-2.2
44	68.6	69.1	-0.5	66.1	68.4	-2.3	63.5	65.7	-2.2
45	72.0	71.8	0.2	69.3	71.2	-1.9	66.2	68.1	-1.9
46	100.2	98.6	1.6	95.4	97.7	-2.3	89.9	91.8	-1.9
47	72.2	72.2	0.0	69.3	71.5	-2.2	66.3	68.4	-2.1

Table 10. Comparison of data for tensiometers read with manometers.

h_m = measured hydraulic head;
h_p = predicted hydraulic head (all values in cm)

	RUN #1			RUN #2			RUN #3		
PORT	h_m	h_p	h_m-h_p	h_m	h_p	h_m-h_p	h_m	h_p	h_m-h_p
M1	53.1	51.0	2.1	51.9	50.7	1.2	50.8	49.7	1.1
M2	55.2	53.3	1.9	54.1	53.0	1.1	52.7	51.8	0.9
M3	56.8	55.1	1.7	55.8	54.8	1.0	54.3	53.4	0.9
M4	75.1	74.6	0.5	74.6	74.5	0.1	73.5	73.6	-0.1
M5	59.6	57.8	1.8	58.5	57.4	1.1	56.7	55.9	0.8
M6	81.8	81.4	0.4	79.3	80.6	-1.3	76.5	77.7	-1.2
M7	86.6	84.9	1.7	82.5	83.8	-1.3	78.8	80.3	-1.5
M8	64.2	63.4	0.8	62.3	62.9	-0.6	60.3	60.8	-0.5
M9	67.0	66.5	0.5	64.5	65.9	-1.4	62.1	63.4	-1.3
M10	94.8	91.6	3.2	88.5	90.1	-1.6	83.9	85.3	-1.4

Table 11. Pressure head and elevation head data for tensiometers read with the Scanivalve.

Z_m = measured elevation head, cm
ψ_m = measured pressure head, cm

	RUN #1		RUN #2	RUN #3
Port	Z_m	ψ_m	ψ_m	ψ_m
2	9.9	34.6	33.9	33.6
3	29.7	8.8	9.4	9.7
4	39.7	0.7	0.4	0.4
5	39.6	3.4	2.4	1.6
6	39.8	12.2	10.1	9.6
7	50.0	-3.0	-2.1	-4.4
8	39.7	11.2	10.0	9.3
9	40.0	12.5	11.6	10.9
10	50.0	3.1	2.2	1.2
11	9.6	44.1	43.0	41.9
12	60.0	-3.5	-5.9	-6.3
13	50.0	7.6	6.2	4.1
14	49.9	11.2	9.5	6.2
15	60.0	2.3	0.6	-2.9
16	79.8	2.0	-0.8	-3.6
17	10.0	51.2	49.4	47.4
18	39.9	22.1	20.3	18.3
19	49.9	12.7	10.8	8.7
20	69.8	15.9	11.8	8.5
21	50.0	13.9	11.9	9.7
22	60.1	5.4	3.2	0.9
23	69.7	18.9	13.9	10.1
24	79.7	10.1	4.7	0.8
25	90.0	1.4	-4.7	-8.7
26	49.8	15.4	13.2	10.8
27	69.9	21.4	15.6	11.5
28	80.0	12.5	6.4	2.2
29	90.1	4.3	-2.8	-7.0
30	29.9	35.4	33.2	31.0
31	49.9	16.6	14.2	11.8
32	60.1	7.1	4.3	2.9
33	70.0	23.7	17.5	13.1
34	90.0	7.1	-0.2	-4.9
35	49.8	17.8	-15.3	12.8
36	60.0	9.1	6.4	3.7
37	79.9	16.7	10.5	5.5
38	89.9	8.6	1.8	-3.2
39	60.0	10.6	8.0	5.2
40	89.9	9.3	3.1	-2.0
41	59.9	10.8	8.0	5.2
42	39.9	29.4	26.8	24.1
43	59.9	11.3	8.4	5.6
44	9.8	58.8	56.3	53.7
45	60.0	12.0	9.3	6.2
46	90.0	10.2	5.4	-0.1
47	60.0	12.2	9.3	6.3

Table 12. Pressure head and elevation head data for tensiometers read with manometers.

z_m = measured elevation head, cm
ψ_m = measured pressure head, cm

	RUN #1		RUN #2	RUN #3
Port	z_m	ψ_m	ψ_m	ψ_m
M1	50.0	3.1	1.9	0.8
M2	59.9	-4.7	-5.8	-7.2
M3	50.0	6.8	5.8	4.3
M4	70.0	5.1	4.6	3.5
M5	60.0	-0.4	-1.5	-3.3
M6	70.1	11.7	9.2	6.4
M7	79.7	6.9	2.8	-0.9
M8	60.1	4.1	2.2	0.2
M9	60.1	6.9	4.4	2.0
M10	79.9	14.9	8.6	4.0